

**MODIS Normalized Water-leaving Radiance
Algorithm Theoretical Basis Document
(MOD 18)**

Version 3

Submitted by

**Howard R. Gordon
Department of Physics
University of Miami
Coral Gables, FL 33124**

Under Contract Number NAS5-31363

August 15, 1996

TABLE OF CONTENTS

Preface	iii
1.0 Introduction	1
1.1 The normalized water-leaving radiance	1
1.2 Outline of the document	2
2.0 Overview and Background Information	3
2.1 Experimental Objectives	3
2.2 Historical Perspective	4
2.3 Instrument Characteristics	5
3.0 Algorithm Description	5
3.1 Theoretical Description	6
3.1.1 Physics of the Algorithm	7
3.1.1.1 The Single Scattering Approximation	10
3.1.1.1.1 The CZCS Algorithm	11
3.1.1.1.2 Application to MODIS	11
3.1.1.2 Multiple-Scattering Effects	19
3.1.1.3 The Multiple-Scattering Algorithm	20
3.1.1.4 Simulated Test of the Multiple-Scattering Algorithm	22
3.1.1.5 Estimation of Aerosol Optical Depth τ_a	28
3.1.1.6 Whitecap Removal Algorithm	31
3.1.1.7 Ancillary Data	35
3.1.1.7.1 Extraterrestrial Solar Irradiance F_0	35
3.1.1.7.2 Ozone Optical Thickness τ_{O_3}	35
3.1.1.7.3 Surface Atmospheric Pressure P_0	36
3.1.1.7.4 Wind Speed W and Wind Vector \vec{W}	37
3.1.1.7.5 Sea Surface Temperature and Atmospheric Stability	37
3.1.1.7.6 Relative Humidity RH	37
3.1.1.8 Examination of Approximations	37
3.1.1.8.1 Aerosol Vertical Structure	37
3.1.1.8.2 Earth-Atmosphere Curvature Effects	40
3.1.1.8.3 Polarization	41
3.1.1.8.4 Sea Surface Roughness	42
3.1.1.8.5 Out-of-band Response	43
3.1.1.9 Remaining Issues	44
3.1.1.9.1 Stratospheric Aerosols and Thin Cirrus Clouds	44
3.1.1.9.2 Appropriateness of the Candidate Aerosol Models	45
3.1.1.9.3 Strongly Absorbing Aerosols	46
3.1.1.9.4 In-Water Radiance Distribution	50
3.1.1.9.5 Diffuse Transmittance	51
3.1.1.9.6 Residual Instrument Polarization Sensitivity	52
3.1.1.9.7 Residual Sun Glitter	53

3.1.2 Mathematical Description of the Algorithm	53
3.1.3 Uncertainty Estimates	55
3.2 Practical Considerations	57
3.2.1 Programming and Procedural Considerations	59
3.2.2 Calibration, Initialization, and Validation	59
3.2.2.1 Calibration Initialization	60
3.2.2.2 Validation	66
3.2.3 Quality Control and Diagnostics	67
3.2.4 Exception Handling	67
3.2.5 Data Dependencies	68
3.2.6 Output Products	68
4.0 Assumptions and Constraints	68
4.1 Assumptions	68
4.2 Constraints	69
5.0 References	70
Appendix A: MODIS Sun Glitter Mask	81
Appendix B: Validation Plan	85

Preface

This algorithm theoretical basis document (ATBD) describes the present state of development of the algorithm for retrieving the normalized water-leaving radiance (reflectance) from MODIS imagery. It replaces Version 0 which was submitted on July 30, 1993, Version 1 submitted February 28, 1994, and Version 2 submitted November 1, 1994. Version 1 was peer reviewed in the spring of 1994 and reviewer suggestions were incorporated into Version 2. Version 3 incorporates the progress of studies relevant to the algorithm since Version 2. The algorithm in its present form is ready for testing with SeaWiFS imagery. Experience gained with SeaWiFS imagery will be useful in assessing the performance of the algorithm. Outstanding issues that require further research are identified in this document.

The author acknowledges the aid of M. Wang in the preparation of Version 0 of this ATBD, K. Ding in the preparation of Version 1, K. Ding and F. He in the preparation of Version 2, and T. Zhang, K. Moore, H. Yang, and Tao Du in the preparation of Version 3.

1.0 Introduction

Following the work of Clarke, Ewing, and Lorenzen [*Clarke, Ewing and Lorenzen, 1970*] showing that the chlorophyll concentration in the surface waters of the ocean could be deduced from aircraft measurements of the spectrum of upwelling light from the sea — the “ocean color” — NASA launched the Coastal Zone Color Scanner (CZCS) on Nimbus-7 in late 1978 [*Gordon et al., 1980; Hovis et al., 1980*]. The CZCS was a proof-of-concept mission with the goal of measuring ocean color from space. It was a scanning radiometer that had four bands in the visible at 443, 520, 550, and 670 nm with bandwidths of 20 nm, one band in the near infrared (NIR) at 750 nm with a bandwidth of 100 nm, and a thermal infrared band (10.5 to 12.5 μm) to measure sea surface temperature. The four visible bands possessed high radiometric sensitivity (well over an order of magnitude higher than other sensors designed for earth resources at that time, e.g., the MSS on the Landsat series) and were specifically designed for ocean color. The CZCS experience demonstrated the feasibility of the measurement of phytoplankton pigments, and possibly even productivity [*Morel and André, 1991; Platt and Sathyendranath, 1988*], on a *global* scale. This feasibility rests squarely on two observations: (1) there exists a more or less universal relationship between the color of the ocean and the phytoplankton pigment concentration for most open ocean waters; and (2) it is possible to develop algorithms to remove the interfering effects of the atmosphere from the imagery. In this document we will describe the basis of the algorithm for removing the atmospheric effects from MODIS imagery over the ocean to derive the normalized water-leaving radiance in the visible. The process of deriving the normalized water-leaving radiance from imagery of the oceans is usually termed *atmospheric correction*.

1.1 The Normalized water-leaving radiance

The normalized water-leaving radiance, $[L_w]_N$, was defined by *Gordon and Clark [1981]* through

$$L_w(\lambda) = [L_w(\lambda)]_N \cos \theta_0 \exp \left[- \left(\frac{\tau_r(\lambda)}{2} + \tau_{O_z}(\lambda) \right) \left(\frac{1}{\cos \theta_0} \right) \right], \quad (1)$$

where $L_w(\lambda)$ is the radiance backscattered *out* of the water at a wavelength λ , $\tau_r(\lambda)$ and $\tau_{O_z}(\lambda)$ are the optical thicknesses of the atmosphere associated with molecular (Rayleigh) scattering and

Ozone absorption, respectively. θ_0 is the solar zenith angle. The normalized water-leaving radiance is approximately the radiance that would exit the ocean in the absence of the atmosphere with the sun at the zenith. (This definition was motivated by the desire to remove, as much as possible, the effects of the atmosphere and the solar zenith angle from $L_w(\lambda)$; however, *Morel and Gentili* [1993] have shown that a residual dependence on θ_0 remains in $[L(\lambda)]_N$.) This quantity is used in other algorithms to derive nearly all of the MODIS ocean products, e.g, the chlorophyll concentration. As such, it plays a central role in the application of MODIS imagery to the oceans.

In the remainder of this document we will abandon the use of radiance in the description of the algorithm in favor of reflectance. The reflectance ρ associated with a radiance L is defined to be $\pi L / F_0 \cos \theta_0$, where F_0 is the extraterrestrial solar irradiance, and θ_0 is the solar zenith angle, i.e., the angle between the line from the pixel under examination to the sun and the local vertical. Reflectance is favored because it may be possible to more accurately calibrate future sensors in reflectance rather than radiance. The desired normalized water-leaving radiance can easily be converted to normalized water-leaving reflectance $[\rho_w]_N$ through

$$[\rho_w]_N = \frac{\pi}{F_0} [L_w]_N, \quad (2)$$

and Eq. (1) becomes

$$\rho_w(\lambda) = [\rho_w(\lambda)]_N \exp \left[- \left(\frac{\tau_r(\lambda)}{2} + \tau_{Oz}(\lambda) \right) \left(\frac{1}{\cos \theta_0} \right) \right] \approx [\rho_w(\lambda)]_N t(\theta_0, \lambda), \quad (3)$$

where $t(\theta_0, \lambda)$ is the CZCS approximation to the diffuse transmittance of the atmosphere (See Section 3.1.1.9.5). Thus, retrieving $[\rho_w]_N$ is equivalent to retrieving $[L_w]_N$. The factor π/F_0 in Eq. (2) is ≈ 0.017 at 443 and 555 nm.

1.2 Outline of the Document

This document is structured in the following manner. First we provide background on the algorithm's role in MODIS products, explain why atmospheric correction is necessary and difficult, and discuss the characteristics of MODIS and SeaWiFS that make atmosphere correction possible. In the main body of the document we develop the proposed algorithm in detail, test it with simulated data, and then discuss the remaining research problems and issues. Next, we present our initial effort toward implementation of the algorithm and provide examples of the influence of sensor radiometric calibration error on the performance of the algorithm. Finally, we describe plans for in-orbit calibration adjustment and validation.

2.0 Overview and Background Information

The purpose of retrieving the normalized water-leaving reflectances $[\rho_w(\lambda)]_N$ is that they are required inputs into algorithms for recovering most of the MODIS ocean products. In this sense they are fundamental to nearly all of the MODIS ocean applications. The accuracy of these products rests squarely on the accuracy of the retrieval of $[\rho_w(\lambda)]_N$.

2.1 Experimental Objectives

The ultimate objective of the application of MODIS imagery over the ocean is to study the primary production, and its spatial and temporal variation, of the oceans on a global scale to better understand the ocean's role in the global carbon cycle. A required component in the estimation of primary productivity is the concentration of chlorophyll *a*. Estimation of the concentration of chlorophyll *a* from MODIS imagery requires the normalized water-leaving radiance. An example of how this is accomplished is provided by the CZCS. Figures 1a and 1b provide $[\rho_w(\lambda)]_N$ at $\lambda = 443$

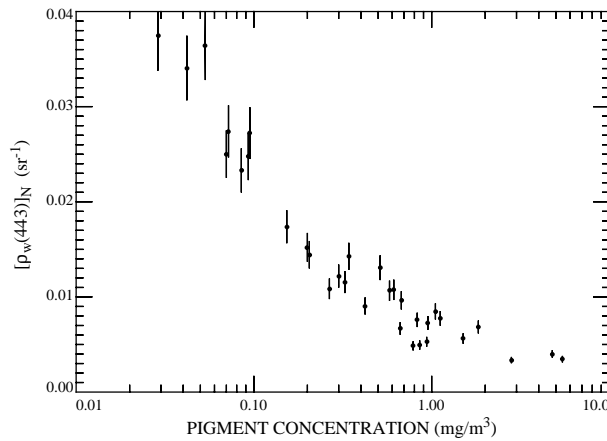


Figure 1a. Normalized water-leaving reflectance at 443 nm as a function of pigment concentration. Redrawn from *Gordon et al.* [1988].

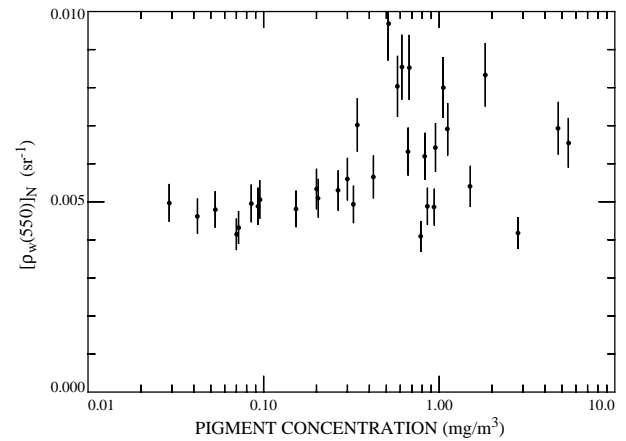


Figure 1b. Normalized water-leaving reflectance at 550 nm as a function of pigment concentration. Redrawn from *Gordon et al.* [1988].

and 550 nm as a function of the pigment concentration (the sum of the concentrations of chlorophyll *a* and its degradation product phaeophytin *a*) in the water. Figure 2 gives the algorithm used to estimate the pigment concentration from $[\rho_w(443)]_N/[\rho_w(550)]_N$. It can be well represented by

$$\log_{10} 3.33C = -1.2 \log_{10} R + 0.5(\log_{10} R)^2 - 2.8(\log_{10} R)^3, \quad (4)$$

with $R = 0.5[\rho_w(443)]_N / [\rho_w(550)]_N$. Thus, the pigment concentration C is directly related to the radiance ratios. Analysis [Gordon, 1990] suggests that the pigment concentration can be derived from the radiance ratio with an error of $\sim \pm 20\%$. Because of relationships such as these that relate bio-optical parameters to $[\rho_w(\lambda)]_N$, the normalized water-leaving reflectance plays a central role in the application of ocean color imagery to the oceans, and atmospheric correction becomes a critical

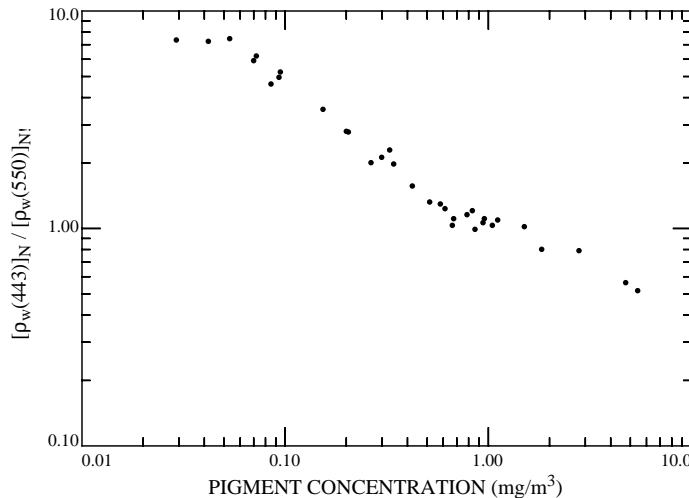


Figure 2. Normalized water-leaving reflectance ratio as a function of pigment concentration. Redrawn from *Gordon et al.* [1988].

factor in determining the fidelity with which bio-optical parameters can be retrieved. When ratios of $[\rho_w]_N$'s are used in computations, as in Eq. (4), small errors of the same sign in the two $[\rho_w]_N$'s will tend to cancel. In most cases the errors in the retrieval of the two $[\rho_w]_N$'s in such ratios *will* have the same sign.

2.2 Historical Perspective

The algorithm for the retrieval of the $[\rho_w]_N$'s from MODIS imagery follows from experience gained with the CZCS. Its purpose is to identify and remove the component of the radiance measured at the sensor that arises from molecular and aerosol scattering in the atmosphere, as well as reflection from the air-sea interface. Since the aerosol concentration and properties are variable in space and time, their effects are unknown *a priori*. The radiometric sensitivity of the CZCS was sufficiently low that it was not necessary to deal with the full complexities of multiple scattering. However, with the increased sensitivity of SeaWiFS and MODIS, multiple scattering in the

atmosphere becomes a central issue in the retrieval algorithms for $[\rho_w]_N$. Examples of important secondary issues not addressed in the CZCS algorithm are the presence of whitecaps on the sea surface and the influence of earth curvature on the algorithm.

The atmospheric correction algorithm for MODIS has not been used previously with satellite imagery; however, the algorithm will be thoroughly tested with SeaWiFS, now scheduled for launch in early 1997.

2.3 Instrument Characteristics

The MODIS and SeaWiFS instruments have similar characteristics (Table 1). The main differences are that MODIS has spectral bands that are half to one-fourth as wide as SeaWiFS, MODIS is 12-bit digitized as opposed to 10-bit for SeaWiFS, and MODIS has approximately twice the SNR. The positions of the spectral bands are similar.

Of critical importance for the retrieval of $[\rho_w]_N$ are spectral bands 7 and 8 (745–785 nm and 845–885 nm, respectively) on SeaWiFS and bands 15 and 16 (745–755 nm and 857–872 nm, respectively) on MODIS. Because of the strong absorption by liquid water, virtually no light will exit the ocean in these bands, except in the most turbid coastal waters, so radiance measured by the sensor originates from the scattering of solar irradiance by the atmosphere and the sea surface. These bands can therefore be used to assess the atmospheric effects. Band 6 on SeaWiFS (660–680 nm) and band 13 on MODIS (662–672 nm) can also be utilized in waters with pigment concentration $\lesssim 0.5 - 1.0 \text{ mg/m}^3$, but probably not in coastal waters. Band 7 on SeaWiFS overlaps the O_2 “A” absorption band centered at $\sim 762 \text{ nm}$. The influence of this absorption band on SeaWiFS atmospheric correction has been studied by *Ding and Gordon [1995]*; however, as MODIS band 15 does not overlap the O_2 absorption, we shall not discuss this problem further in this document.

The application of these bands to atmospheric correction is straightforward in principle: one assesses the contribution of the atmosphere in the NIR and extrapolates it into the visible.

3.0 Algorithm Description

This section provides a description of the entire algorithm. Before beginning, a few preliminaries are useful. Table 1 provides the MODIS radiometric specifications in terms of reflectance for a solar zenith angle of 60° and viewing near the scan edge. For convenience we also provide

the “noise equivalent reflectance” ($\text{NE}\Delta\rho$) for the SeaWiFS and CZCS bands closest to the given

Table 1: Comparison of the radiometric performance of MODIS, SeaWiFS, and CZCS for $\theta_0 = 60^\circ$ near the scan edge.

Band	λ (nm)	ρ_{max} (sr^{-1})	ρ_t (sr^{-1})	$[\rho_w]_N$ (sr^{-1})	$\text{NE}\Delta\rho$ (sr^{-1})		
					MODIS	SeaWiFS	CZCS
8	412	0.50	0.34	0.040	0.00018	0.00068	–
9	443	0.46	0.29	0.038	0.00016	0.00043	0.0011
10	490	0.36	0.23	0.024	0.00014	0.00034	–
11	530	0.30	0.19	0.0090	0.00013	0.00031	0.00058
12	550	0.25	0.154	0.0040	0.00010	0.00027	0.00064
13	670	0.17	0.105	0.0004	0.00004	0.00023	0.00051
14	681	0.17	0.105	0.0003	0.00004	–	–
15	750	0.15	0.081	–	0.000085	0.00018	–
16	865	0.13	0.069	–	0.000076	0.00015	–

MODIS band. Note that MODIS is typically 2-3 times more sensitive than SeaWiFS, which in turn is approximately twice as sensitive as CZCS. Exceptions are the MODIS bands 13 and 14 which are to be used to measure the chlorophyll *a* fluorescence near 683 nm [Neville and Gower, 1977]. These bands are ~ 6 times more sensitive than SeaWiFS and ~ 12 times more sensitive than CZCS. The table also provides the typical top-of-the-atmosphere reflectance ρ_t and the normalized water-leaving reflectance $[\rho_w]_N$ for a very low pigment concentration (Sargasso Sea in summer) [Gordon and Clark, 1981]. Note that $[\rho_w]_N$ is only a small fraction of ρ_t . To recover $[\rho_w]_N$ in the blue (443 nm) for these waters with an error $< 5\%$ requires an atmospheric correction of $\sim \pm 0.001$ to ± 0.002 in reflectance, i.e., about five to ten times the $\text{NE}\Delta\rho$. This is our goal for MODIS band 9. It is shown later that when this goal is met, the error in $[\rho_w]_N$ at 550 nm will be ~ 3 –4 times smaller than that at 443 nm. In this case, Figure 1 shows that the error in the ratio R in Eq. (4) usually will be dominated by error in $[\rho_w]_N$ at 443 nm, the exception being very low values of C .

3.1 Theoretical Description

In this section we provide the theoretical basis of the algorithm. We begin by discussing the basic physics of the algorithm, starting with single scattering and progressing into the multiple scattering regime. Then a whitecap removal algorithm, which is in the process of validation, is

presented. Next, the required ancillary data are itemized, the approximations used in the development of the algorithm are examined, and the remaining research issues are discussed. Finally, an implementation of the algorithm is described and the effects of MODIS radiometric calibration uncertainty is considered.

3.1.1 Physics of the Algorithm

The radiance received by a sensor at the top of the atmosphere (TOA) in a spectral band centered at a wavelength λ_i , $L_t(\lambda_i)$, can be divided into the following components: $L_{path}(\lambda_i)$ the radiance generated along the optical path by scattering in the atmosphere *and* by specular reflection of atmospherically scattered light (skylight) from the sea surface; $L_g(\lambda_i)$ the contribution arising from specular reflection of direct sunlight from the sea surface (sun glitter); $L_{wc}(\lambda_i)$ the contribution arising from sunlight and skylight reflecting from individual whitecaps on the sea surface; and, $L_w(\lambda_i)$ the desired water-leaving radiance; i.e.,

$$L_t(\lambda_i) = L_{path}(\lambda_i) + T(\lambda_i)L_g(\lambda_i) + t(\lambda_i)L_{wc}(\lambda_i) + t(\lambda_i)L_w(\lambda_i). \quad (5)$$

L_{wc} and L_w are area-weighted averages of the radiance leaving whitecap-covered and whitecap-free areas of the surface, respectively. In this equation, T and t are the direct and diffuse, transmittance of the atmosphere, respectively. The diffuse transmittance is appropriate for the water-leaving radiance and the whitecap radiance as they have near-uniform angular distribution. It is discussed in detail in Section 3.1.1.9.5. In contrast, to the diffuse transmittance, the direct transmittance is appropriate when the angular distribution of the radiance is approximately a Dirac delta function. As the sun glitter is highly directional (except at high wind speeds), its transmittance is approximated by the direct transmittance. The direct transmittance is given by

$$T(\theta_v, \lambda) = \exp \left[- (\tau_r(\lambda) + \tau_{Oz}(\lambda) + \tau_a(\lambda)) \left(\frac{1}{\mu_v} \right) \right],$$

where $\mu_v = \cos \theta_v$, θ_v is the angle the exiting radiance makes with the upward normal at the TOA, and τ_r , τ_a , and τ_{Oz} are, respectively, the Rayleigh, aerosol, and Ozone optical thicknesses. In this equation, we have ignored the possibility of weak continuum (in the atmospheric windows) absorption by water vapor [Eldridge, 1967; Tomasi, 1979a; Tomasi, 1979b] due to the extreme difficulty in separating the direct effect of water vapor absorption from the indirect effect that

water vapor will have on the extinction of hygroscopic aerosols [Fraser, 1975]. Converting to reflectance, Eq. (5) becomes

$$\rho_t(\lambda_i) = \rho_{path}(\lambda_i) + T(\lambda_i)\rho_g(\lambda_i) + t(\lambda_i)\rho_{wc}(\lambda_i) + t(\lambda_i)\rho_w(\lambda_i). \quad (6)$$

Thus, from the measured $\rho_t(\lambda_i)$ we require an algorithm that provides accurate estimates of $\rho_{path}(\lambda_i)$, $T(\lambda_i)\rho_g(\lambda_i)$, $t(\lambda_i)\rho_{wc}(\lambda_i)$, and $t(\lambda_i)$. Near the sun's glitter pattern $T(\lambda_i)\rho_g(\lambda_i)$ is so large that the imagery is virtually useless and must be discarded. A sun glitter mask to remove seriously contaminated pixels is described in Appendix A. Away from the glitter pattern, i.e., where values of $T(\lambda_i)\rho_g(\lambda_i)$ become negligibly small, the largest of the remaining terms, and most difficult to estimate, is $\rho_{path}(\lambda_i)$. This difficulty is principally due to the aerosol by virtue of its highly variable concentration and optical properties. Thus, we concentrate on this term first, then consider $t(\lambda_i)\rho_{wc}(\lambda_i)$ and the ancillary data required to operate the algorithm.

In general, ρ_{path} can be decomposed into several components:

$$\rho_{path} = \rho_r(\lambda) + \rho_a(\lambda) + \rho_{ra}(\lambda) \quad (7)$$

where ρ_r is the reflectance resulting from multiple scattering by air molecules (Rayleigh scattering) in the absence of aerosols, ρ_a is the reflectance resulting from multiple scattering by aerosols in the absence of the air, and ρ_{ra} is the interaction term between molecular and aerosol scattering [Deschamps, Herman and Tanre, 1983]. The term ρ_{ra} accounts for the interaction between Rayleigh and aerosol scattering, e.g., photons first scattered by the air then scattered by aerosols, or photons first scattered by aerosols then air, etc. This term is zero in the single scattering case, in which photons are only scattered once, and it can be ignored as long as the amount of multiple scattering is small, i.e., at small Rayleigh and aerosol optical thicknesses. We note that given the surface atmospheric pressure (to determine the value of τ_r) and the surface wind speed (to define the roughness of the sea surface), ρ_r can be computed accurately, even accounting for polarization effects [Gordon, Brown and Evans, 1988; Gordon and Wang, 1992b].

In modeling the propagation of radiance in the ocean-atmosphere system, we assume that the atmosphere can be considered to be a vertically stratified, plane parallel medium. The medium is described by providing the extinction coefficient, $c(h)$, as a function of altitude h , the scattering

phase function for scattering of radiance from direction $\hat{\xi}'$ to direction $\hat{\xi}$, $P(h; \hat{\xi}' \rightarrow \hat{\xi})$, and the single scattering albedo $\omega_0(h)$. Replacing h by the optical depth τ defined as

$$\tau(h) = \int_h^\infty c(h) dh,$$

the propagation of radiance in such a medium in the scalar approximation (the polarization state of the radiance, and the change in polarization induced by the scattering process is ignored) is governed by the radiative transfer equation (RTE):

$$\hat{\xi} \cdot \hat{n} \frac{dL(\tau, \hat{\xi})}{d\tau} = -L(\tau, \hat{\xi}) + \frac{\omega_0(\tau)}{4\pi} \int_{\text{all } \hat{\xi}'} P(\tau; \hat{\xi}' \rightarrow \hat{\xi}) L(\tau, \hat{\xi}') d\Omega(\hat{\xi}'),$$

where $d\Omega(\hat{\xi}')$ is the differential of solid angle around the direction $\hat{\xi}'$, and \hat{n} is a unit vector in the nadir direction (normal to the sea surface pointed down). Analytical solutions to the RTE are possible only in the simplest case, e.g., $\omega_0 = 0$, so normally one must be satisfied with numerical solutions.

In principal this equation must be solved for the coupled ocean-atmosphere system; however, because of the very low albedo of the ocean (Table 1) it is not necessary to consider the coupling [Gordon, 1976], i.e., we can ignore processes such as photons being backscattered out of the water and then scattered back into the water and backscattered out again, etc. The water-leaving radiance simply propagates to the sensor (ρ_{path} is independent of ρ_w in Eq. (6)) and the ocean and atmosphere decouple, hence, we need only understand the solution of the atmospheric part of the problem, i.e., an atmosphere bounded by a Fresnel-reflecting ocean surface.

As the goal of atmospheric correction is to retrieve $\rho_w(443)$ with an uncertainty less than ± 0.002 , i.e., $\sim \pm 0.6\%$ of $\rho_t(443)$ (Table 1), for the development and testing of the algorithm we require solutions of the RTE that yield ρ_t with an uncertainty $\ll 0.6\%$. For the bulk of the work described here, ρ_t was generated using the successive-order-of-scattering method [van de Hulst, 1980]. To understand the accuracy of this code, a second code was developed employing Monte Carlo methods. Typically, the values of ρ_t produced by the two codes differ by less than 0.05%. Thus, either code meets the accuracy required for this work.

We will assume, as justified earlier, that $\rho_w = 0$ in the NIR. The problem we are required to solve can then be stated in a simple manner: given the satellite measurement of the radiance (reflectance) of the ocean-atmosphere system in the NIR, predict the radiance (reflectance) that

would be observed in the visible. The difference between the predicted and the measured radiance (reflectance) of the ocean-atmosphere system is the water-leaving radiance (reflectance) transmitted to the top of the atmosphere.

3.1.1.1 The Single Scattering Approximation

It is useful to consider $\rho_{path}(\lambda_i)$ in the limit that the optical thickness of the atmosphere is $\ll 1$. We refer to this as the single-scattering limit. Formulas for the reflectances in this limit are referred to as the single-scattering approximation. The CZCS algorithm was based on the single-scattering approximation. In this approximation the path reflectance reduces to

$$\rho_{path}(\lambda_i) = \rho_r(\lambda_i) + \rho_{as}(\lambda_i), \quad (8)$$

with the aerosol contribution ρ_{as} provided by

$$\begin{aligned} \rho_{as}(\lambda) &= \omega_a(\lambda) \tau_a(\lambda) p_a(\theta_v, \phi_v; \theta_0, \phi_0; \lambda) / 4 \cos \theta_v \cos \theta_0, \\ p_a(\theta_v, \phi_v; \theta_0, \phi_0; \lambda) &= P_a(\theta_-, \lambda) + \left(r(\theta_v) + r(\theta_0) \right) P_a(\theta_+, \lambda), \\ \cos \theta_{\pm} &= \pm \cos \theta_0 \cos \theta_v - \sin \theta_0 \sin \theta_v \cos(\phi_v - \phi_0), \end{aligned} \quad (9)$$

where $P_a(\alpha, \lambda)$ is the aerosol scattering phase function for a scattering angle α , ω_a is the aerosol single scattering albedo, and $r(\alpha)$ is the Fresnel reflectance of the interface for an incident angle α . The angles θ_0 and ϕ_0 are, respectively, the zenith and azimuth angles of a vector from the point on the sea surface under examination (pixel) to the sun, and likewise, θ_v and ϕ_v are the zenith and azimuth angles of a vector from the pixel to the sensor. These are measured with respect to the *upward* normal so θ_v and θ_0 are both less than 90° in these equations. In what follows usually we take $\phi_0 = 0$.

Following the approach described above, we assume we are given the the path reflectance at two bands in the NIR at λ_s and λ_l , where the subscript “s” stands for short and “l” for long, e.g., for MODIS $\lambda_s = 750$ nm and $\lambda_l = 865$ nm. [Note that since we are ignoring sun glitter $T(\lambda_i)\rho_g(\lambda_i)$, this implies that $t(\lambda_i)\rho_{wc}(\lambda_i)$ has also been provided.] Given estimates of the surface atmospheric pressure and the wind speed (ancillary data), $\rho_r(\lambda)$ can be computed precisely and therefore $\rho_{as}(\lambda_s)$ and $\rho_{as}(\lambda_l)$ can be determined from the associated measurements of ρ_{path} at λ_s and λ_l . This allows estimation of the parameter $\varepsilon(\lambda_s, \lambda_l)$:

$$\varepsilon(\lambda_s, \lambda_l) \equiv \frac{\rho_{as}(\lambda_s)}{\rho_{as}(\lambda_l)} = \frac{\omega_a(\lambda_s) \tau_a(\lambda_s) p_a(\theta_v, \phi_v; \theta_0, \phi_0; \lambda_s)}{\omega_a(\lambda_l) \tau_a(\lambda_l) p_a(\theta_v, \phi_v; \theta_0, \phi_0; \lambda_l)}. \quad (10)$$

If we can compute the value of $\varepsilon(\lambda_i, \lambda_l)$ for the MODIS band at λ_i from the value of $\varepsilon(\lambda_s, \lambda_l)$, this will yield $\rho_{as}(\lambda_i)$, which, when combined with $\rho_r(\lambda_i)$, provides the desired $\rho_{path}(\lambda_i)$. Clearly, the key to this procedure is the estimation of $\varepsilon(\lambda_i, \lambda_l)$ from $\varepsilon(\lambda_s, \lambda_l)$.

3.1.1.1.1 The CZCS Algorithm

The atmospheric correction algorithm for CZCS was described in detail in *Evans and Gordon* [1994]. Briefly, the basic CZCS algorithm [*Gordon, 1978; Gordon and Clark, 1980*] was based on single scattering; however, $\rho_r(\lambda_i)$ was computed accurately, including the effects of multiple scattering and polarization [*Gordon, Brown and Evans, 1988*]. As there were no NIR bands, the algorithm could not be operated as described in Section 3.1.1.1. However, Table 1 shows that $\rho_w(670)$ can generally be taken to be zero (at least if the pigment concentration is low enough). Thus, the single scattering algorithm was typically operated with $\lambda_l = 670$ nm and $\rho_w(\lambda_l) = 0$. Unfortunately, there was no shorter wavelength (λ_s) for which $\rho_w = 0$, so in the processing of the CZCS global data set [*Feldman et al., 1989*] $\varepsilon(\lambda_i, \lambda_s)$ was set equal to unity. This is characteristic of a maritime aerosol at high relative humidity.

For sufficiently low C values, Figure 1b suggests that $[\rho_w(550)]_N$ is approximately constant. This fact can be used to estimate $\varepsilon(550, 670)$ for such “clear water” regions [*Gordon and Clark, 1981*] in a scene, allowing a basis for extrapolation to 520 and 443 nm. If the resulting $\varepsilon(\lambda_i, \lambda_l)$ is then assumed to be valid for the entire image, retrieval of $[\rho_w(\lambda_i)]_N$ and C can be effected for the image. This is the procedure used by *Gordon et al.* [1983] in the Middle Atlantic Bight. Unfortunately, there are serious difficulties applying this procedure routinely. For example, the image of interest may contain no “clear water,” the ε ’s may vary over the image because of variations in aerosol type, and the pigment concentration may not be small enough to take $\rho_w = 0$ at 670 nm. Morel and his co-workers have developed a promising approach for dealing these problems in Case 1 waters [*André and Morel, 1991; Bricaud and Morel, 1987*] based on the ideas of *Smith and Wilson* [1981]. This involves utilizing a modeled relationship between C and $[\rho_w(\lambda_i)]_N$. Fortunately, for the sensors of concern in this paper (SeaWiFS and MODIS), these problems are circumvented by virtue of the additional spectral bands with $\lambda > 700$ nm.

3.1.1.1.2 Application to MODIS

As the key to application of the single scattering algorithm to the EOS era sensors is the extrapolation from $\varepsilon(\lambda_s, \lambda_l)$ to $\varepsilon(\lambda_i, \lambda_l)$, which involves more than a factor of two in wavelength, it is important to try to gain some insight into the possible spectral behavior of $\varepsilon(\lambda_i, \lambda_l)$. This has been attempted by *Gordon and Wang* [1994b] by computing $\varepsilon(\lambda_i, \lambda_l)$ for several aerosol models. Briefly, they used aerosol models that were developed by *Shettle and Fenn* [1979] for LOWTRAN-6 [*Kenizys et al.*, 1983]. These models consist of particles distributed in size according to combinations of log-normal distributions. The size frequency distribution $n(D)$ is given by

$$n(D) = \sum_{i=1}^2 n_i(D),$$

with

$$n_i(D) = \frac{dN_i(D)}{dD} = \frac{N_i}{\log_e(10)\sqrt{2\pi}\sigma_i D} \exp \left[-\frac{1}{2} \left(\frac{\log_{10}(D/D_i)}{\sigma_i} \right)^2 \right],$$

where, $dN_i(D)$ is the number of particles per unit volume between D and $D + dD$, D_i and σ_i are the median diameter and the standard deviation, respectively, and N_i is the total number density of the i^{th} component. Since hygroscopic particles swell with increasing relative humidity (RH), D_i and σ_i are functions of RH. The smaller size fraction is a mixture of 70% water soluble and 30% dust-like particles called the Tropospheric aerosol. It has been used to represent the aerosols within the free troposphere above the boundary-layer [*Shettle and Fenn*, 1979]. The refractive index m for this component at 550 nm ranges from $1.53 - 0.0066i$ at $\text{RH} = 0$, to $1.369 - 0.0012i$ at $\text{RH} = 98\%$. Thus as the particles absorb more water, the real part of their refractive index approaches that of water and the imaginary part (proportional to the absorption coefficient) decreases. Because of the moderate imaginary part of the refractive index, these particles have weak absorption and ω_a ranges from 0.959 to 0.989 for $0 \leq \text{RH} \leq 98\%$. The modal diameter of this component is always $< 0.1 \mu\text{m}$. The larger fraction is a sea salt-based component, the “Oceanic” aerosol. Its modal diameter varies from about 0.3 to $1.2 \mu\text{m}$ as RH varies from 0 to 98%. Its index of refraction is essentially real (imaginary part $\sim 10^{-8}$), so $\omega_a = 1$. Like the tropospheric aerosol its real part ranges from 1.5 at $\text{RH} = 0$ to 1.35 at $\text{RH} = 98\%$.

From these components, three basic models were constructed: the Tropospheric model with no Oceanic contribution; the Maritime model for which 99% of the particles have the Tropospheric characteristics and 1% the Oceanic; and the Coastal model for which 99.5% of the particles have

the Tropospheric characteristics and 0.5% the Oceanic. *Gordon and Wang* [1994b] introduced

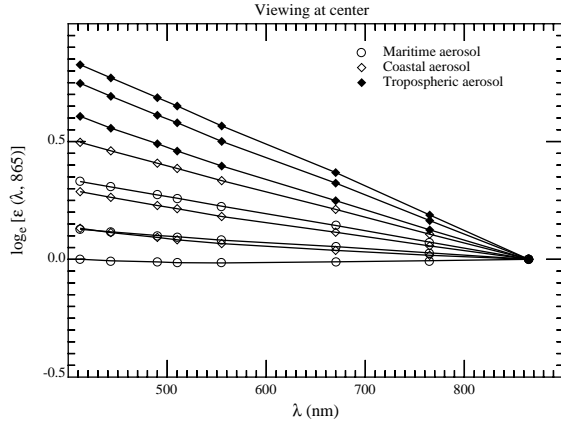


Figure 3a. $\varepsilon(\lambda, 865)$ for nadir viewing with $\theta_0 = 60^\circ$ for the Maritime, Coastal, and Tropospheric aerosol models. For each model, the RH values are 50, 80, and 98% from the upper to the lower curves.

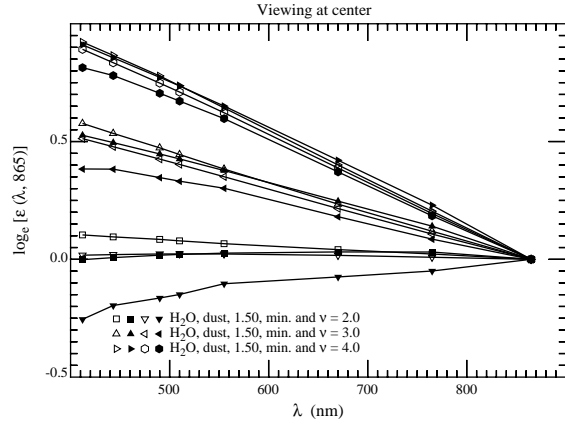


Figure 3b. $\varepsilon(\lambda, 865)$ for nadir viewing with $\theta_0 = 60^\circ$ for the Haze C models. Note that the open symbols are for models with little or no absorption, while the filled symbols are for absorbing models.

the Coastal aerosol model to represent the aerosol over the oceans nearer the coast (less Oceanic contribution). The properties of all three aerosol models depend on the wavelength and relative humidity. With the values of D_i , σ_i , and $m_i(\lambda)$ taken from *Shettle and Fenn* [1979], Mie theory was used to calculate the optical properties for all three models for the SeaWiFS and MODIS spectral bands at different relative humidities.

Sample results for $\varepsilon(\lambda_i, \lambda_l)$, where λ_l is taken to be 865 nm (SeaWiFS), are presented in Figure 3a. These computations suggest that there should be a strong variation of ε with aerosol model and RH. The increase in particle size (due to swelling) with increasing RH clearly reduces the spectral variation of ε . The spectral variation of ε is due in large part to the spectral variation of the aerosol optical thickness, τ_a ; however, additional variation is produced by the aerosol phase function. Note that Figure 3a is plotted in a format that would yield a straight line under the hypothesis that $\varepsilon(\lambda_i, \lambda_l) = \exp[c(\lambda_l - \lambda_i)]$, where c is a constant. This shows that over the range 412–865 nm $\varepsilon(\lambda_i, \lambda_l)$ can be considered to be an exponential function of $\lambda_l - \lambda_i$, for the *Shettle and Fenn* [1979] models. *Wang and Gordon* [1994] have used this fact to extend the CZCS algorithm for use with SeaWiFS and MODIS.

We now examine the accuracy of this CZCS-type single-scattering algorithm based on an assumed exponential spectral variation of $\varepsilon(\lambda_i, \lambda_l)$. For this purpose, we simulated atmospheres using

an array of aerosol models. First, the aerosol optical properties were taken from the Tropospheric, Coastal, and Maritime models at RH = 80%, denoted, respectively, as T80, C80, and M80. Then, we simulated the aerosol using the *Shettle and Fenn* [1979] Urban model at RH = 80% (U80). This model shows strong absorption. In addition to the water soluble and dust-like particles of the Tropospheric model, the Urban model contains soot-like particles (combustion products). Also, the Urban model has a second, larger particle, mode in addition to that of the Tropospheric model. At 865 nm the Mie theory computations yielded, $\omega_a = 0.9934, 0.9884, \text{ and } 0.9528$, respectively, for the Maritime, Coastal, and Tropospheric models (RH = 80%), while in contrast, $\omega_a = 0.7481$ for the Urban model. Here, the Urban model is intended to represent aerosols that might be present over the oceans near areas with considerable urban pollution, e.g., the Middle Atlantic Bight off the U.S. East Coast in summer. Finally, we examined aerosols with a different analytical form for the size distribution [*Junge*, 1958]:

$$\begin{aligned} n(D) = \frac{dN(D)}{dD} &= K, & D_0 < D < D_1, \\ &= K \left(\frac{D_1}{D} \right)^{\nu+1}, & D_1 < D < D_2, \\ &= 0, & D > D_2, \end{aligned}$$

with $D_0 = 0.06 \mu\text{m}$, $D_1 = 0.20 \mu\text{m}$, and $D_2 = 20 \mu\text{m}$. Following *Deirmendjian* [1969] we call these Haze C models. Twelve separate Haze C models were considered: $\nu = 2, 3, \text{ and } 4$, with the refractive index of the particles taken to be that of liquid water (from *Hale and Querry* [1973]), close to that of the dust component in the Tropospheric model ($1.53 - 0.008i$), nonabsorbing crystals ($1.50 - 0i$), and absorbing minerals that might be expected from desert aerosols transported over the oceans [*d'Almeida, Koepke and Shettle*, 1991]. The spectral behavior of $\varepsilon(\lambda, 865)$ for these models is presented in Figure 3b. We see that the absorption-free (open symbols) Haze C models display a behavior similar to the Shettle and Fenn models; however, for models with strong absorption (solid symbols) departures are seen, especially for the mineral models for which the imaginary part of the refractive index increases with decreasing λ . An important observation from Figure 3b is that, in general, $\varepsilon(765, 865)$ cannot be utilized to discriminate between weakly- and strongly-absorbing aerosols with similar size distributions.

Using these aerosol models we generated hypothetical atmospheres with a two-layer structure: the aerosols occupying the lower layer, and all molecular scattering confined to the upper layer. This distribution of aerosols is similar to that typically found over the oceans when the aerosol is locally generated, i.e., most of the aerosol is confined to the marine boundary layer [*Sasano and*

Browell, 1989]. The atmosphere was bounded by a flat (smooth) Fresnel-reflecting sea surface, and all photons that penetrated the interface were assumed to be absorbed in the ocean. The RTE in the scalar approximation was solved for this hypothetical atmosphere using the successive-order-of-

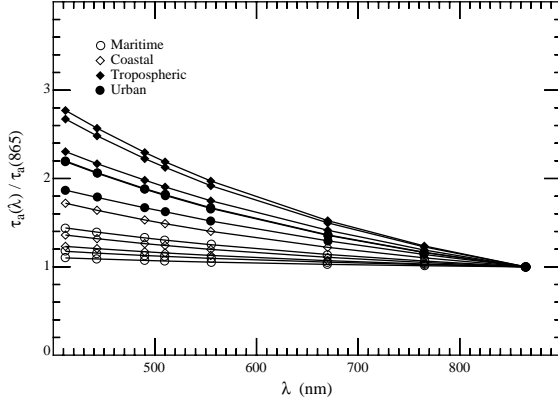


Figure 4a. Spectral variation of τ_a for the Maritime, Coastal, and Tropospheric aerosol models. For each model, the RH values are 50, 80, and 98% from the upper to the lower curves.

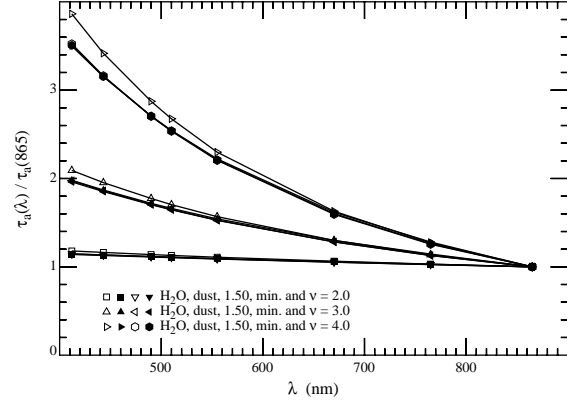


Figure 4b. Spectral variation of τ_a for the Haze C models. Note that the open symbols are for models with little or no absorption, while the filled symbols are for absorbing models.

scattering method [*van de Hulst*, 1980] to provide pseudo TOA reflectance (ρ_t) data. All significant orders of multiple scattering were included. As the surface was assumed to be smooth (no wind), the sun glitter and whitecap terms in Eq. (6) are absent. The simulations of ρ_t were carried out for the following geometries: $\theta_0 = 20^\circ, 40^\circ$, and 60° , with $\theta_v \approx 1^\circ$ and $\phi_v - \phi_0 = 90^\circ$, i.e., viewing near the MODIS scan center; and $\theta_0 = 0^\circ, 20^\circ, 40^\circ$, and 60° , with $\theta_v \approx 45^\circ$ and $\phi_v - \phi_0 = 90^\circ$, i.e., viewing near the scan edge. In this manner a wide range of sun-viewing geometries were included. Four wavelengths were considered: $\lambda_i = 443, 555, 765$, and 865 nm. The values used for the aerosol optical thickness at 865 nm, $\tau_a(865)$, were 0.1, 0.2, 0.3, and 0.4. The values of $\tau_a(\lambda_i)$ at the other wavelengths were determined from the spectral variation of the extinction coefficient for each particular model. These are provided in Figure 4. The Haze C models clearly show that the spectral variation of τ_a is principally determined by the size distribution, with the index of refraction playing only a minor role. Equation (10) suggests that there should be a relationship between $\tau_a(\lambda)/\tau_a(865)$ and $\varepsilon(\lambda, 865)$. Figure 5 provides an example of this for $\theta_0 = 60^\circ$ and nadir viewing, i.e., the same geometry as in Figure 3, with $\varepsilon(765, 865)$ used rather than $\varepsilon(443, 865)$. Thus, for a given $\tau_a(865)$, $\tau_a(443)$ will generally increase with increasing $\varepsilon(765, 865)$. This will be useful in interpreting the results described below.

As the true $\rho_w(\lambda_i)$ was taken to be zero in the pseudo data (all photons entering the water were absorbed), the error in atmospheric correction, i.e., the error in the retrieved water-leaving

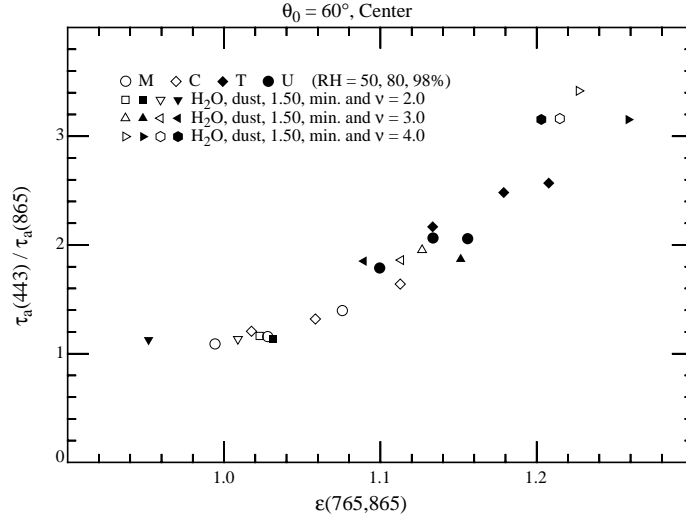


Figure 5. Relationship between $\epsilon(765, 865)$ and $\tau_a(443)/\tau_a(865)$ for the various aerosol models with $\theta_0 = 60^\circ$ and nadir viewing.

reflectance, $\Delta(t\rho_w)$, is just the error in the predicted path radiance. This is

$$\Delta(t\rho_w(\lambda_i)) = \rho_t(\lambda_i) - \rho_{path}(\lambda_i) = \rho_t(\lambda_i) - \rho_r(\lambda_i) - \epsilon^{(e)}(\lambda_i, \lambda_l)\rho_{as}(\lambda_l), \quad (11)$$

where $\epsilon^{(e)}(\lambda_i, \lambda_l)$ is the estimated value of $\epsilon(\lambda_i, \lambda_l)$ assuming an exponential variation with λ_i :

$$\epsilon^{(e)}(\lambda_i, \lambda_l) \equiv \exp[c(\lambda_l - \lambda_i)] = \exp \left[\left(\frac{\lambda_l - \lambda_i}{\lambda_l - \lambda_s} \right) \log_e \left(\frac{\rho_{as}(\lambda_s)}{\rho_{as}(\lambda_l)} \right) \right].$$

$\rho_r(\lambda_i)$ was computed using the same radiative transfer code, i.e., it includes all effects of multiple scattering, but not polarization. In an actual application, $\rho_r(\lambda_i)$ would be computed using a code that included polarization as well [Gordon, Brown and Evans, 1988]. Figure 6 provides the error in the retrieved normalized water-leaving reflectance, $\Delta[\rho_w(443)]_N$, for the seven sun-viewing geometries and for $\tau_a(865) = 0.1$ and 0.2. To derive $\Delta[\rho_w]_N$ from $\Delta t\rho_w$, the approximation for t similar to that used in processing CZCS imagery was utilized (See Section 3.1.1.9.5). The x -axis in Figure 6, $\epsilon^{(e)}(765, 865)$, is the *estimated* value for the indicated model and geometry.

In the absence of aerosol absorption (open symbols), the performance of this simple algorithm is truly remarkable, as Figures 4b and 5 show that for $\nu = 4$, $\tau_a(443) \approx 0.35$ and 0.70 for Figures

6a and 6b, respectively. The large negative errors for $\nu = 4$ occur at the scan edge with $\theta_0 = 60^\circ$, i.e., the geometry with the most multiple scattering. For $\nu = 3$ ($\tau_a(443) \sim 0.2$ and 0.4 (Figures 4b and 5 for Figures 6a and 6b, respectively), the retrieved value of $[\rho_w(443)]_N$ is usually within the acceptable limits.

In the case of absorbing aerosols, the errors are seen to be mostly negative, and to grow rapidly with $\tau_a(443)$. Negative errors are particularly troublesome as they can lead to negative values in

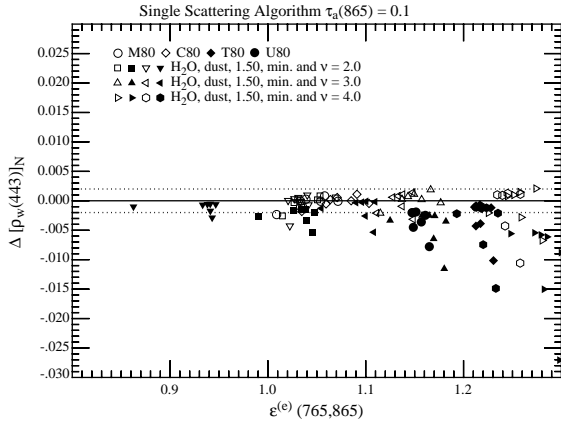


Figure 6a. $\Delta[\rho_w(443)]_N$ as a function of $\epsilon^{(e)}(765,865)$ for $\tau_a(865) = 0.1$ and all of the aerosol models and viewing geometries examined in the study.

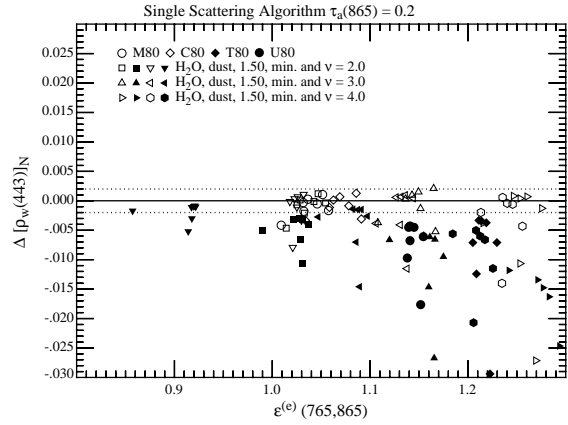


Figure 6b. $\Delta[\rho_w(443)]_N$ as a function of $\epsilon^{(e)}(765,865)$ for $\tau_a(865) = 0.2$ and all of the aerosol models and viewing geometries examined in the study.

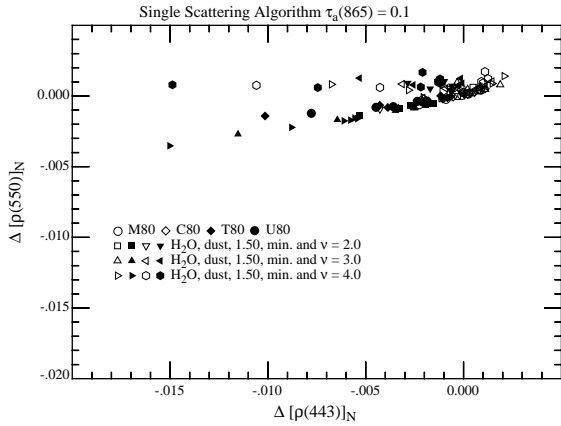


Figure 6c. $\Delta[\rho_w(550)]_N$ as a function of $\Delta[\rho_w(443)]_N$ for the results in Figure 6a.

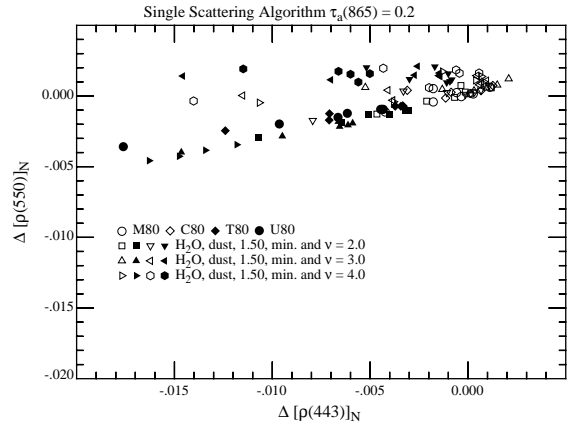


Figure 6d. $\Delta[\rho_w(550)]_N$ as a function of $\Delta[\rho_w(443)]_N$ for the results in Figure 6b.

the retrieved $[\rho_w(443)]_N$ when the pigment concentration $\gtrsim 0.5 - 1.0 \text{ mg/m}^3$. The source of the error for absorbing aerosols is twofold. For the Haze C aerosol, it can be seen from Figure 3b that,

in contrast to the nonabsorbing aerosols, an exponential extrapolation of $\varepsilon(765, 865)$ to $\varepsilon(443, 865)$ would lead to an erroneous overestimation of $\varepsilon(443, 865)$, the single exception being the mineral aerosol with $\nu = 2$. This will cause an overestimation of the aerosol contribution at 443 nm, which in turn will result in a negative error in $[\rho_w(443)]_N$. In contrast, the extrapolation does work well for T80 (Figure 3a) and, as we shall see later, in this case the error is principally due to multiple scattering, which is strongly influenced by even weak aerosol absorption.

The error in $[\rho_w(550)]_N$ as related to the associated error in $[\rho_w(443)]_N$ is provided in Figures 6c and 6d. The observed improvement in atmospheric correction at 550 compared to 443 nm can be traced to the facts that (1) the ε determination requires a smaller extrapolation at 550 nm, and (2) there is less multiple scattering at 550 nm as both τ_a (Figure 4) and τ_r are smaller. Notably, the error at 550 nm is usually much less than that at 443 nm, there being a tendency for $\Delta[\rho_w(550)]_N \sim (1/4)\Delta[\rho_w(443)]_N$, although occasionally $|\Delta[\rho_w(550)]_N| \gtrsim |\Delta[\rho_w(443)]_N|$. Thus, in a pigment ratio algorithm such as Eq. (4), the error at 443 nm will usually be the more significant error in R .

It is useful at this point to review the sparse direct observations of the aerosol optical thickness over the oceans. In the open ocean, far from sources of pollution and/or sources of desert aerosols, the atmosphere is very clear. In the Pacific $\tau_a(550)$ is found in the range 0.04 to 0.24 with a mean of 0.13 and Angstrom exponent of 0.56 [Villevalde *et al.*, 1994], suggesting a mean $\tau_a(865)$ of ~ 0.1 and a maximum of ~ 0.19 . Similar results are obtained for the North Atlantic [Korotaev *et al.*, 1993; Reddy *et al.*, 1990]. In such a region, Lechner *et al.* [1989] found that there were low concentrations of aerosol in the free troposphere possessing a Haze C-like distribution with an average ν of ~ 3.5 , while in the marine boundary layer the concentration was much higher (and highly variable) with an average ν of ~ 1.8 , and sometimes even a bimodal size distribution (the large mode presumably resulting from local generation of aerosols by breaking waves). In contrast, in the region of the Atlantic off West Africa subject to Saharan dust, Reddy *et al.* [1990] found a mean $\tau_a(550)$ of 0.4 with $\tau_a(865) \approx 0.3$, in agreement with the observations of Korotaev *et al.* [1993], $\tau_a(550) \sim 0.3$ to 0.5. In areas subject to urban pollution, even higher optical thicknesses are observed, e.g., Reddy *et al.* [1990] found a mean $\tau_a(550) \approx 0.5$ and $\tau_a(865) \approx 0.3$ in the Western North Atlantic in summer when trajectory analysis suggested the origin of the air mass was the North American continent.

Thus, direct observation suggests that over the open ocean most of the aerosol is in the marine boundary layer and, for mean conditions $\tau_a(865) \approx 0.1$. Furthermore, the size distribution is

either similar to Haze C with $\nu \approx 2.5$ or bimodal like M80 or C80. Such aerosols would have $\varepsilon(765, 865) < 1.1$ (Figure 5). Figure 6a (open symbols) with $\varepsilon(765, 865) < 1.1$ is appropriate to these mean conditions and shows that the single scattering CZCS-type algorithm should be capable of retrieving $[\rho_w(443)]_N$ with the desired accuracy. For the maximum $\tau_a(865)$ (~ 0.19), Figure 6b is appropriate and under the same conditions for maximum end of the observed $\tau_a(865)$ range, and for most of the geometries good retrievals are obtained, although in some cases, the error is outside the acceptable range.

For situations with a strong continental influence, e.g., Saharan dust or urban pollution carried over the oceans by the wind, the aerosol is likely to be at least moderately absorbing. Also, $\tau_a(\lambda)$ will be sufficiently large that aerosol single scattering will no longer be an adequate approximation. Thus, we are forced to consider a full multiple scattering approach.

3.1.1.2 Multiple Scattering Effects

Multiple scattering effects have already been shown [Deschamps, Herman and Tanre, 1983; Gordon, Brown and Evans, 1988; Gordon and Castaño, 1987] to be significant at the level of accuracy required for SeaWiFS and MODIS, i.e., $\Delta[\rho_w(443)]_N \approx 0.001 - 0.002$. Although the single scattering approach is seen to work well only for sufficiently small optical depth (Figure 6) and nonabsorbing aerosols, typically the case over the open ocean, we desire an algorithm that can cope with even extreme situations. To begin the study of the effects of multiple scattering, we examine the properties of the solutions to the RTE used in providing the pseudo data for Figure 6. Since we are ignoring sun glitter and whitecaps for the moment, we can assess the multiple scattering effects by noting that

$$\rho_t - \rho_r - t\rho_w = \rho_a + \rho_{ra} \xrightarrow{\text{Single Scattering}} \rho_{as}.$$

Thus, comparison of $\rho_t - \rho_r - t\rho_w$ and ρ_{as} provides a direct assessment of multiple scattering. Figures 7a and 7b provide such a comparison for the Tropospheric model with RH = 50% (T50) and the Maritime model with RH = 99% (M99). Note that for the Maritime aerosol for $\rho_{as} \gtrsim 0.01$, the value of $\rho_a + \rho_{ra}$ is about 40% greater than ρ_{as} , i.e., multiple scattering significantly increases the reflectance due to the aerosol. In contrast, for the Tropospheric model at RH = 50% the aerosol reflectance is only increased by $\sim 10\%$. Thus, we see that the influence of multiple scattering depends significantly on the aerosol model. In contrast to the algorithm in Section 3.1.1.1.2, for

which multiple scattering was ignored, and for which no knowledge of the aerosol properties was required to effect the atmospheric correction, the model-dependent multiple scattering will make it necessary to utilize aerosol models in the ρ_w retrieval algorithm.

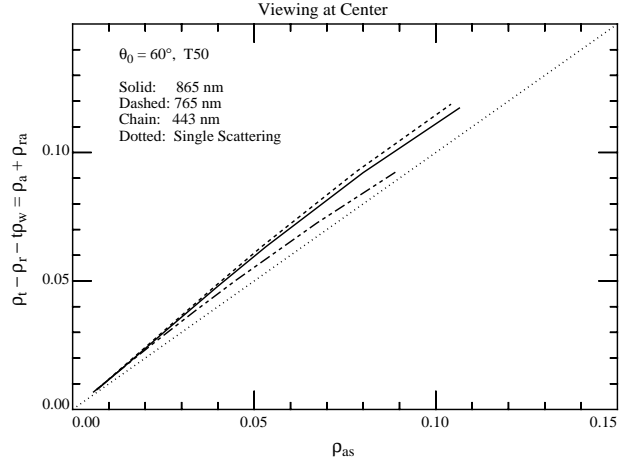


Figure 7a. $\rho_a(\lambda) + \rho_{ra}(\lambda)$ as a function of $\rho_{as}(\lambda)$ for aerosol model T50 at $\theta_0 = 60^\circ$ and nadir viewing.

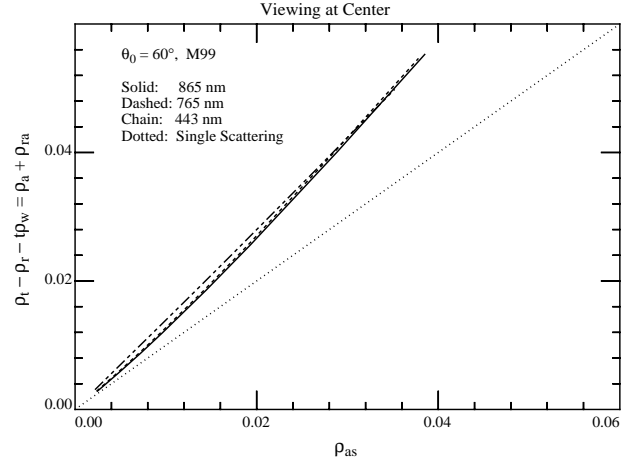


Figure 7b. $\rho_a(\lambda) + \rho_{ra}(\lambda)$ as a function of $\rho_{as}(\lambda)$ for aerosol model M99 at $\theta_0 = 60^\circ$ and nadir viewing.

3.1.1.3 The Multiple-Scattering Retrieval Algorithm

From the last section it should be clear that a way must be found to deal with multiple scattering. However, the success of the single-scattering algorithm at low values of τ_a , and the fact that the only *direct* link to the aerosol models is through $\varepsilon(\lambda, \lambda_l)$, or in particular through $\varepsilon(\lambda_s, \lambda_l)$, it seems reasonable to retain the formalism of the single scattering algorithm, but modify it to include multiple scattering. This is the approach taken here. Writing

$$\rho_a(\lambda) + \rho_{ra}(\lambda) = K[\lambda, \rho_{as}(\lambda)]\rho_{as}(\lambda),$$

where the dependence of K on $\rho_{as}(\lambda)$ represents the departure of the $\rho_a(\lambda) + \rho_{ra}(\lambda)$ versus $\rho_{as}(\lambda)$ relationship from linearity, we see that K is nearly the same for the two NIR bands, but can be significantly different at 443 nm (Figure 7a). It is irrelevant whether the dependence of K on λ is explicit ($K = K[\lambda]$) or implicit ($K = K[\rho_{as}(\lambda)]$) or both, the effect is the same: Eq. (11) becomes

$$\Delta(t\rho_w(\lambda_i)) = \rho_t(\lambda_i) - \rho_r(\lambda_i) - \frac{K[\lambda_i, \rho_{as}(\lambda_i)]}{K[\lambda_l, \rho_{as}(\lambda_l)]}\varepsilon(\lambda_i, \lambda_l)[\rho_a(\lambda_l) + \rho_{ra}(\lambda_l)],$$

and the $\rho_a(\lambda) + \rho_{ra}(\lambda)$ versus $\rho_{as}(\lambda)$ relationship must be known at each wavelength.

Gordon and Wang [1994b] solved the RTE for a set of N candidate aerosol models to provide what is essentially a set of lookup tables for $K[\lambda, \rho_{as}(\lambda)]$. As in the single scattering algorithm, the NIR bands are used to provide the aerosol model through

$$\varepsilon(\lambda_s, \lambda_l) = \frac{K[\lambda_l, \rho_{as}(\lambda_l)]}{K[\lambda_s, \rho_{as}(\lambda_s)]} \left[\frac{\rho_a(\lambda_s) + \rho_{ra}(\lambda_s)}{\rho_a(\lambda_l) + \rho_{ra}(\lambda_l)} \right];$$

however, since the aerosol model is not known at this point, the K ratio is unknown. Figure 7 suggests that this K ratio should not deviate significantly from unity, so *Gordon and Wang* [1994b] proposed computing $\varepsilon(\lambda_s, \lambda_l)$ though

$$\varepsilon(\lambda_s, \lambda_l) = \frac{1}{N} \sum_{j=1}^N \varepsilon_j(\lambda_s, \lambda_l),$$

where $\varepsilon_j(\lambda_s, \lambda_l)$ is the value of $\varepsilon(\lambda_s, \lambda_l)$ derived from $\rho_a(\lambda_l) + \rho_{ra}(\lambda_l)$ and $\rho_a(\lambda_s) + \rho_{ra}(\lambda_s)$ by assuming that the K ratio for the j^{th} aerosol model is correct. This procedure works reasonably well because the values of ε_j derived using the individual models are all close to the correct value. The procedure has been further modified by recomputing a new average formed by dropping the two models with the largest values of $\varepsilon(\lambda_s, \lambda_l) - \varepsilon_j(\lambda_s, \lambda_l)$ and the two models with the most negative values. This procedure is carried out several times until the final value is computed using four models: two with $\varepsilon - \varepsilon_j < 0$ and two models with $\varepsilon - \varepsilon_j > 0$.

Having derived a value for $\varepsilon(\lambda_s, \lambda_l)$, the next task is to estimate $\varepsilon(\lambda_i, \lambda_l)$. In general, the derived value of $\varepsilon(\lambda_s, \lambda_l)$ will be bracketed by two of the N candidate aerosol models. We then assume that $\varepsilon(\lambda_i, \lambda_l)$ falls between the same two aerosol models proportionately in the same manner as $\varepsilon(\lambda_s, \lambda_l)$. Finally, we also assume that $K[\lambda_i, \rho_{as}(\lambda_i)]$ falls between the two values for these models in the same proportion as $\varepsilon(\lambda_s, \lambda_l)$. These assumptions are required to proceed, and as we shall see, they are not always true. However, to the extent that the actual aerosols are similar in their optical properties to the candidate models, the assumptions appear to be reasonably valid.

At present, twelve candidate aerosol models are used: the Maritime, Coastal, and Tropospheric models with RH = 50, 70, 90, and 99%. Tables of the $\rho_a(\lambda) + \rho_{ra}(\lambda)$ versus $\rho_{as}(\lambda)$ relationship were constructed by solving the RTE for each model for $\theta_0 = 0$ to 80° in increments of 2.5° , and at 33 values of θ_v . The azimuthal dependence of the reflectance was determined through Fourier analysis. Computations were carried out for eight values of $\tau_a(\lambda_i)$ from 0.05 to 0.8. The total number of separate solutions to the RTE used in the preparation of the tables exceeded 33,000 (including the

four Urban models used later). To reduce storage, for a given set (θ_0, θ_v) the simulations were fit to

$$\log[\rho_t(\lambda) - \rho_r(\lambda) - t\rho_w(\lambda)] = \log[a(\lambda)] + b(\lambda) \log[\rho_{as}(\lambda)] + c(\lambda) \log^2[\rho_{as}(\lambda)] \quad (12)$$

by least-squares. In the case of the azimuth angle ϕ_v , we expanded $a(\lambda)$, $b(\lambda)$ and $c(\lambda)$ in a Fourier series in ϕ_v and stored only the Fourier coefficients. As the reflectances are even functions of the relative azimuth angle ϕ_v , $a(\lambda)$, $b(\lambda)$, and $c(\lambda)$ will be even functions of ϕ_v . Thus, we can write

$$a(\theta_v, \theta_0, \phi_v, \lambda) = a^{(0)}(\theta_v, \theta_0, \lambda) + 2 \sum_{m=1}^M a^{(m)}(\theta_v, \theta_0, \lambda) \cos m\phi_v,$$

with

$$a^{(m)}(\theta_v, \theta_0, \lambda) = \frac{1}{\pi} \int_0^\pi a(\theta_v, \theta_0, \lambda, \phi_v) \cos m\phi_v d\phi_v,$$

etc. Using Fourier analysis with $M = 14$ produced about the same accuracy in the results as interpolating with an increment in ϕ_v of 5° or 10° .

3.1.1.4 Simulated Test of the Multiple-Scattering Algorithm

We have tested this multiple-scattering algorithm by applying it to pseudo data created using the *Shettle and Fenn* [1979] Tropospheric, Coastal, Maritime, and Urban models at RH = 80%, denoted by T80, C80, M80, and U80, respectively. Note that these are *not* part of the candidate aerosol set, although the size and refractive index distributions of T80, C80, and M80 are similar to members of the set. In contrast to the others, and unlike any members of the candidate set, U80 has strong aerosol absorption.

Comparison between the single-scattering and multiple-scattering algorithms for pseudo data created with these models at the seven sun-viewing geometries described earlier is provided in Figure 8 for $\tau_a(865) = 0.2$. Clearly, including multiple scattering in the algorithm significantly improves the retrieval of $[\rho_w(443)]_N$ for the T80, C80, and M80 cases, for which $\tau_a(443) \approx 0.50$, 0.32, and 0.24, respectively (Figures 4a and 5). In contrast, the U80 retrievals, although somewhat improved over single scattering, are still very poor. Thus, even though the size distribution of the U80 model is similar to the candidates (both in modal diameter and standard deviation), the fact that the particles are strongly absorbing causes as large an error in the retrieval of $[\rho_w(443)]_N$ as neglecting multiple scattering completely. Clearly, particle absorption must have a profound impact on multiple scattering.

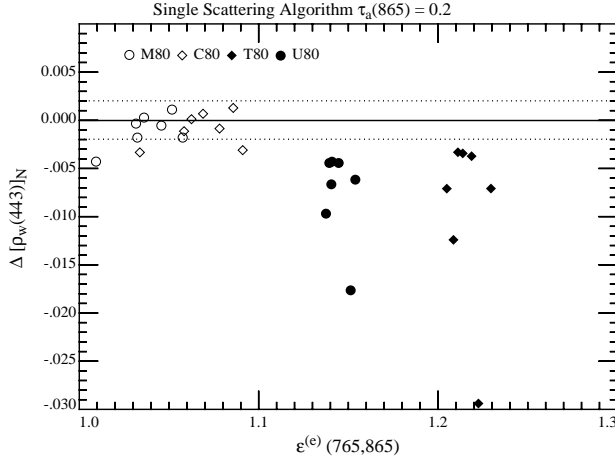


Figure 8a. $\Delta[\rho_w(443)]_N$ as a function of $\epsilon^{(e)}(765,865)$ for $\tau_a(865) = 0.2$ and all of the viewing geometries examined in the study, using the single-scattering algorithm.

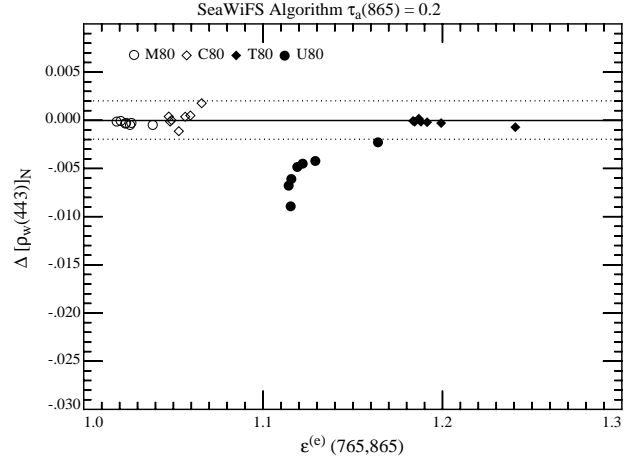


Figure 8b. $\Delta[\rho_w(443)]_N$ as a function of $\epsilon^{(e)}(765,865)$ for $\tau_a(865) = 0.2$ and all of the viewing geometries examined in the study, using the multiple-scattering algorithm.

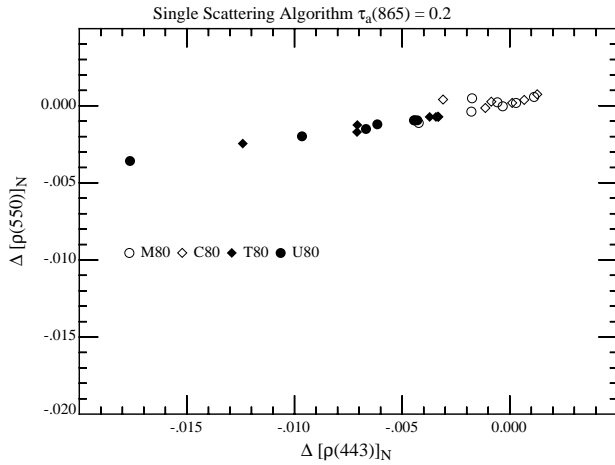


Figure 8c. $\Delta[\rho_w(550)]_N$ as a function of $\Delta[\rho_w(443)]_N$ for the results in Figure 8a.

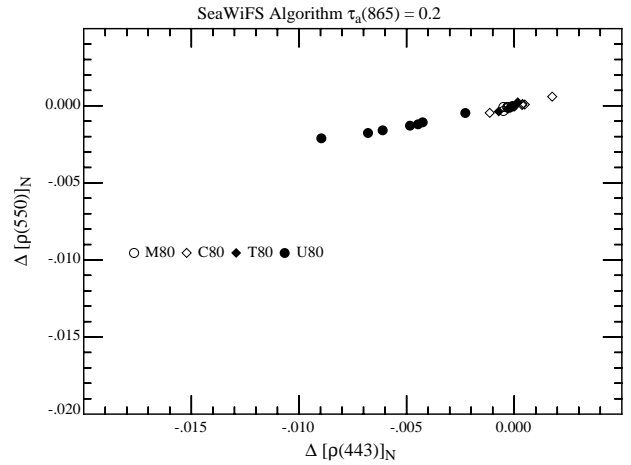


Figure 8d. $\Delta[\rho_w(550)]_N$ as a function of $\Delta[\rho_w(443)]_N$ for the results in Figure 8b.

As in Figures 6c and 6d, Figures 8c and 8d provide the relationship between $[\rho_w(550)]_N$ and $[\rho_w(443)]_N$ for the single-scattering and the multiple-scattering (SeaWiFS) algorithms. For the multiple-scattering algorithm, $\Delta[\rho_w(550)]_N \approx (1/4)\Delta[\rho_w(443)]_N$, and with the exception of very low pigment concentrations, the error in atmospheric correction at 443 nm will contribute more significantly to the error in R [Eq. (4)] than that at 550 nm. Fortuitously, the errors at 443 and 550 nm typically have the same sign and, therefore, tend to cancel in R .

Table 2: Mean value of C obtained for seven viewing geometries and three aerosol models (M80, C80, and T80). The number in parenthesis is the standard deviation divided by the mean (in %).

$\tau_a(865)$	$C_{\text{True}} = 0.10$ mg/m ³	$C_{\text{True}} = 0.47$ mg/m ³	$C_{\text{True}} = 0.91$ mg/m ³
0.1	0.101 (1.6)	0.466 (3.4)	0.912 (9.1)
0.2	0.100 (3.1)	0.470 (4.7)	0.940 (12.8)
0.3	0.098 (5.5)	0.493 (15.3)	0.936 (25.3)

The error in the pigment concentration induced by $\Delta[\rho_w(550)]_N$ and $\Delta[\rho_w(443)]_N$ in the multiple-scattering algorithm is provided in Table 2. To prepare this table, the errors were added to values of $[\rho_w(550)]_N$ and $[\rho_w(443)]_N$ that are characteristic of three pigment concentrations (0.10, 0.47, and 0.91 mg/m³) in order to produce retrieved reflectances that include the atmospheric correction error. These were then inserted into Eq. (4) and the resulting pigment concentration was derived for each sun-viewing geometry for the M80, C80, and T80 aerosol models. For each true pigment concentration, the twenty-one retrieved values of C (seven geometries times three aerosol models) were averaged and the standard deviation was computed. The computations were carried out for $\tau_a(865) = 0.1, 0.2$, and 0.3 .

As expected, the quality of the retrievals is best for the smallest value of $\tau_a(865)$. Excellent retrievals of C (as indicated by excellent mean values and small relative standard deviations) were obtained for $\tau_a(865) = 0.1$ and 0.2 , and for the two lower concentrations for $\tau_a(865) = 0.3$. As mentioned earlier, $\tau_a(865)$ is typically $\lesssim 0.2$ in regions not subjected to urban pollution or desert dust. For $\tau_a(865) = 0.3$ and a true value of C of 0.91 mg/m³, one retrieved value of C was ≈ 9 mg/m³ ($\theta_0 = 60^\circ$, $\theta_v \approx 45^\circ$, T80, for which $\tau_a(443) \approx 0.75$ and $\tau_a(550) \approx 0.6$). This value was not included in the average or the standard deviation computation. These results suggest that the multiple-scattering algorithm will provide excellent results as long as the candidate aerosol models are similar in size and composition to the aerosol actually present.

To try to understand the effect of particle absorption on multiple scattering, a set of multiple scattering computations of $\rho_a + \rho_{ra}$ was carried out in which particle absorption *alone* was varied. Specifically, we used the phase functions for the T50 and M99 aerosol models evaluated at 865 nm (Figure 9). These models have the most weakly (T50) and the most strongly (M99) forward peaked scattering phase function among the candidate models. Simulations of $\rho_a + \rho_{ra}$ as a function of τ_a (or equivalently ρ_{as}) were made for $\theta_0 = 60^\circ$ and $\theta_v \approx 1^\circ$, with $\tau_r = 0.015$ (865 nm) and 0.236 (443 nm), as ω_a assumed the values of 0.6, 0.8, and 1.0. The results are presented in Figure 10. Two facts concerning the $\rho_a + \rho_{ra}$ versus ρ_{as} relationship emerge from these simulations. First, for $\omega_a = 1$, the relationship is nearly linear and, for the sharply peaked M99 phase function, the Rayleigh-aerosol interaction (\sim the difference between the dashed and solid curves caused by changing τ_r) is small,

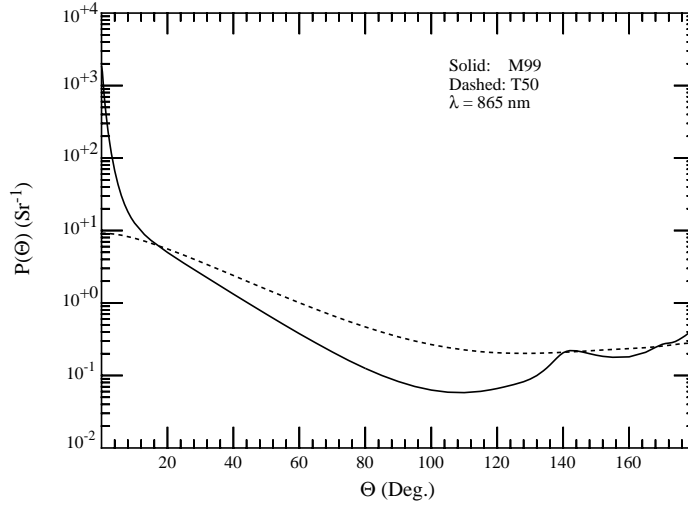


Figure 9. Scattering phase functions for the T50 and M99 aerosol models at 865 nm.

while for the smoother T50 phase function the Rayleigh-aerosol interaction is significantly larger. This is to be expected, since the mid-angle scattering by T50 is much larger than M99 (Figure 9). Second, as ω_a decreases, there are greater departures from linearity and an increase in the significance of the Rayleigh-aerosol interaction for *both* T50 and M99. The general shape of the curves is explained by the fact that $\rho_a + \rho_{ra}$ must approach an asymptotic value as $\tau_a \rightarrow \infty$. Also, increasing τ_r causes more diffuse light to enter the aerosol layer and traverse longer paths through it, with the concomitant greater chance of absorption. This explains the strong influence of ω_a on ρ_{ra} .

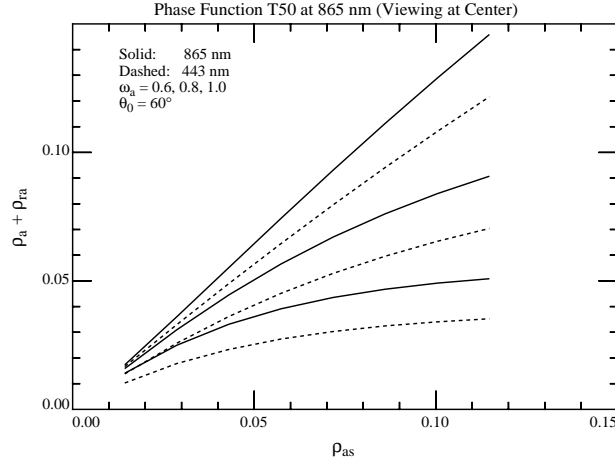


Figure 10a. $\rho_a + \rho_{ra}$ as a function of ρ_{as} and ω_a for 443 nm (dashed) and 865 nm (solid) and the T50 phase function. Curves from bottom to top correspond to $\omega_a = 0.6, 0.8$, and 1.0 .

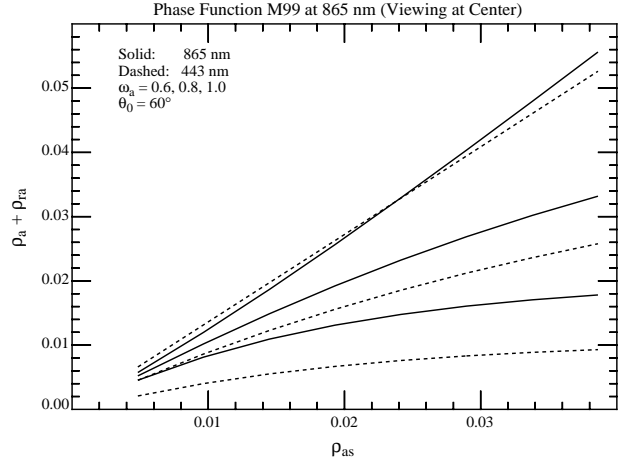


Figure 10b. $\rho_a + \rho_{ra}$ as a function of ρ_{as} and ω_a for 443 nm (dashed) and 865 nm (solid) and the M99 phase function. Curves from bottom to top correspond to $\omega_a = 0.6, 0.8$, and 1.0 .

The impact of the absorption in Figure 10 is serious. Consider a hypothetical situation in which the M99 phase function is appropriate and $\epsilon(\lambda_i, \lambda_l) = 1$, so $\rho_{as}(\lambda_i) = \rho_{as}(\lambda_l)$. Also, assume that $\epsilon(\lambda_i, \lambda_l)$ is correctly determined by the algorithm and that $\rho_a + \rho_{ra} \approx 0.02$ at 865 nm. Then, if $\omega_a = 1$ were used for estimating $\rho_a + \rho_{ra}$ at 443 nm, but the true value of ω_a was actually 0.8, Figure 10b shows that the error in $\rho_a + \rho_{ra}$ at 443 nm would be ~ -0.004 . In contrast, if the $\omega_a = 1$ assumption was correct the error would be $\sim +0.001$. Clearly, the effect of absorption is to produce large negative errors in $t\rho_w$, i.e., to overestimate the effect of the atmosphere. Figure 3a suggests that when $\epsilon(\lambda_i, \lambda_l)$ is estimated from $\epsilon(\lambda_s, \lambda_l)$ using weakly- or nonabsorbing aerosol models, it will be overestimated, i.e., $\epsilon(\lambda_i, \lambda_l)$ will be too large, if the aerosol strongly absorbs. This effect will cause a further overestimation of the atmospheric effect.

As the twelve candidate models in Section 3.1.1.3 are combinations of two components with physical properties dependent on RH, they represent a fixed set of values of ω_a at each wavelength, i.e., there are only twelve different values of ω_a . At 865 nm, these range from 0.99857 (M99) to 0.92951 (T50). Furthermore, each model possesses a unique value of $\epsilon(\lambda_s, \lambda_l)$ and a more or less unique value of $\epsilon(\lambda_i, \lambda_l)$ for a given sun-viewing geometry (Figure 3a). Thus, the choice of the twelve candidates forces a definite relationship between ω_a and $\epsilon(\lambda_i, \lambda_l)$. In the case of the twelve models chosen here, there is a steady decrease in ω_a with increasing $\epsilon(\lambda_i, \lambda_l)$. If this relationship is more or less correct, an excellent correction is effected (Figure 8b, T80); however, with its low

value of ω_a (0.74806 for U80 at 865 nm) the Urban model falls considerably outside this relationship and the resulting atmospheric correction is very poor (U80 in Figure 8b). This is further shown in Figure 11 in which the multiple-scattering algorithm is applied to the Haze C models. In this Figure we have limited the models to those that fall within the range of variation of the values of $\varepsilon(\lambda_s, \lambda_l)$ of the candidate models, and also models for which $\tau_a(443) \lesssim 0.8$, the upper limit of τ_a used in the preparation of the $\rho_a + \rho_{ra}$ versus ρ_{as} look up tables. Haze C models with a real index of refraction ($\omega_a = 1$) and $\nu \geq 3$ do not follow the $\omega_a - \varepsilon(\lambda_s, \lambda_l)$ relationship implied by the candidate models, and the values of $\Delta[\rho_w(443)]_N$ are positive. In contrast, the dust and mineral models both display ω_a -values less than T50, and for these the $\Delta[\rho_w(443)]_N$ are large and negative. Thus, it should be clear that it is imperative to use candidate aerosol models that possess an approximately correct relationship between ω_a and $\varepsilon(\lambda_s, \lambda_l)$, or physically, an approximately correct relationship between particle size and absorption. Such a relationship must be based on climatology, e.g., when the aerosol optical thickness over the North Atlantic Saharan dust zone is high, one should use

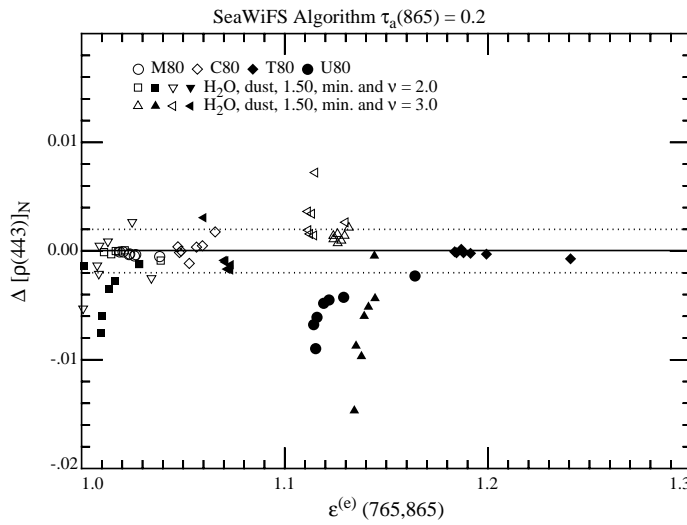


Figure 11. $\Delta[\rho_w(443)]_N$ as a function of $\varepsilon^{(e)}(765, 865)$ for the Haze C models with $\tau_a(865) = 0.2$ and all of the viewing geometries examined in the study, using the multiple-scattering algorithm.

candidate models consisting of a linear combination of a Maritime model and Saharan dust model, either uniformly mixed in the marine boundary layer or having a two-layer structure. Given such climatology-based models, preparation of the appropriate lookup tables for incorporation into the algorithm is a simple process.

As an example, we modified the algorithm to utilize only four candidate models, the *Shettle and Fenn* [1979] Urban models at RH = 50%, 70%, 90%, and 99%, and tested it using pseudo data created with the U80 model. In this manner, the ω_a and $\varepsilon(\lambda_s, \lambda_l)$ relationship was approximately correct. The results are provided in Figure 12, which shows the error in $[\rho_w(443)]_N$ as a function of the aerosol optical thickness of U80 at 865 nm. Recall, from Figure 4a, that $\tau_a(443) \approx 1.75\tau_a(865)$. Comparison with Figure 11, for which $\tau_a(865) = 0.2$, shows that the maximum error (which occurs at the scan edge with $\theta_0 = 60^\circ$), when the Urban models are used as candidates, is only twice the minimum error when the original twelve candidate aerosol models were used. This underscores the necessity of having realistic climatologically-based aerosol models in situations in which the aerosol

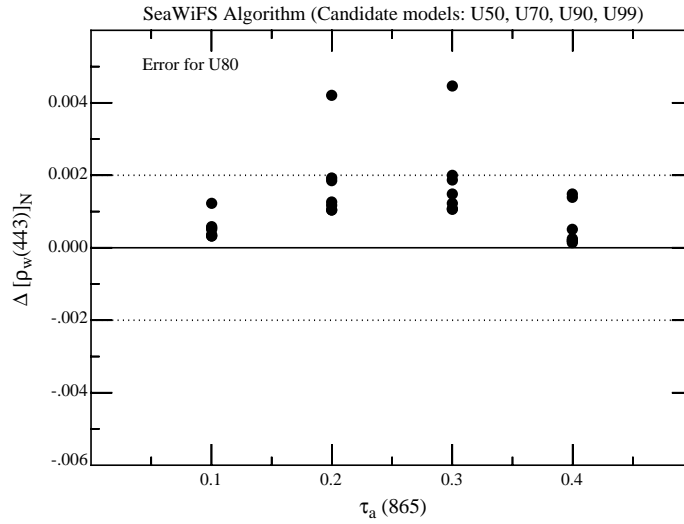


Figure 12. $\Delta[\rho_w(443)]_N$ as a function of $\tau_a(865)$ for the U80 model, when the candidate aerosol models in the multiple-scattering algorithm are restricted to U50, U70, U90, and U99.

concentration is sufficiently large to require consideration of multiple scattering. We shall discuss experimental efforts to obtain such a climatology in a later section.

3.1.1.5 Estimation of Aerosol Optical Depth τ_a

There is considerable interest now in the global distribution of aerosols because of their role in climate forcing and biogeochemical cycling [Charlson *et al.*, 1992]. The hypothesis [Charlson *et al.*, 1987] that dimethylsulfide (DMS) from phytoplankton activity leads to an increase in cloud

condensation nuclei in the marine atmosphere argues for simultaneous study of aerosols and productivity where possible [Falkowski *et al.*, 1992]. There has been effort in recent years directed toward estimating the aerosol concentration ($\propto \tau_a$) and other properties using Earth-orbiting satellites [Durkee *et al.*, 1986; Fraser, 1976; Griggs, 1975; Griggs, 1981; Griggs, 1984; Griggs, 1981; Koepke and Quenzel, 1979; Koepke and Quenzel, 1981; Mekler *et al.*, 1977; Rao *et al.*, 1988]. In this section we show that τ_a can be retrieved with a simple extension of the atmospheric correction algorithm.

Even in the single scattering approximation, one notes from Eq. (9) that it is not possible to estimate τ_a without assuming a model for the aerosol to provide ω_a and P_a . For example, Rao *et al.* [1988] assume that the aerosol consists of spherical particles with a size frequency distribution $\propto (\text{radius})^{-4.5}$ and a refractive index of 1.5. The assumption of an incorrect model can produce significant errors (up to a factor of 2–3) in the recovered τ_a . As in atmospheric correction, we will try to avoid using an incorrect model in the retrieval of τ_a by utilizing the only other aerosol information available on a pixel-by-pixel basis — the spectral variation of ρ_{as} .

Our retrieval algorithm is a simple extension of the atmospheric correction algorithm, i.e., the correction algorithm yields the two models which most closely bracket $\varepsilon(765, 865)$, and we use these two models to invert Eq. (9) to obtain two estimates of τ_a . As with the atmospheric correction, it is necessary to know the absorption properties of the aerosol. Assuming the aerosols are weakly absorbing, i.e., that the aerosol consists of particles that are accurately described by the Maritime, Coastal, or Tropospheric aerosol models with RH = 80%, ρ_t is simulated for this aerosol and inserted into the multiple-scattering atmospheric correction algorithm. The correction algorithm provides two candidate models based on $\varepsilon(765, 865)$ and these specify two sets of P_a and ω_a values for two estimates of τ_a . These estimates are then averaged to yield the final estimate of τ_a . Tables 3 and 4 provide the % error in the retrieved $\tau_a(865)$ for three aerosol models at the center and the edge of the MODIS scan as a function of θ_0 . The true value of $\tau_a(865)$ was 0.2 or 0.4. All the calculations were carried out for $\phi_v = 90^\circ$. From the tables, we can see that the error in the retrieved aerosol optical thickness is within $\pm 10\%$ (and usually considerably less) for most of the cases examined. We also tried determining τ_a from the weighted average of the two estimates as in the correction algorithm; however, this led to a slightly poorer retrieval.

Finally, it is of interest to estimate the upper limit to the value of $\tau_a(865)$ that can be estimated with SeaWiFS or MODIS given its design saturation reflectance (ρ_{\max}). This is dependent on the particular aerosol model because for a given τ_a the backscattering (scattering at angles $> 90^\circ$) is

Table 3: Error in retrieved $\tau_a(865)$
for viewing at the center and edge of
the scan. The true value of $\tau_a(865)$ is 0.20.

Position	θ_0	Error (%) in $\tau_a(865)$		
		Maritime	Coastal	Tropospheric
Center	20°	+10.9	−4.74	+2.02
	40°	−2.96	−5.04	+0.62
	60°	−0.31	−4.57	+0.94
Edge	0°	−1.36	−2.69	+0.43
	20°	−1.39	−3.73	+0.13
	40°	−1.75	−5.45	−0.29
	60°	−0.92	−5.74	+0.65

Table 4: Error in retrieved $\tau_a(865)$
for viewing at the center and edge of
the scan. The true value of $\tau_a(865)$ is 0.40.

Position	θ_0	Error (%) in $\tau_a(865)$		
		Maritime	Coastal	Tropospheric
Center	20°	+9.99	−6.40	+1.01
	40°	−1.82	−6.36	+1.00
	60°	+0.83	−3.63	+1.32
Edge	0°	−0.52	−2.45	+0.99
	20°	−0.24	−2.99	+0.93
	40°	+0.03	−3.77	+0.90
	60°	+0.85	−3.95	+1.37

Table 5: Value of $\tau_a(865)$ required to
saturate SeaWIFS/MODIS at 865 nm.

Position	θ_0	Maximum value of $\tau_a(865)$	
		Maritime (RH = 98%)	Tropospheric (RH = 70%)
Center	20°	0.72	0.54
	40°	1.04	0.72
	60°	1.69	0.80
Edge	0°	0.88	0.51
	20°	0.98	0.51
	40°	1.04	0.50
	60°	1.02	0.50

strongly dependent on the aerosol size distribution and the refractive index. We estimate the upper limit of $\tau_a(865)$ that can be estimated by using the Tropospheric model with RH = 70% (the *largest* backscattering of the models used here) and the Maritime model with RH = 98% (the *smallest* backscattering). The results are presented in Table 5.

3.1.1.6 Whitecap Removal Algorithm

As mentioned earlier, the term $t(\lambda_i)\rho_{wc}(\lambda_i)$ in Eq. (6) has been ignored in the development of the algorithm. If we indicate the reflectance measured at the top of the atmosphere as $\rho_t^{(m)}$, this reflectance consists of two parts; that which would be measured in the absence of whitecaps, and the reflectance added by the whitecaps $t\rho_{wc}$, i.e.,

$$\rho_t^{(m)} = \rho_t + t\rho_{wc}. \quad (13)$$

Since the $[\rho_w]_N$ -retrieval algorithm must be operated with ρ_t rather than $\rho_t^{(m)}$, $t\rho_{wc}$ must be removed from the imagery *before* the algorithm can be applied.

As in the case of the normalized water-leaving radiance, we define the normalized whitecap reflectance (or the albedo) $[\rho_{wc}]_N$ to be the area-weighted reflectance (over several pixels) of oceanic whitecaps *at* the sea surface in the absence of the atmosphere. Then the whitecap component of the radiance leaving the surface is

$$L_{wc}(\lambda) = [\rho_{wc}(\lambda)]_N \frac{F_0 \cos \theta_0}{\pi} t(\theta_0, \lambda),$$

where the whitecaps are assumed to be lambertian. Converting to reflectance we have

$$\rho_{wc}(\lambda) = [\rho_{wc}(\lambda)]_N t(\theta_0, \lambda).$$

At the top of the atmosphere, the whitecaps contribute

$$t\rho_{wc}(\lambda) = [\rho_{wc}(\lambda)]_N t(\theta_0, \lambda)t(\theta_v, \lambda).$$

The problem faced in removing $t\rho_{wc}(\lambda)$ from $\rho_t(\lambda)$ in Eq. (6) is the estimation of $[\rho_{wc}(\lambda)]_N$.

Based on previous research on the relationship between whitecaps and environmental parameters, the algorithm adopted for estimating $[\rho_{wc}]_N$ is that of *Koepke [1984] [Gordon and Wang, 1994a]*:

$$[\rho_{wc}]_N = 6.49 \times 10^{-7} W^{3.52}, \quad (14)$$

where W is the wind speed in m/s measured 10 m above the sea surface. Figure 13 provides Koepke's $[\rho_{wc}]_N$ as a function of W , along with derived data from *Monahan* [1971]. It shows that Eq. (14) predicts $[\rho_{wc}]_N$ with a standard deviation approximately equal to $[\rho_{wc}]_N$ itself.

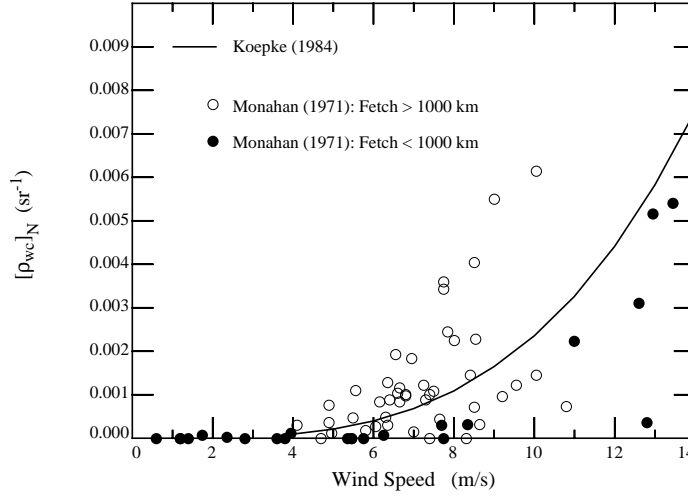


Figure 13. $[\rho_{wc}]_N$ (solid line) as a function of wind speed. Points are computed using the data from *Monahan* [1971].

The effect of the any error in the estimation of $[\rho_{wc}]_N$ on the retrieved water-leaving reflectance is strongly dependent on the spectral variation of $[\rho_{wc}(\lambda)]_N$. In *Gordon and Wang* [1994a] it was assumed, based on measurements carried out by *Whitlock, Bartlett and Gurganus* [1982], that $[\rho_{wc}(\lambda)]_N$ was independent of λ ; however, *Schwindling* [1995] and *Frouin, Schwindling and Deschamps* [1996] have reported measurements on breaking waves in the surf zone suggesting that whitecaps may reflect considerably less in the NIR than in the visible, presumably because a significant component of the whitecap reflectivity is due to scattering from submerged bubbles. To understand the effect of spectral variation in $[\rho_{wc}]_N$ on the accuracy of atmospheric correction, the multiple scattering algorithm has been operated in the presence of whitecaps displaying both non-spectral reflectance and the spectral reflectance suggested by *Frouin, Schwindling and Deschamps* [1996]. Figure 14 compares the error in $[\rho_w(443)]_N$ as a function of θ_0 for viewing at the edge of the MODIS scan with the M80 aerosol model ($\tau_a(865) = 0.2$) for these two cases when the error in the estimate of $[\rho_{wc}]_N$ at 443 nm is ± 0.002 . This error in $[\rho_{wc}(443)]_N$ corresponds to a wind speed of $\sim 8 - 9$ m/s. Figure 14 shows that for wavelength-independent whitecap reflectivity,

the resulting error in $[\rho_w(\lambda)]_N$ can be significantly less ($\sim 1/4$) than the error in the estimate of

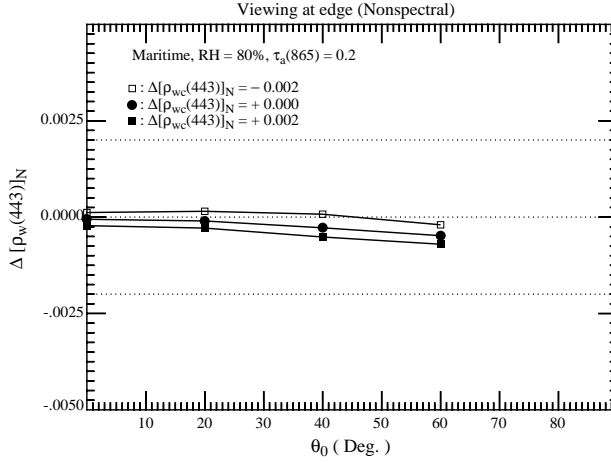


Figure 14a. $\Delta[\rho_w(443)]_N$ as a function of the error in the whitecap reflectance at 443 nm and θ_0 at the edge of the scan for the M80 aerosol model with $\tau_a(865) = 0.2$. Whitecap reflectance spectrum is that proposed by *Whitlock, Bartlett and Gurganus* [1982].

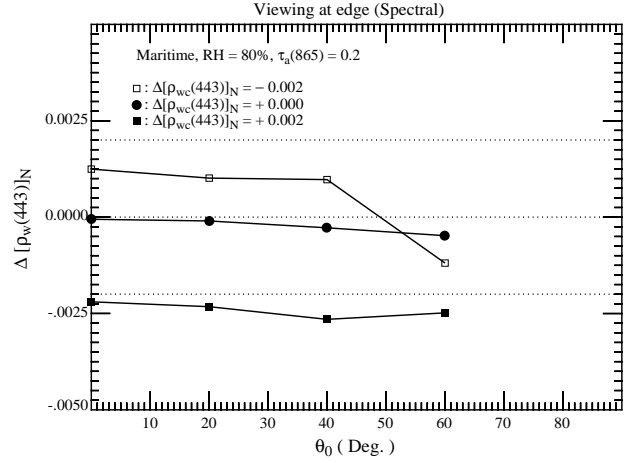


Figure 14b. $\Delta[\rho_w(443)]_N$ as a function of the error in the whitecap reflectance at 443 nm and θ_0 at the edge of the scan for the M80 aerosol model with $\tau_a(865) = 0.2$. Whitecap reflectance spectrum is that proposed by *Frouin, Schwindling and Deschamps* [1996].

$[\rho_{wc}(443)]_N$. In contrast, if whitecaps reflect in a manner consistent with the *Frouin, Schwindling and Deschamps* [1996] observations, the error in $[\rho_w(443)]_N$ can be expected to be of the same order-of-magnitude as the error in $[\rho_{wc}(443)]_N$. Similar simulations using the T80 aerosol model, for which $\epsilon(\lambda, 865)$ displays strong variation with λ , show similar effects for the case of whitecaps with the *Frouin, Schwindling and Deschamps* [1996] reflectance; however, the error for the *Whitlock, Bartlett and Gurganus* [1982] reflectance model can also be the same order of magnitude as $\Delta[\rho_{wc}(443)]_N$ [Gordon and Wang, 1994a]. Figure 14 shows that an overestimation of $[\rho_{wc}(443)]_N$ leads to a negative error in $[\rho_w(443)]_N$. The same is true at 550 nm. When the errors in $[\rho_w(\lambda)]_N$ are negative, algorithms such as Eq. (4), that use radiance ratios, can lead to very large errors in the derived products. Because of this, it is better to underestimate the $[\rho_{wc}(443)]_N$ in the whitecap correction algorithm rather than overestimating it.

As whitecaps have the potential of producing errors of a magnitude similar to the magnitude of the acceptable error in $[\rho_w(\lambda)]_N$, it is important to obtain radiometric data of actual oceanic whitecaps, and validate its dependence on wind speed. In particular, it is critical to understand the spectral dependence of $[\rho_{wc}]_N$ in the NIR. Our approach this was to construct a ship-based radiometer for observing whitecaps while the ship is on station or underway. The radiometer, suspended from a boom off the bow of the ship, continuously views a spot about 12 cm in diameter

on the sea surface. A video image, from a TV camera mounted along side of the radiometer to visually observe the water surface, is used to reject sun glitter. A second radiometer on the deck of the ship records the incident irradiance. The reflectance of the surface measured by the radiometer is recorded as a function of time (~ 7 samples/sec). This reflectance consists of background reflectance (low) from whitecap-free areas (the predominant situation) and a much higher reflectance whenever a portion of a whitecap is in the field of view of the radiometer. After determining the reflectance of the whitecap-free areas (essentially the “baseline” of the reflectance), and subtracting it from the entire record, we are left with the time-average reflectance due to the whitecaps, $\langle \rho_{wc}(\lambda) \rangle$. Clearly, $\rho_{wc}(\lambda) = \langle \rho_{wc}(\lambda) \rangle$, so

$$[\rho_{wc}(\lambda)]_N = \langle \rho_{wc}(\lambda) \rangle / t(\theta_0, \lambda).$$

The radiometer is accompanied by a meteorological package to provide the speed of the wind relative to the ship (and other, possibly relevant, parameters) and a GPS unit to provide the absolute speed of the ship. Combining these will yield W . The whitecap radiometer records in 10 nm bands centered at 6 wavelengths: 410, 510, 550, 670, 750, and 860 nm, and the downward surface irradiance is measured in 5 bands, also 10 nm wide, centered at 410, 510, 550, 670, and 860 nm. Thus, we are able to study the validity of Eq. (14) throughout the relevant spectral region.

An example of two whitecaps passing under the radiometer (deployed from the NOAA ship *RV Malcolm Baldrige*, April 1996) is shown in Figure 15. The 96 consecutive samples shown are acquired over a period of ~ 15 seconds. In this example a large whitecap suddenly breaks in view of the radiometer with thick white foam (sample point 11) reaching a peak reflectance of $\sim 55\%$. Six traces are plotted representing the six radiometer channels. The lower trace corresponds to the 860 nm reflectance. The thick foam is temporarily replaced by a region of submerged bubbles and less thick foam (\sim sample points 13, 14, 15) and some thick foam comes into view again at sample point 17. At sample point 20 and 21 a thin layer of foam passes followed by the decaying thicker foam to about sample point 35. Sample points from about 35 to 55 show the reflectance of thinning residual foam. From 60 to about 75 the reflectance of the foam free water surface is shown and is suddenly followed by another whitecap of smaller magnitude (sample point 76) and continues to decay out to about sample point 96. The data clearly suggest a significant fall in the NIR reflectance of whitecaps in agreement with the measurements of *Frouin, Schwindling and Deschamps* [1996] in the surf zone. Analysis of this data set is continuing.

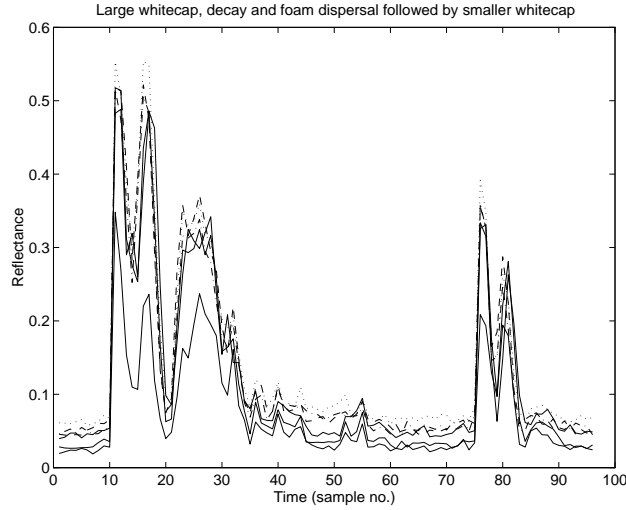


Figure 15. An ~ 15 second record of the reflectance of two whitecaps passing within the field of view of the radiometer. The lowest line corresponds to 860 nm.

3.1.1.7 Ancillary Data

Several sets of ancillary data are required to operate the $[\rho_w]_N$ retrieval algorithm. These are listed in Table 6. They may be needed on at most a $1^\circ \times 1^\circ$ latitude-longitude grid, but probably a coarser grid, e.g., $3^\circ \times 3^\circ$ will be sufficient considering the expected quality of some of the data. We will discuss each ancillary data set required below. MODIS Team Member Dr. Robert H. Evans of the University of Miami is researching the assembly of these required ancillary data sets.

3.1.1.7.1 Extraterrestrial Solar Irradiance F_0

Unless MODIS is calibrated directly in reflectance units, the extraterrestrial solar irradiance is required to convert from L_t to ρ_t . It is planned that this be taken from *Neckel and Labs* [1984] unless newer, more accurate, determinations become available in the future. In the event that MODIS is calibrated directly in reflectance units, this quantity is only needed to turn $[\rho_w]_N$ into the desired $[L_w]_N$.

3.1.1.7.2 Ozone Optical Thickness

Table 6: Quantities and required ancillary data.

Quantity	Ancillary Data
$\rho_t(\lambda_i)$	$F_0(\lambda_i)$
$\rho_r(\lambda_i)$	$\tau_{Oz}(\lambda_i), W, P_0$
$\rho_{wc}(\lambda_i)$	$W, \Delta T, T_W$
$\rho_g(\lambda_i)$	\vec{W}
$t(\lambda_i)$	$\tau_{Oz}(\lambda_i), P_0$
$T(\lambda_i)$	$\tau_{Oz}(\lambda_i), P_0, \tau_a(\lambda_i)$
$\epsilon(\lambda_i, \lambda_j)$	RH

In the radiative transfer model the atmosphere is assumed to be composed of three layers. The top is the Ozone layer and is nonscattering, the second is a molecular scattering layer and the third is the aerosol layer. The Ozone optical thickness $\tau_{Oz}(\lambda)$ is needed to compute the two way transmittance of ρ_r , ρ_w , ρ_{wc} and ρ_g through the Ozone layer. Since the Ozone absorption is small ($\tau_{Oz} \lesssim 0.035$) high accuracy is not needed. It is estimated that an error in the Ozone concentration of $\sim 20 - 40$ mAtm-cm (Dobson Units) could be tolerated. The source will either be MODIS itself (most convenient) or a sensor on the NOAA system.

3.1.1.7.3 Surface Atmospheric Pressure P_0

The atmospheric pressure is needed to compute the Rayleigh optical thickness (τ_r), that is required for the computation of ρ_r , and is used in the transmittances t and T . The value of τ_{r_0} , the Rayleigh optical thickness at the standard atmospheric pressure P_0 of 1013.25 mb is given by [Hansen and Travis, 1974]

$$\tau_{r_0} = 0.008569\lambda^{-4} (1 + 0.0113\lambda^{-2} + 0.00013\lambda^{-4}),$$

where λ is in μm . At any surface pressure P , the Rayleigh optical depth is

$$\tau_r = \frac{P}{P_0} \tau_{r_0}.$$

An error $< \pm 5$ mB should be sufficient for the computation of τ_a . The source of this data set will be the output of numerical weather models, probably from NMC.

3.1.1.7.4 Wind Speed W and Wind Vector \vec{W}

The wind speed, if known, is used in the computation of ρ_r , otherwise ρ_r is computed with $W = 0$. It is also required for the estimation of $[\rho_{wc}]_N$. The wind vector is required for the construction of a glint mask, i.e., a mask to remove areas contaminated by sun glint from the imagery before processing (Appendix A). The importance of creating a realistic mask is that good data may be masked if the mask is made in too conservative a manner. An error of $< 1 - 2$ m/s in the speed and $< 30^\circ$ on the direction should be sufficient. The source of this data set will be the output of numerical weather models, probably from NMC.

3.1.1.7.5 Sea Surface Temperature and Atmospheric Stability

These may be needed to estimate $[\rho_{wc}]_N$, if another estimate replaces Koepke's (Eq. (14)), e.g., *Monahan and O'Muircheartaigh* [1986]. An error of $< \pm 1^\circ\text{C}$ in the air-sea temperature difference ΔT (indicating the atmospheric stability) and the water temperature T_W will probably be sufficient. The water temperature will be derived by MODIS itself, while the source of the air-sea temperature difference will be the output of numerical weather models, probably from NMC.

3.1.1.7.6 Relative Humidity RH

The surface relative humidity (RH) is not really needed by the algorithm; however, it could be useful as a constraint on the candidate aerosol models chosen by the algorithm as described in Section 3.1.1.3. The error in the value of RH should be $< \pm 5 - 10\%$ to be useful. The source of this data set will be the output of numerical weather models, probably from NMC.

3.1.1.8 Examination of Approximations

3.1.1.8.1 Aerosol Vertical Structure

The reflectance of the atmosphere in the single-scattering approximation is independent of the manner in which the aerosol is distributed with altitude. However, this independence does not extend to a multiple-scattering atmosphere. As the multiple-scattering algorithm assumes that the

aerosol is all located in the bottom layer of a two-layer atmosphere, it is important to understand the

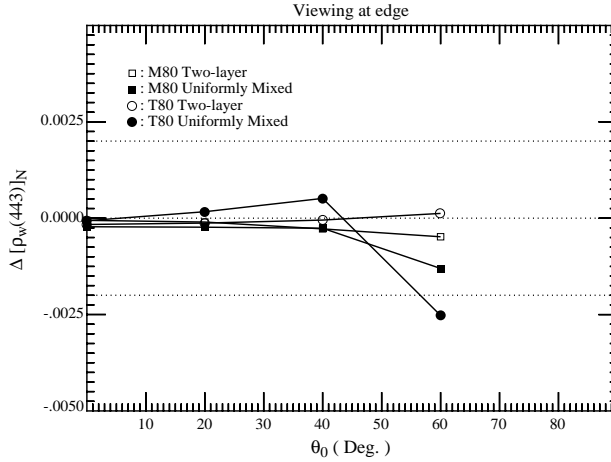


Figure 16a. Effect of the vertical distribution of aerosol on $\Delta[\rho_w(443)]_N$ as a function of θ_0 at the edge of the scan for the T80 and M80 aerosol models with $\tau_a(865) = 0.2$. Note that the correction algorithm assumes that the “Two-layer” stratification is correct.

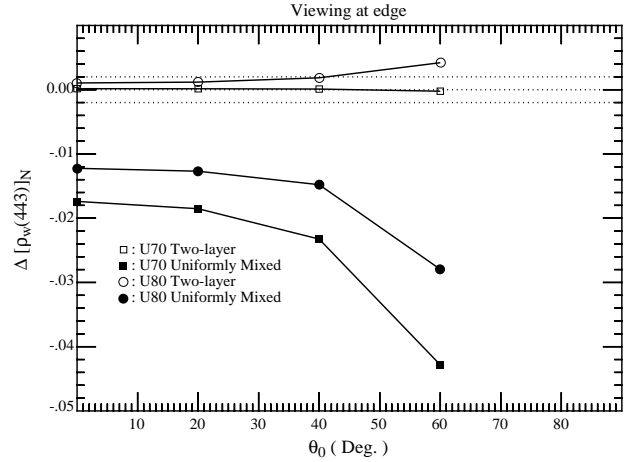


Figure 16b. Effect of the vertical distribution of aerosol on $\Delta[\rho_w(443)]_N$ as a function of θ_0 at the edge of the scan for the U80 and U70 aerosol models with $\tau_a(865) = 0.2$. Note that the correction algorithm assumes that the “Two-layer” stratification is correct.

effect of aerosol vertical structure on the correction algorithm. This has been studied by comparing the error in the algorithm when the pseudo data are simulated using the “correct” two-layer model with the error when the pseudo data are simulated using a model in which the aerosol and Rayleigh scattering have an altitude-independent mixing ratio, i.e., a uniformly mixed model. Figure 16a provides such a comparison for the M80 and T80 aerosol models with $\tau_a(865) = 0.2$. It is seen that the effect of an incorrect assumption regarding the vertical structure will not lead to serious errors in this case. However, in the case of strongly absorbing aerosols, e.g., the Urban models, the assumed vertical structure is very important. Figure 16b provides the two-layer versus uniformly mixed cases for the Urban models with $\tau_a(865) = 0.2$. In this case the candidate aerosol models were restricted to U50, U70, U90, and U99, as in the results for Figure 12. For the U80 case, the error becomes excessive, increasing by over an order of magnitude compared to the two-layer case. More disturbing is the performance of the U70 aerosol model. U70 is actually one of the candidate aerosol models in this case. When the vertical structure is the same as assumed by the algorithm, the error is negligible. In contrast, when the incorrect structure is assumed, the error becomes very large.

As we have examined only an extreme deviation from that assumed by the correction algorithm, it is of interest to quantify how the correction algorithm performs as the aerosol layer thickens from

being confined just near the surface to being mixed higher in the atmosphere. Thus, the top-of-atmosphere reflectance was simulated using a two layer model with aerosol *plus* Rayleigh scattering in the lower layer and *only* Rayleigh scattering in the upper layer. The fraction of the Rayleigh scattering optical thickness assigned to the lower layer was consistent with aerosol-layer thickness of 0, 1 km, 2 km, 4 km, 6 km, and ∞ . The aerosol model used in the simulations was U80, and $\tau_a(865)$ was kept constant at 0.2. The multiple-scattering algorithm was then operated with this pseudo data using U50, U70, U90, and U99 as candidate models. The results of this exercise are provided in Figure 17. Clearly, progressive thickening of the layer in which the aerosol resides leads to a progressive increase in the error in the retrieved water-leaving reflectance.

This influence of vertical structure on the algorithm when the aerosol is strongly absorbing is easy to understand. The algorithm assumes all of the aerosol resides in a thin layer beneath the molecular scattering layer. As the aerosol layer thickens and encompasses more and more of the molecular scattering layer, the amount of Rayleigh scattering within the aerosol layer will increase causing an increase in the average path length of photons through the layer, and a concomitant increase in absorption. Thus, for a given τ_a , ρ_t will decrease as the thickness of the aerosol layer increases. Since $\rho_r \sim \lambda^{-4}$, this decrease will be relatively more in the visible than in the NIR, so the algorithm will predict values of $\rho_a + \rho_{ra}$ in the visible that are too large, yielding an over correction, $\Delta[\rho_w(443)]_N < 0$.

Ding and Gordon [1995] (Figures 9 and 10) have provided some examples of the error in the multiple-scattering algorithm for vertical structures in which the aerosol model as well as concentration varies with altitude. For the weakly-absorbing aerosol of the models that they investigated ($\omega_a \gtrsim 0.93$), the conclusions are similar to those here: as long as the aerosol is weakly absorbing, the error is negligible, but as ω_a decreases, the error becomes progressively larger. Clearly, more study is required for a quantitative assessment of the impact of vertical structure in a strongly absorbing atmosphere; however, the computations provided here demonstrate that a large error in the vertical structure of the aerosol layer assumed for the lookup tables will result in a very poor atmospheric correction, even if the candidate aerosol models are appropriate. Figure 17 suggests that at a minimum, the lookup tables for the Urban candidates need to be recalculated under the assumption of an aerosol layer of finite physical thickness, i.e., some Rayleigh scattering in the aerosol layer. It also suggests that, for the case studied, if the lookup tables were computed for an aerosol layer of physical thickness 2 km, they would provide reasonable retrievals for layers with

thicknesses from 1 to 3 km, i.e., the algorithm could tolerate a ± 1 km error in the layer thickness for this case.

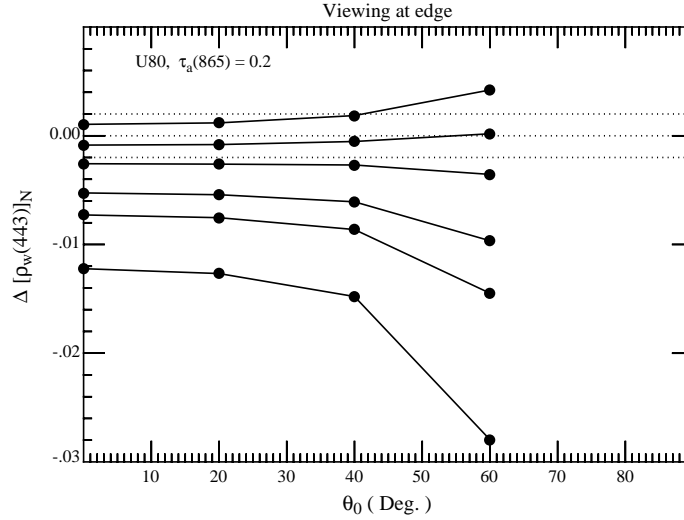


Figure 17. Effect of the vertical distribution of aerosol on $\Delta[\rho_w(443)]_N$ as a function of θ_0 at the edge of the scan for the U80 aerosol models with $\tau_a(865) = 0.2$. Curves from top to bottom refer to situations in which the aerosol is confined to a layer just above the surface, between the surface and 1, 2, 4, and 6 km, and uniformly mixed throughout the atmosphere.

3.1.1.8.2 Earth-Atmosphere Curvature Effects

All atmospheric corrections algorithms developed thus far ignore the curvature of the earth, i.e., the plane-parallel atmosphere approximation has been used in the radiative transfer simulations. However, at the level of accuracy required to utilize the full sensitivity of MODIS, it may be necessary to take the curvature of the earth into account, especially at high latitudes with their associated large θ_0 values. *Ding and Gordon* [1994] have examined this problem in detail using a model based on a spherical shell atmosphere solved with Monte Carlo techniques. It was found that as long as ρ_r was computed using a spherical shell atmosphere model, the multiple-scattering algorithm performed as well at high latitudes as at low latitudes. They provided a method for the rapid computation of ρ_r for the spherical shell atmosphere; however, it has yet to be implemented for image processing.

3.1.1.8.3 Polarization

All of the radiative transfer simulations described in Section 3.1.1 were carried out using scalar radiative transfer theory, i.e., polarization was ignored. In the case of single scattering, except for the terms involving the Fresnel reflectance, scalar (ignores polarization) and vector (includes polarization) radiative transfer theory lead to the same radiances. Thus, the single scattering algorithm is little influenced by polarization. It is well known, however, that, when multiple scattering is present, the use of scalar theory leads to small errors (\sim few %) in the radiance compared to that computed using exact vector theory [Gordon, Brown and Evans, 1988; Kattawar, Plass and Hitzfelder, 1976]. As with CZCS, in the actual application of the algorithm, ρ_r will be computed using vector theory; however, the lookup tables relating $\rho_a + \rho_{ra}$ to ρ_{as} have been computed using scalar theory. To understand the influence of neglecting polarization in the computation of the lookup tables, simulations of the top-of-the-atmosphere reflectance ρ_t were carried out using both scalar and vector radiative transfer theory. In the case of the scalar simulations, $[\rho_w(443)]_N$ was retrieved as described in Section 3.1.1.3. An identical retrieval procedure was used for the vector simulations with a single exception: as in the case of CZCS, ρ_r was computed using vector theory. The results are presented in Figure 18a and 18b for the M80 and T80 aerosol models respectively. These figures provide $\Delta\rho \equiv t\Delta\rho_w(443)$ (rather than $\Delta[\rho_w(443)]_N$ in the previous figures) produced by the multiple-scattering correction algorithm as a function of θ_0 for $\tau_a(865) = 0.2$. The notation “S–S” and “V–V” means that *both* ρ_t and ρ_r were computed using scalar (S–S) and vector (V–V) radiative transfer theory, respectively. Note that the difference between computations is the error induced by ignoring polarization in the preparation of the $\rho_a + \rho_{ra}$ versus ρ_{as} lookup tables. At present, only a small number of simulations of the type shown in Figure 18 have been carried out; however, for these the difference between S–S and V–V was typically $\lesssim 0.001$ but reached as much as 0.002 in isolated cases. Thus, compared to the errors possible when strongly absorbing aerosols or whitecaps are present, this error appears negligible. It could be removed by recomputing the lookup tables using vector radiative transfer theory, but at considerable computational cost.

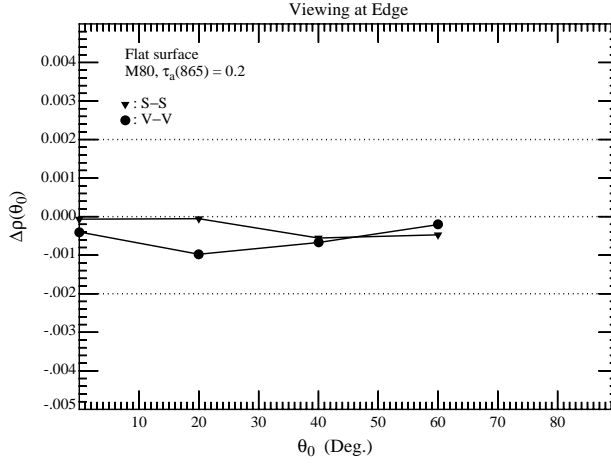


Figure 18a. Effect of neglecting polarization in the multiple-scattering lookup tables. S-S and V-V are for ρ_t and ρ_r computed using scalar and vector radiative transfer theory, respectively. $\Delta\rho \equiv t\Delta\rho_w$, the aerosol model is M80, and $\tau_a(865) = 0.2$.

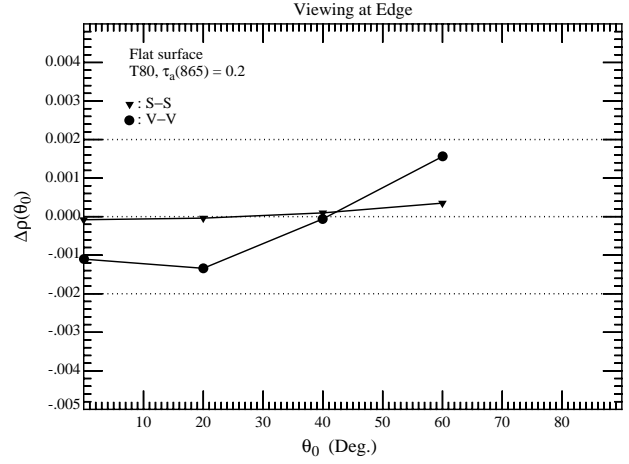


Figure 18b. Effect of neglecting polarization in the multiple-scattering lookup tables. S-S and V-V are for ρ_t and ρ_r computed using scalar and vector radiative transfer theory, respectively. $\Delta\rho \equiv t\Delta\rho_w$, the aerosol model is T80, and $\tau_a(865) = 0.2$.

3.1.1.8.4 Sea surface roughness

The roughness of the sea surface caused by the wind can play a large role on the reflectance measured at the top of the atmosphere. The principal effect of the rough surface is to redirect the direct solar beam reflected from the sea surface into a range of angles. This leads to a very large reflectance close to the specular image of the sun, known as sun glitter or the sun's glitter pattern. As this can be many times the radiance exiting the atmosphere in the smooth-surface case, the data in the region of the sun glitter must be discarded. This is accomplished by a mask as described in Appendix A. The remainder of the rough-surface effect is due to a redistribution of light scattered from the reflected solar beam (because it is redirected) and a redistribution of sky light reflected from the surface (the Fresnel reflection terms in Eq. (9)). This redistribution of radiance contaminates the imagery over all viewing angles. As the lookup tables relating $\rho_a + \rho_{ra}$ to ρ_{as} were computed under the assumption that the surface was flat, it is necessary to examine the error in the water-leaving reflectance induced when viewing a rough ocean. This was effected by computing ρ_t for an ocean roughened by the wind and inserting the result into the multiple-scattering correction algorithm. In this simulation, the sea surface roughness was based on the *Cox and Munk* [1954] surface slope distribution function (Appendix A). For computational simplicity, an omnidirectional wind was assumed [*Cox and Munk*, 1954]. The wind speed was taken to be

~ 7.5 m/s. Since *Gordon and Wang* [1992b] and *Gordon and Wang* [1992a] showed that at the

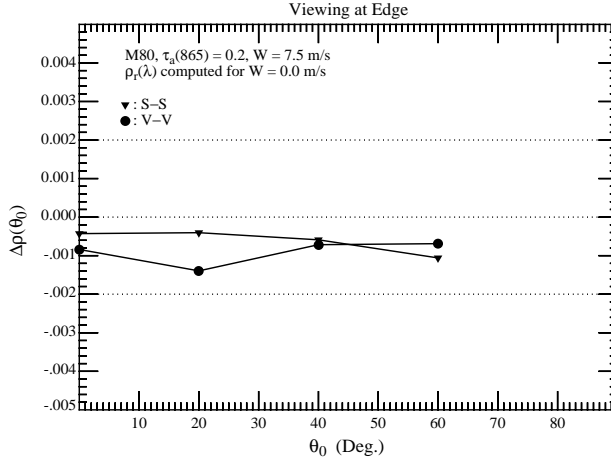


Figure 19a. Effect of neglecting sea surface roughness in the multiple-scattering lookup tables. S-S and V-V are for ρ_t and ρ_r computed using scalar and vector radiative transfer theory, respectively. $\Delta\rho \equiv t\Delta\rho_w$, the aerosol model is M80, and $\tau_a(865) = 0.2$. ρ_r has been computed assuming that $W = 0.0$ m/s.

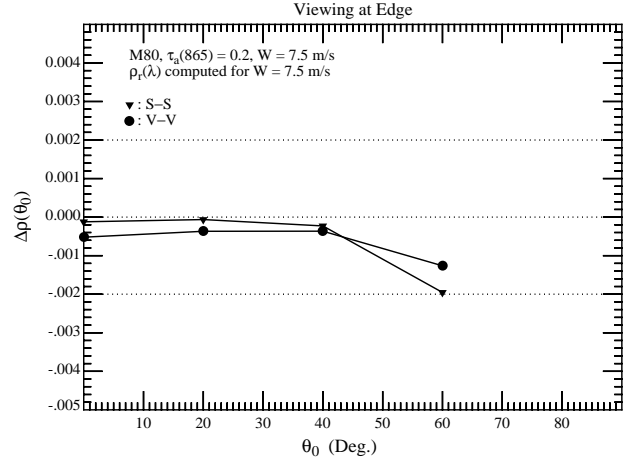


Figure 19b. Effect of neglecting sea surface roughness in the multiple-scattering lookup tables. S-S and V-V are for ρ_t and ρ_r computed using scalar and vector radiative transfer theory, respectively. $\Delta\rho \equiv t\Delta\rho_w$, the aerosol model is M80, and $\tau_a(865) = 0.2$. ρ_r has been computed assuming that $W = 7.5$ m/s.

radiometric sensitivity of SeaWiFS and MODIS, correct computation of the influence of surface roughness on ρ_r required use of vector radiative transfer theory, the computations were carried out using *both* scalar and vector theory. Sample results from one set of the small number of simulations that have been carried out to assess the effect of surface roughness are provided in Figure 19. These are in the same format as Figure 18. The differences between the two panels is that, in Figure 19a ρ_r has been computed assuming a smooth sea surface (a wind speed of zero), while in Figure 19b it has been computed using the correct (7.5 m/s) wind speed. For reference, Figure 18a provides similar results for a smooth sea surface. Comparing Figures 18a and 19a shows that the residual effect of the rough surface external to the sun's glitter pattern is small ($\Delta\rho \sim 0.0005$), and comparing Figures 18a and 19b shows that the residual effect can be removed by using the correct wind speed in the computation of ρ_r , i.e., ignoring the surface roughness in computation of the lookup tables relating $\rho_a + \rho_{ra}$ to ρ_{as} does not appear to lead to significant error.

3.1.1.8.5 Out-of-band Response

In the development of the algorithm, it has been assumed that the MODIS spectral bands were monochromatic, i.e., the reflectance ρ_t is measured at discrete wavelengths. However, the MODIS bands actually average the reflectance over spectral regions that are nominally 10–15 nm wide.

Also, the possibility exists that there could be significant out-of-band response, i.e., contributions to the reflectance from spectral regions far from the band center. This problem was particularly severe in the case of the SeaWiFS band at 865 nm [Barnes *et al.*, 1994], for which $\sim 9\%$ of the power measured in this band when observing a Rayleigh-scattering source originates at wavelengths shorter than 600 nm. Gordon [1995] has developed a methodology for delineating the influence of finite spectral band widths and significant out-of-band response of sensors for remote sensing of ocean color. The basis of the method is the application of the sensor's spectral response functions to the individual components of the TOA radiance rather than the TOA radiance itself. For engineering purposes, this approach allows one to assess easily (and quantitatively) the potential of a particular sensor design for meeting the system — sensor plus algorithms — performance requirements. Incorporation of this methodology into the atmospheric correction algorithm is relatively straightforward, and is being carried out for SeaWiFS. It can be easily added to the MODIS algorithm should characterization of the sensor show significant out-of-band response.

3.1.1.9 Remaining Issues

Although the algorithm described above is being implemented for the MODIS processing system, its performance is still under study. In addition, there are other questions and issues that are being studied for SeaWiFS and MODIS. These are outlined in the present section.

3.1.1.9.1 Stratospheric Aerosols

In some situations, e.g., following volcanic eruptions or when there are thin cirrus clouds present, there can be significant quantities of aerosol in the stratosphere. Gordon and Castaño [1988] showed that the presence of the El Chichón aerosol [King, Harshvardhan and Arking, 1984] had little effect on CZCS atmospheric correction; however, at the higher correction accuracy required for MODIS the Gordon and Wang [1994b] algorithm may be degraded by the presence of stratospheric aerosol. Although not listed in Table 1, MODIS is equipped with a spectral band at 1380 nm that can be used to assess the contamination of the imagery by stratospheric aerosol. This spectral band is centered on a strong water vapor absorption band and photons penetrating through the stratosphere will usually be absorbed by water vapor in the free troposphere [Gao, Goetz and Wiscombe, 1993]. Thus, any radiance measured at $1.38\ \mu\text{m}$ can, in the first approximation, be assumed to be scattered by the stratospheric aerosol alone, providing a mechanism for estimating the stratospheric contribution.

The author and coworkers [Gordon *et al.*, 1996] have assessed the effect of stratospheric aerosols on atmospheric correction and studied ways in which to correct the contamination, assuming that all radiance detected at 1380 nm results from scattering by the stratospheric aerosol *alone*. Briefly, the stratospheric aerosol contributes to the reflectance at all wavelengths. Thus, in its presence the total reflectance will be changed by an amount $\delta\rho_t^{(s)}$, i.e.,

$$\rho_t^{(s)}(\lambda) = \rho_t(\lambda) + \delta\rho_t^{(s)}(\lambda),$$

where $\rho_t^{(s)}$ is the reflectance of the entire ocean-atmosphere system in the presence of stratospheric aerosol, and ρ_t the reflectance in its absence. To assess the impact of the stratospheric aerosol, the multiple-scattering algorithm was operated using simulated values of $\rho_t^{(s)}(\lambda)$ in the place of $\rho_t(\lambda)$, for four stratospheric aerosol types. The results suggest that stratospheric aerosol/cirrus cloud contamination does not seriously degrade the Gordon and Wang [1994b] algorithm except for large ($\sim 60^\circ$) solar zenith angles and large ($\sim 45^\circ$) viewing angles, for which multiple scattering effects can be expected to be particularly severe.

The performance of a hierarchy of algorithms for using the 1380 nm MODIS band to correct for stratospheric aerosol/cirrus clouds, was also examined. The approach was to use $\rho_t^{(s)}(1380)$ to estimate $\delta\rho_t^{(s)}(\lambda)$ in the visible and NIR. The procedures investigated ranged from simply subtracting the reflectance at 1380 nm from that in the visible bands, i.e., $\delta\rho_t^{(s)}(\lambda) = \rho_t^{(s)}(1380)$, to assuming all of the optical properties of the stratospheric aerosol are known (measurement at 1380 nm providing the concentration) and carrying out multiple scattering computations to estimate $\delta\rho_t^{(s)}(\lambda)$. It is not surprising that the most complex procedures yield the best results; however, it was surprising that the complex procedures appear to only reduce the error in the retrieved water-leaving radiance by \lesssim a factor of two compared to the simplest procedures.

In the case of thin cirrus clouds, Gordon *et al.* [1996] investigated an empirical correction approach in which a detailed model of the cloud optical properties was not required. This correction proved to be satisfactory for cloud optical thicknesses as large as 0.5 with only a coarse estimate of the cloud scattering phase function; however, the correction requires some knowledge regarding the aerosol in the marine boundary layer and, therefore, requires two passes through the aerosol correction algorithm. Strategies for implementation of this algorithm are presently under study.

3.1.1.9.2 Appropriateness of aerosol models

Operation of the multiple-scattering algorithm requires a set of candidate aerosol models. Thus far, models from, or derived from, the work of *Shettle and Fenn* [1979] have been used as candidates. These models were basically developed from the analysis of aerosol physical-chemical properties and are believed to provide realistic approximations to the extinction and absorption cross section of real aerosols. However, they have never been validated for the role they are being used for here, i.e., for their ability to provide realistic aerosol phase functions and their spectral variation. As it is important to utilize as candidates, aerosol models that closely approximate the optical properties of actual aerosols over the ocean, work is being carried out or planned to study the optical properties of aerosols over the ocean.

Measurements over and above aerosol optical thickness and its spectral variation are required to understand the adequacy of candidate aerosol models. *Schwindling* [1995] compared estimates of the aerosol scattering phase function obtained from a pier at Scripps Institution of Oceanography at La Jolla, CA, with the properties of the *Shettle and Fenn* [1979] models and concluded that within the accuracy of their measurements the models fit both the phase function and the spectral variation of the aerosol optical thickness. It was also confirmed that $\tau_a(\lambda)$ becomes very low off the coast of CA. Such measurements need to be carried out in different regions and at different times. The AERONET aerosol monitoring network based on CIMEL sun/sky radiometers operated by B. Holben [*Holben et al.*, 1996] of NASA/GSFC is presently being expanded to include stations at the coast and on small islands. The plan is to use the methods developed by *Wang and Gordon* [1993] to invert the sky radiance and optical thickness data to obtain the aerosol scattering phase function and the single scattering albedo.

3.1.1.9.3 Strongly Absorbing Aerosols

In Section 3.1.1.4 it was shown that in the presence of strongly absorbing aerosols, the candidate aerosol models must be restricted to those with values of ω_a similar to the true aerosol. This was effected there by limiting the candidate models to U50, U70, U90, and U99 when the test aerosol was U80 (Figure 12), since when the initial twelve candidate models were used, the error was excessive (Figure 11). Without a method of determining the absorption characteristics of the aerosols from satellite measurements, an aerosol climatology is required to be able to provide realistic candidate models. Furthermore, in Section 3.1.1.8.1 it was shown that, for strongly absorbing aerosols, even given the appropriate set of candidate models, knowledge of the vertical distribution of the aerosol

was required for an adequate correction (Figure 17). Thus the aerosol climatology needs to contain information concerning the aerosol-layer thickness for regions with strongly absorbing aerosols.

The effort toward building a climatology for absorbing aerosols involves measurements of the type discussed in Subsection 3.1.1.9.2, i.e., measurements of sky radiance and aerosol optical thickness from ships or small islands in the appropriate regions. The *Wang and Gordon* [1993] retrieval algorithm should perform as well for strongly-absorbing as for nonabsorbing aerosols. A climatology for the aerosol vertical distribution can most effectively be built using LIDAR measurements [*Sasano and Browell*, 1989]. An excellent start toward a vertical distribution climatology can be made utilizing data from the Lidar In-Space Technology Experiment (LITE) [*McCormick*, 1995]. On the basis of LITE-based and aircraft-based measurements *Grant et al.* [1995] observed that the Saharan dust layer over the Eastern Caribbean extended in altitude from 1-4 km. This is in contrast to the dust-free atmosphere in which the thickness of the marine boundary layer is typically 1-2 km. We plan to use micro pulse lidar [*Spinhirne*, 1993] to study the vertical distribution in this region. Examining a LITE pass from Wallops Island, Virginia to Bermuda, *Ismail et al.* [1995] found that the plume of pollution from the U.S. East Coast was in a 1-2 km thick layer above the 0.5-1.0 km thick maritime boundary layer. These observations suggest that the principal absorbing aerosols expected in the Atlantic are mixed higher in the atmosphere than assumed in the existing candidate aerosol model lookup tables.

It must be pointed out that, with the exception of TOMS [*Herman et al.*, 1996], there is no space-borne way of discriminating between weakly- and strongly-absorbing aerosols. Clearly, it would be extremely useful to be able to detect the presence of absorbing aerosols from measurements made by the ocean color sensor alone, e.g., to be able to distinguish between absorbing and nonabsorbing aerosols. Computations using Mie scattering suggest that MODIS observations of $\rho_t(\lambda)$ for $\lambda > 865$ nm, may be useful in this regard. Figure 20 compares the $\varepsilon(\lambda, 865)$ for Haze C distributions of nonabsorbing (liquid water) and absorbing (minerals transported over the oceans with the index of refraction taken from *d'Almeida, Koepke and Shettle* [1991]) aerosol particles. Also included on Figure 20 are computations for a log-normal distribution suggested in *d'Almeida, Koepke and Shettle* [1991] for minerals transported over large distances to the marine environment. In contrast to nonabsorbing aerosols, the mineral aerosol shows a significant decrease in $\varepsilon(\lambda, 865)$ for $\lambda > 1.26 \mu\text{m}$ over that extrapolated from the observed $\varepsilon(765, 865)$ and $\varepsilon(1260, 865)$. This behavior of $\varepsilon(\lambda, 865)$ is apparently due to the rapid decrease in the real part of the mineral refractive index

beyond 1260 nm. Notwithstanding the perils of using Mie theory to predict the large-angle scattering for irregularly shaped particles [Mishchenko and Travis, 1994; Mugnai and Wiscombe, 1989] these computations suggest that it may be reasonable to try to use the short-wave infrared (SWIR) bands on MODIS to differentiate between some types of absorbing and nonabsorbing aerosols.

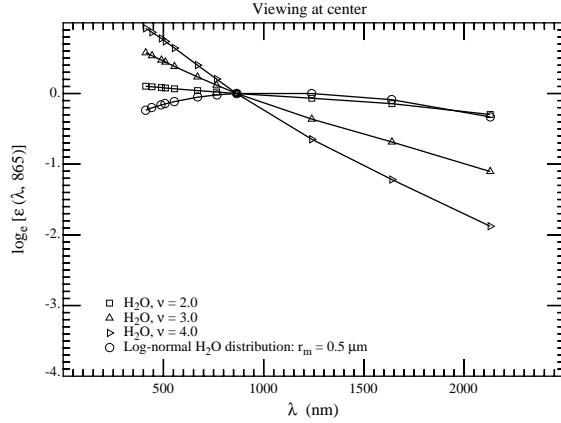


Figure 20a. $\varepsilon(\lambda, 865)$ for nadir viewing with $\theta_0 = 60^\circ$ for the Haze C models composed of liquid water.

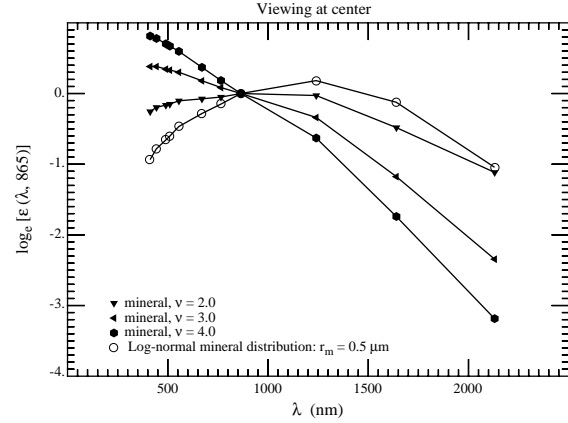


Figure 20b. $\varepsilon(\lambda, 865)$ for nadir viewing with $\theta_0 = 60^\circ$ for the Haze C models composed of absorbing minerals.

Although such a method would likely be limited to Saharan dust (assuming the modeled index of refraction is correct), we have performed simulations aimed at determining whether the single scattering approximation could be used to implement a discrimination algorithm based on this idea in a simple manner. If we ignore multiple scattering in the aerosol contribution, then ε is approximated by

$$\varepsilon_{\text{Approx}}(\lambda, 865) = \frac{\rho_t(\lambda) - \rho_r(\lambda)}{\rho_t(865) - \rho_r(865)}, \quad (15)$$

where ρ_t is the total reflectance of the ocean-atmosphere system, and ρ_r is the contribution due to Rayleigh scattering. Figure 21 compares the value of $\varepsilon_{\text{Approx}}(\lambda, 865)$ (for $\lambda = 765, 1240, 1640$, and 2130 nm) using this equation with the true value for the Log-normal (largest $\tau_a(\lambda)$ in the SWIR) model in Figure 20 and for aerosol optical thicknesses $\tau_a(865)$ of 0.3 and 0.4. Clearly, Eq. (15) provides an excellent approximation to $\varepsilon(\lambda, 865)$ in the NIR and SWIR for even large aerosol optical thicknesses. Thus, it appears that the SWIR could be used in a simple manner to distinguish Saharan dust from nonabsorbing maritime aerosols by extrapolating and $\varepsilon_{\text{Approx}}(865, 865)$ and $\varepsilon_{\text{Approx}}(1260, 865)$ to find $\varepsilon_{\text{Extrapolated}}(2130, 865)$. If $\varepsilon_{\text{Extrapolated}}(2130, 865) \gtrsim 2\varepsilon_{\text{Approx}}(2130, 865)$, it would indicate the presence of Saharan dust.

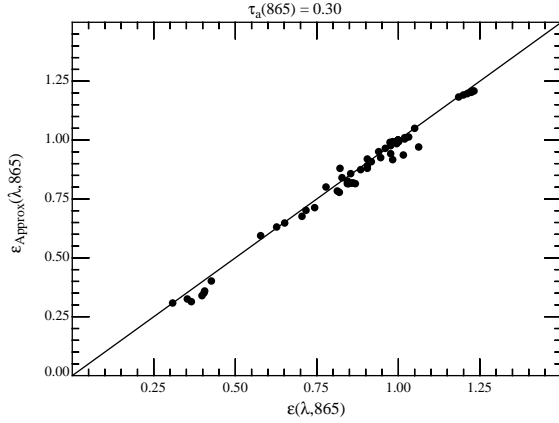


Figure 21a. Comparison between $\varepsilon(\lambda, 865)$ and $\varepsilon_{Approx}(\lambda, 865)$ for several viewing geometries with $\tau_a = 0.30$.

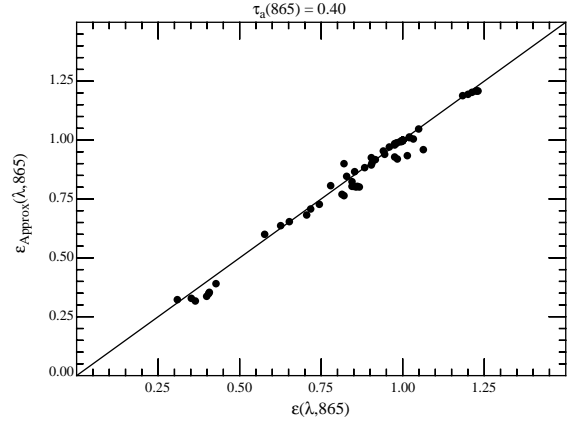


Figure 21b. Comparison between $\varepsilon(\lambda, 865)$ and $\varepsilon_{Approx}(\lambda, 865)$ for several viewing geometries with $\tau_a = 0.40$.

Do the relevant MODIS bands have sufficient sensitivity to allow the use of these bands for this purpose? The specifications of the MODIS SWIR bands are provided in Table 7 in terms of reflectance for a solar zenith angle of 60° . In the table, $\Delta\rho_{Dig}$ represents the quantization interval of the 12-bit digitized reflectance. Bands 4, 5, and 6 have a spatial resolution of 500 m compared to 1000 m for Bands 8-16 and 26. Comparing $NE\Delta\rho$ and $\Delta\rho_{Dig}$ suggests that averaging four 500 m pixels to form one 1000 m pixel could reduce the effective $NE\Delta\rho$ by \sim a factor of 2, particularly for Band 5.

To estimate the aerosol component of the expected reflectance in these bands, we take a conservative approach. We assume a mineral aerosol (strongly absorbing) with $\tau_a(865) = 0.2$ and use the single scattering approximation with the surface reflection terms omitted. Then for nadir viewing and $\theta_0 = 60^\circ$,

$$\rho_{as}(\lambda) = \frac{\omega_a(\lambda)P_a(120^\circ, \lambda)\tau_a(\lambda)}{2}.$$

For the size distribution we use the Haze C model with $\nu = 2$ (the smallest $P_a(120^\circ)$) as well as the log-normal model (Figure 20). The resulting values of ρ_{as} are presented in Table 8.

These computations suggest that Bands 5 and 6 would be able to detect aerosols with a signal-to-noise ratio of ~ 20 , with pixel averaging. In contrast, it appears that Band 7 would be useful only at higher $\tau_a(865)$. One must note, however, that these estimates for ρ_{as} are conservative. This approach to detecting mineral dust will be studied in a research mode after the launch of MODIS.

Table 7: Radiometric performance of MODIS in the SWIR

Band	λ (nm)	ρ_{max} (Sr^{-1})	$\text{NE}\Delta\rho$ (Sr^{-1})	$\Delta\rho_{\text{Dig}}$ (Sr^{-1})
5	1240	0.94	6.2×10^{-4}	2.2×10^{-4}
6	1640	1.88	7.2×10^{-4}	4.6×10^{-4}
7	2130	1.50	6.2×10^{-4}	3.6×10^{-4}
26	1380	1.64	7.2×10^{-4}	4.0×10^{-4}

Table 8: Expected aerosol reflectance in the SWIR.

Values for ρ_{as} and $\text{NE}\Delta\rho$ have been multiplied by 10^{+4} .

Band	λ (nm)	ρ_{as} (Sr^{-1})	$\text{NE}\Delta\rho$ (Sr^{-1})	
		Haze C	Log-normal	
16	865	110	103	0.8
5	1240	106	128	6.2
6	1640	68	94	7.2
7	2130	39	37	6.2

Finally, the fact that TOMS is capable of detecting the presence of strongly-absorbing aerosols [Herman *et al.*, 1996] provides an exciting possibility of using such data to aid in atmospheric correction. We shall investigate the possibility of employing TOMS data in the MODIS atmospheric correction algorithm. We note, however, that using this data on an operational basis may introduce a delay in the processing of MODIS data.

3.1.1.9.4 In-Water Radiance Distribution

Algorithms for retrieving total pigments, chlorophyll, etc., from ocean color imagery are developed by relating the nadir-viewing water-leaving radiance to the quantity in question. In the analysis of ocean color imagery it has always been assumed that $[\rho_w]_N$ is independent of the viewing angle. This assumption was based on a small number of observations, e.g., see Smith [1974] and references therein, which suggests that $L_u(z, \theta, \phi)$, the upwelling radiance at depth z beneath

the surface and traveling in a direction specified by the angles (θ, ϕ) , is only weakly dependent on θ and ϕ . However, in a series of papers Morel and Gentili [Morel and Gentili, 1991; Morel and Gentili, 1993; Morel and Gentili, 1996] studied theoretically the bidirectional effects as a function of the sun-viewing geometry and the pigment concentration. Their simulations suggest that, although the bidirectional effects nearly cancel in the estimation of the pigment concentration using radiance ratios (Eq. (4)), $L_u(z, \theta, \phi)$ can depend significantly on θ , ϕ and θ_0 . This means that the value of $[\rho_w]_N$ retrieved in atmospheric correction is actually appropriate only to the viewing direction in which the measurement of ρ_t is made. Since most in-water algorithms have been developed based on nadir-viewing measurements, the derived $[\rho_w]_N$ values should be corrected to nadir-viewing geometry. This requires understanding the bidirectional effects. This is effected by direct determination of the upwelling radiance distribution for a variety of waters and solar zenith angles using an electro-optics radiance camera system developed by Voss [1989], e.g., see Morel, Voss and Gentili [1995]. These measurements will provide direct determination of the effect, and will yield an algorithm for extrapolation to the nadir viewing direction as required for derived product algorithms.

3.1.1.9.5 Diffuse transmittance

The diffuse transmittance was mentioned in Section 3.1.1. It is defined as the water-leaving radiance in a particular viewing direction (θ_v, ϕ_v) “transmitted” to the top of the atmosphere, i.e.,

$$t(\theta_v, \phi_v) = \frac{\rho_w(\theta_v, \phi_v)_{\text{Top}}}{\rho_w(\theta_v, \phi_v)}.$$

Thus, if the atmosphere were only illuminated from below with radiance $\rho_w(\theta, \phi)$, the radiance measured at the top of the atmosphere in the direction (θ_v, ϕ_v) would be $t(\theta_v, \phi_v)\rho_w(\theta_v, \phi_v)$. The diffuse transmittance accounts for the direct loss from $\rho_w(\theta_v, \phi_v)$ due to absorption and scattering within the atmosphere, as well as for the gain in radiance in the direction (θ_v, ϕ_v) due to scattering of $\rho_w(\theta, \phi)$, i.e., from all other upward directions, into (θ_v, ϕ_v) . In the case of the CZCS, it was assumed that $\rho_w(\theta, \phi)$ is independent of (θ, ϕ) . Then, $t(\theta_v, \phi_v, \lambda)$ was approximated by [Gordon *et al.*, 1983]

$$t(\theta_v, \phi_v, \lambda) = \exp \left[- \left(\frac{\tau_r(\lambda)}{2} + \tau_{Oz}(\lambda) \right) \left(\frac{1}{\mu_v} \right) \right] t_a(\theta_v, \lambda), \quad (16)$$

where

$$t_a(\theta_v, \lambda) = \exp \left[- \frac{[1 - \omega_a(\lambda)F_a(\mu_v, \lambda)]\tau_a(\lambda)}{\mu_v} \right], \quad (17)$$

and $\mu_v = \cos \theta_v$. $F_a(\mu_v, \lambda)$ is related to the scattering phase function of the aerosol and is given by

$$F_a(\mu_v, \lambda) = \frac{1}{4\pi} \int_0^1 P_a(\alpha, \lambda) d\mu d\phi,$$

where $P_a(\alpha, \lambda)$ is the aerosol phase function at λ (normalized to 4π) for a scattering angle α , and

$$\cos \alpha = \mu\mu_v + \sqrt{(1 - \mu^2)(1 - \mu_v^2)} \cos \phi.$$

If θ_v is $\lesssim 60^\circ$ the factor $[1 - \omega_a(\lambda)F_a(\mu_v, \lambda)]$ is usually $\ll 1$, so t_a depends only weakly on the aerosol optical thickness and was taken to be unity for CZCS.

As retrieval of ρ_w from ρ_t requires t , and relative error in t will yield an equivalent relative error in ρ_w , it is important to compute this quantity as accurately as possible. Because the correction algorithm provides models of the aerosol, it is possible to incorporate all of the multiple scattering and aerosol effects into t in the form of look up tables, and considerably improve its accuracy. Unfortunately, any precomputed t must be based on an assumed form for the water-leaving radiance distribution. The natural distribution to assume is uniform (independent of direction); however, as described in Subsection 3.1.1.9.4, $L_u(\theta, \phi)$ just beneath the surface is not uniform, so this assumption cannot be correct. In fact, the appropriate transmittance to use to propagate the water-leaving reflectance to the top of the atmosphere depends on the actual variation of $L_u(\theta, \phi)$ with θ and ϕ . The extent of the effect of $L_u(\theta, \phi)$ on the transmittance is being studied [Yang and Gordon, in preparation], and preliminary results indicate that the difference between a uniform (subsurface) upwelling distribution and a more-realistic $L_u(\theta, \phi)$ is usually $< 5\%$ of t . This suggests that derivation of $\rho_w(443)$ within $\pm 5\%$ may require knowing, or estimating, the shape of the subsurface radiance distribution. Morel and Gentili [1996] have devised an iterative scheme for estimating the shape of the subsurface radiance distribution from an estimate of the pigment concentration. Such a scheme may be required to provide a more realistic value for t .

3.1.1.9.6 Residual Instrument Polarization

All scanning radiometers display some sensitivity to the polarization of the radiance they are intended to measure. For MODIS, it was specified that this polarization sensitivity should be less than 2%, and that it be mapped as part of the sensor characterization procedure. Depending on how well the MODIS meets this specification, a correction may be required to remove the residual polarization effects from ρ_t . We have developed a formalism [Gordon, 1988] which provides the

framework for removal of instrumental polarization-sensitivity effects. The difficulty with removing the polarization sensitivity error is that the polarization properties of the radiance backscattered by the aerosol are unknown. Although the details of the correction process have yet to be determined, simulations of this effect for an instrument possessing ~ 3 – 4 times the polarization sensitivity expected for MODIS are presently being carried out. Preliminary results suggest that the error caused by polarization sensitivity can be severe; however, elimination of the error is possible at the required level of accuracy by estimating the polarization of the top-of-atmosphere radiance to be that expected for a pure Rayleigh scattering atmosphere, given an accurate determination of the Mueller matrix for the instrument prior to launch.

3.1.1.9.7 Residual Sun Glitter

The algorithm implementation (Section 3.1.2) assumes that an appropriate sun glitter mask (Appendix A) has been applied to the imagery at a lower level of processing to remove seriously contaminated pixels. (If not, this would be the first step in the $[\rho_w]_N$ retrieval algorithm.) After application of the mask, the imagery will still contain some residual sun glitter unless the mask is extremely conservative. Although not in the processing stream as envisaged below, we shall experiment with SeaWiFS imagery to understand the efficacy of the *Cox and Munk* [1954] analysis for removal of the residual sun glitter, and design a correction module if appropriate. We note, however, that over and above the error in the Cox-Munk distribution, there will be additional error caused by variations in wind speed and direction on spatial scales that cannot be resolved by operational models. If removal does not appear possible, a very conservative sun glitter mask will be used.

3.1.2 Mathematical Description of the Algorithm

The multiple-scattering algorithm is implemented as described in Section 3.1.1.3, i.e., lookup tables providing $K[\lambda, \rho_{as}(\lambda)]$, in the form of $a(\lambda)$, $b(\lambda)$, and $c(\lambda)$ in Eq. (12), for all required viewing geometries, solar zenith angles, wavelengths, aerosol models, and aerosol concentrations, are used to provide the $\rho_t - \rho_r - t\rho_w$ versus ρ_{as} relationship. An annotated flow diagram for the entire algorithm is presented in Figure 22.

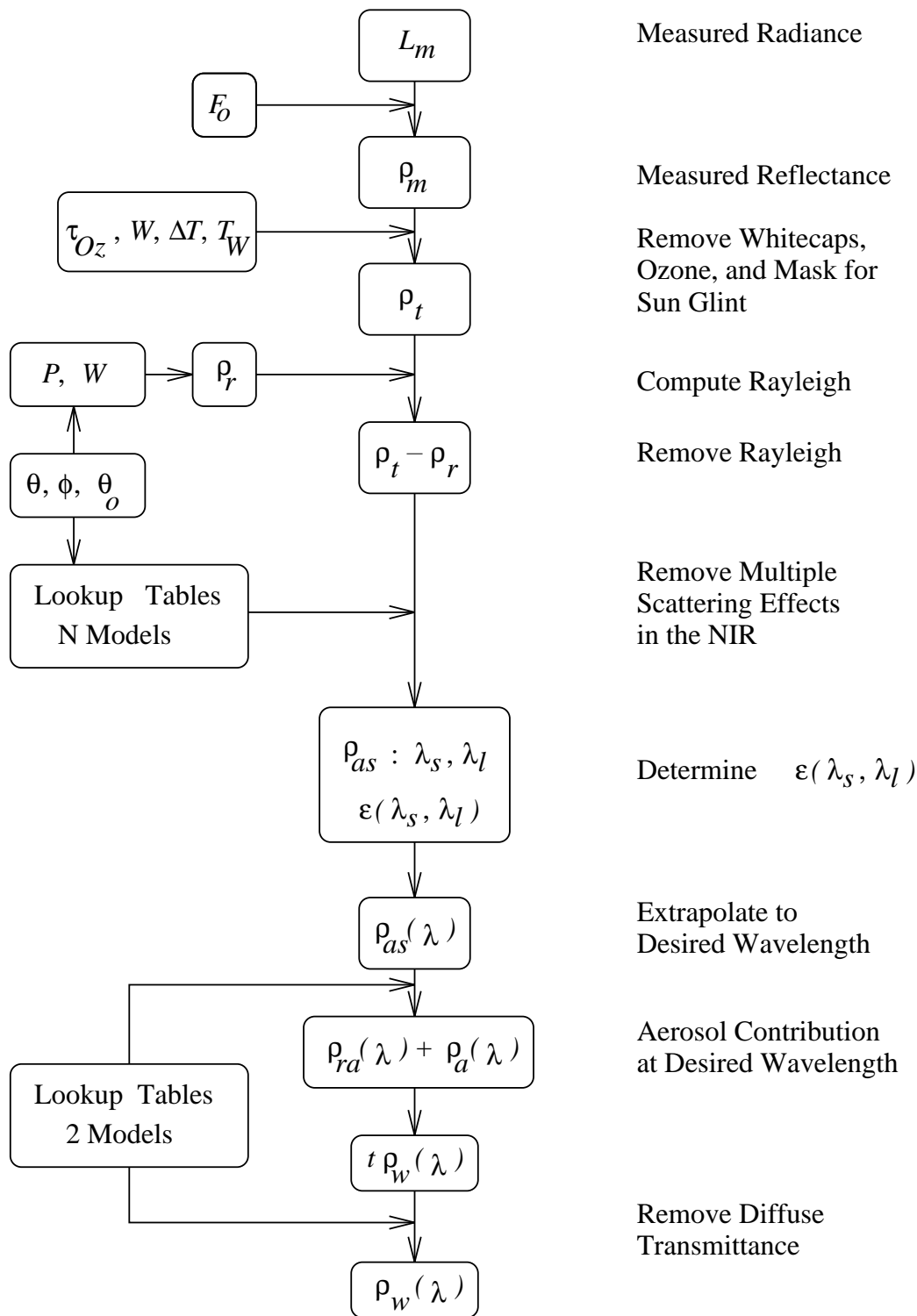


Figure 22. Annotated flow diagram of the algorithm.

3.1.3 Uncertainty Estimates

There are four major sources of error in the algorithm as described thus far. The first is the fact that the N candidate aerosol models chosen to describe the aerosol may be unrepresentative of the natural aerosol. The magnitude of this effect has been estimated in Section 3.1.1.4. (In particular see Figure 11.) The second is the error in the estimate of the whitecap reflectance ρ_{wc} . In Section 3.1.1.6 we showed that when the whitecap reflectance depends on wavelength as suggested by *Frouin, Schwindling and Deschamps* [1996], the error in $[\rho_w]_N$ is similar to the error in the estimate of $[\rho_{wc}]_N$, which exceeds ± 0.002 at 443 nm for a wind speed of ~ 9 –10 m/s. The third is the error associated with either the misidentification of strongly-absorbing aerosols as being weakly-absorbing, or in the case of strongly-absorbing aerosols, an inaccurate estimate of their vertical extent. The magnitude of these errors was discussed in Sections 3.1.1.4 and 3.1.1.8.1. The fourth is the error in the sensor's radiometric calibration, i.e., the error in $\rho_t(\lambda)$. In this section we will describe some simulations to estimate the magnitude of the effect of the radiometric calibration error.

Since the desired water-leaving reflectance is only a small part of ρ_t , at most $\sim 10 - 15\%$ (Table 1), accurate calibration of the sensor is critical [*Gordon, 1987*]. In this section we describe simulations to estimate the magnitude of the effect of the radiometric calibration error, and discuss how accurate on-orbit calibration can be effected.

To assess the effect of calibration errors, we add a small error to each of the measured reflectances, i.e.,

$$\rho'_t(\lambda) = \rho_t(\lambda)[1 + \alpha(\lambda)], \quad (18)$$

where $\alpha(\lambda)$ is the fractional error in $\rho_t(\lambda)$ and $\rho'_t(\lambda)$ is the value of $\rho_t(\lambda)$ that the incorrect sensor calibration would indicate. The atmospheric correction algorithm is then operated by inserting $\rho'_t(\lambda)$ as the measured value rather than the true value $\rho_t(\lambda)$ and $t\Delta\rho_w \equiv \Delta\rho$ is computed as before.

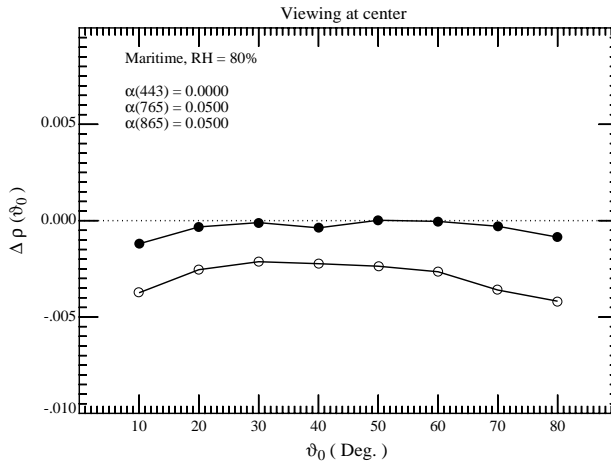


Figure 23a. Error in the retrieved $t(443)\rho_w(443)$ for viewing at the center of the scan with a Maritime aerosol at RH = 80% as a function of the solar zenith angle with $\tau_a(865) = 0.2$ and calibration errors $\alpha(443)$, $\alpha(765)$, and $\alpha(865)$ in Eq. (18) (open circles). Solid circles are for $\alpha(\lambda_i) = 0$ for all λ_i .

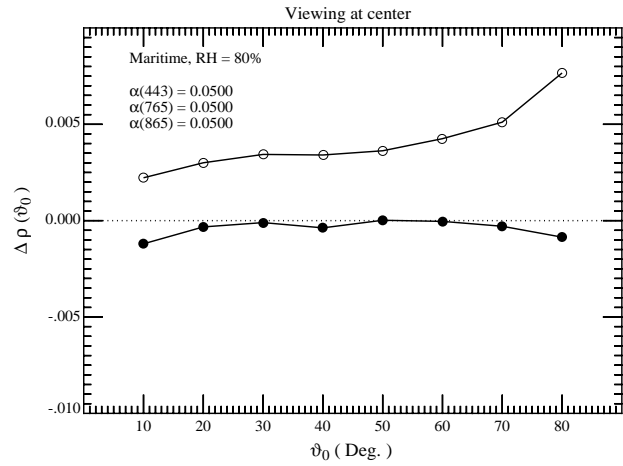


Figure 23b. Error in the retrieved $t(443)\rho_w(443)$ for viewing at the center of the scan with a Maritime aerosol at RH = 80% as a function of the solar zenith angle with $\tau_a(865) = 0.2$ and calibration errors $\alpha(443)$, $\alpha(765)$, and $\alpha(865)$ in Eq. (18) (open circles). Solid circles are for $\alpha(\lambda_i) = 0$ for all λ_i .

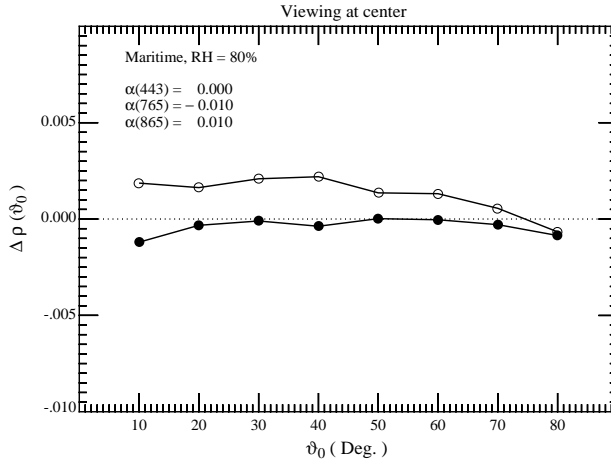


Figure 23c. Error in the retrieved $t(443)\rho_w(443)$ for viewing at the center of the scan with a Maritime aerosol at RH = 80% as a function of the solar zenith angle with $\tau_a(865) = 0.2$ and calibration errors $\alpha(443)$, $\alpha(765)$, and $\alpha(865)$ in Eq. (18) (open circles). Solid circles are for $\alpha(\lambda_i) = 0$ for all λ_i .

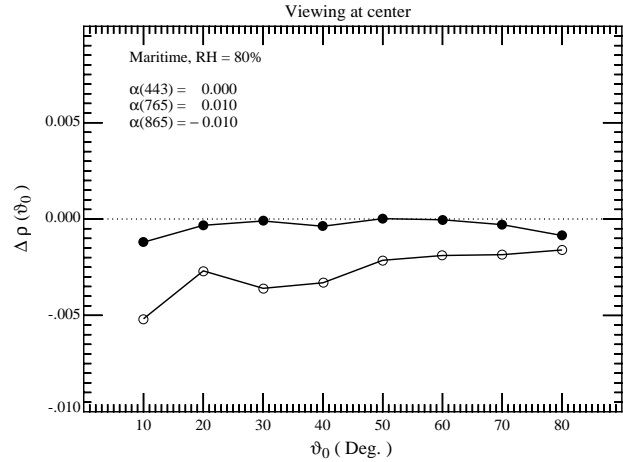


Figure 23d. Error in the retrieved $t(443)\rho_w(443)$ for viewing at the center of the scan with a Maritime aerosol at RH = 80% as a function of the solar zenith angle with $\tau_a(865) = 0.2$ and calibration errors $\alpha(443)$, $\alpha(765)$, and $\alpha(865)$ in Eq. (18) (open circles). Solid circles are for $\alpha(\lambda_i) = 0$ for all λ_i .

Assuming the single-scattering algorithm, Eq. (11), is exact, and $\varepsilon(\lambda_i, \lambda_l) = \exp[c(\lambda_l - \lambda_i)]$, it is easy to show that to first order in $\alpha(\lambda)$, the error in the retrieved ρ_w is

$$t(\lambda_i)\Delta\rho_w(\lambda_i) = \alpha(\lambda_i)\rho_t(\lambda_i) - \varepsilon(\lambda_i, \lambda_l)\alpha(\lambda_l)\rho_t(\lambda_l) - \left(\frac{\lambda_l - \lambda_i}{\lambda_l - \lambda_s}\right) \left[\frac{\varepsilon(\lambda_i, \lambda_l)}{\varepsilon(\lambda_s, \lambda_l)}\alpha(\lambda_s)\rho_t(\lambda_s) - \varepsilon(\lambda_i, \lambda_l)\alpha(\lambda_l)\rho_t(\lambda_l) \right] \quad (19)$$

The first term represents the direct effect of calibration error at λ_i on $\rho_w(\lambda_i)$, while the remaining terms represent the indirect effect from calibration error in the atmospheric correction bands at λ_s and λ_l . The second term obviously increases in importance as λ_i decreases. Note that if all of the spectral bands have calibration error with the same sign, i.e., all $\alpha(\lambda)$ have the same sign, significant cancelation of the atmospheric correction contribution can occur; however, if $\alpha(\lambda_s)$ and $\alpha(\lambda_l)$ have different signs, the error is magnified as the last two terms in Eq. (19) will add.

To see if this holds for the multiple-scattering algorithm as well, it was also operated by inserting $\rho'_t(\lambda)$ as the measured value rather than the true value $\rho_t(\lambda)$. The results of this exercise are presented in Figures 23a–23d for the M80 aerosol model at the center of the scan. In Figures 23a and 23b, $\alpha(765) = \alpha(865)$ with $\alpha(443) = 0$ (Figure 23a) or with $\alpha(443) = \alpha(765) = \alpha(865)$ (Figure 23b). Figures 23a and 23b show the effect of a calibration bias that is the same at 765 and 865 nm. Figures 23c and 23d show the effect of having calibration errors that are of opposite sign at 765 and 865 nm. Note that in this case even a small calibration error (1%) can make as significant an error in $\rho_w(443)$ as a large calibration error (5%) when the signs are all the same. As discussed above, the reason the error is so much larger when it is of opposite sign at 765 and 865 nm is that it will cause a large error in the estimated value of $\varepsilon(765, 865)$, and this will propagate through the algorithm causing a large error in the retrieved water-leaving reflectance at 443 nm. In the cases examined in Figure 23, the magnitude of the errors is in quantitative agreement with that predicted by Eq. (19).

As the goal for the calibration of the relevant ocean color bands on MODIS is that L_t have an uncertainty of $< \pm 5\%$, and Figures 23c and 23d show that such an error (even if it were the same in each band) would cause the error in the retrieved $\rho_w(443)$ to be outside the acceptable range. A method for overcoming these calibration difficulties is provided later in this ATBD.

3.2 Practical Considerations

In this section we intended to discuss the intricacies of actually using the algorithm by virtue of experience with SeaWiFS data. However, in its absence, we have utilized CZCS data as a preliminary test of the algorithm. This has been carried out through CZCS data through collaboration with R. Evans and J. Brown. Operating with SeaWiFS or MODIS data, the algorithm will use measured radiances near 765 and 865 nm (where the ocean is essentially a black body) to correct the radiances in the visible for atmospheric effects. CZCS has only half of the spectral bands of SeaWiFS and MODIS with no bands in the near infrared (NIR). Thus, there are no bands for which the ocean can be approximated as a black body. To test the implementation with CZCS data, we examined “clear” water imagery, e.g., the Sargasso Sea, for which the water-leaving radiance is known at three of the bands (520, 550, and 670 nm) [*Gordon and Clark*, 1981] and used the algorithm to derive the water-leaving radiance at 443 nm. The resulting water-leaving radiances were typically within one CZCS digital count of the radiances derived with the standard CZCS atmospheric correction algorithm. This suggests that the initial implementation software contains few coding errors; however, tests of the adequacy of the algorithm for retrieving the water-leaving radiance must await SeaWiFS data.

The CZCS test provided estimates for the minimum computational resources required to run the algorithm. The timing’s that were determined for a single processor are provided in Table 9. They refer to a CZCS image with about 50% clouds. Cloud pixels are not processed but they *are* counted in the total. The speed of the present algorithm is well above that required to keep up with the SeaWiFS data flow; however, it must be increased — either through increases in CPU speed or algorithm modifications — to keep up with the volume of MODIS data. Possible modifications are being considered; however, their effectiveness must await the availability of SeaWiFS data.

This implementation provides an example of our cooperative interaction with MODIS Science Team member R. Evans, who is designing the MODIS Ocean Computing Facility. When our original SeaWiFS implementation algorithm was delivered to Evans, it could only process CZCS imagery at the rate of *one* pixel per second. Evans and co-workers increased the speed by a factor of approximately 200.

Table 9: Speed (in pixels/s) of the implementation of the proposed SeaWiFS atmospheric correction algorithm

Computer	Frequency (MHz)	Rate (Pixels/s)
SGI 4D/480	40	181
SGI Indigo 2	150	509
DEC 3000/400	133	569
DEC 3000/500	176	679
DEC 7000/610	183	860

The present algorithm does not appear to be capable of adequately dealing with strongly-absorbing aerosols, e.g., the Urban model. Although urban aerosols are not expected to be prevalent over the oceans, desert aerosols blown over the oceans exhibit similar properties [Nakajima *et al.*, 1989], so aerosols of this type need to be addressed. This will require that a system be developed to indicate the presence of such aerosols — by unacceptable $[\rho_w]_N$'s, unacceptable pigments, etc. — and initiate a second pass through the algorithm using a special set of candidate aerosol models with the appropriate absorption properties.

It is too early to speculate on some portions of the individual subsections below and parts are occasionally marked “TBD” (To Be Determined). Please note that those that are not marked TBD are not necessarily complete.

3.2.1 Programming and Procedural Considerations

These considerations are described in the ATBD “Processing Framework and Matchup Data Base: MODIS Algorithm” by R. Evans. The report also includes data volume, networking, and CPU requirements.

3.2.2 Calibration, Initialization, and Validation

In Section 3.1.3 examples were provided to show the sensitivity of the algorithm to sensor calibration errors (Figure 23). It was demonstrated that calibration errors of the order of $\pm 5\%$, the absolute radiometric calibration uncertainty specified for the MODIS visible bands, would lead

to excessive error in $[\rho_w]_N$, even if the calibration error the errors in bands 15 and 16 were of the same sign. When errors in these bands are small ($\sim \pm 1\%$) but have opposite signs (Figures 23c and 23d), the error in the water-leaving reflectance becomes large because of the extrapolation of ε into the visible. Thus, it is clear the the calibration uncertainty of MODIS must be reduced in order to provide acceptable $[\rho_w]_N$, retrievals.

3.2.2.1 Calibration Initialization

Although the calibration requirement is difficult if not impossible to meet using standard laboratory methods, it should be possible to perform an adequate calibration in orbit using surface measurements to deduce the true water-leaving radiance and the optical properties of the aerosol. This is normally referred to as *vicarious* calibration [Evans and Gordon, 1994; Fraser and Kaufman, 1986; Gordon, 1987; Koepke, 1982; Slater et al., 1987]. Below, we outline a plan for effecting such calibration, the process of which we refer to as *initialization*. This calibration is *not* radiometric, rather, it is a calibration of the entire system — the sensor *plus* the algorithms. As will be seen below, the sensor calibration will be adjusted to force the algorithm to conform to surface measurements of water-leaving radiance and atmospheric (aerosol) properties. A similar procedure was carried out for CZCS [Evans and Gordon, 1994], but without surface-based atmospheric measurements. It was only moderately successful because the calibration of that instrument varied in time, and there was no independent way of determining the temporal variation. Here, we make the assumption that any change in the sensitivity of the instrument with time can be determined by other methods, e.g., using the SRCA, the solar diffuser, or imagery of the moon.

Upon initial operation of the sensor, one expects that the $\alpha(\lambda_i)$ in Eq. (18) will be of the order of $\pm 5\%$, with $\alpha(\lambda_i)$ being positive for some λ_i and negative for others. We examine imagery acquired over ships measuring $L_w(\lambda_i)$ for a variety of (clear sky) aerosol concentrations. Given $\rho_w(\lambda_i)$, and assuming the atmospheric correction algorithm is exact, we operate it backward and compute $\varepsilon(\lambda_i, \lambda_l)$ at each wavelength λ_i , and note the behavior of $\varepsilon(\lambda_i, \lambda_l)$ with λ_i . Figure 3 shows that $\varepsilon(\lambda_i, \lambda_l)$ is expected to be a smooth function of λ_i for all of the aerosol models. If the $\alpha(\lambda_i)$'s differ significantly in magnitude (or in sign), $\varepsilon(\lambda_i, \lambda_l)$ will vary with λ_i in a repeatable (from day-to-day) but unrealistic manner. We can understand how this works with the aid of a

hypothetical example. To keep the analysis simple, we assume that the single scattering version of the atmospheric correction algorithm is exact. In that case,

$$\rho_t(\lambda) = \rho_r(\lambda) + \rho_{as}(\lambda) + t(\lambda)\rho_w(\lambda),$$

and from its definition

$$\varepsilon(\lambda_i, \lambda_l) = \frac{\rho_{as}(\lambda_i)}{\rho_{as}(\lambda_l)} = \frac{\rho_t(\lambda_i) - \rho_r(\lambda_i) - t(\lambda_i)\rho_w(\lambda_i)}{\rho_t(\lambda_l) - \rho_r(\lambda_l) - t(\lambda_l)\rho_w(\lambda_l)}.$$

Inserting ρ'_t from Eq. (18) in place of ρ_t , we have

$$\varepsilon(\lambda_i, \lambda_l) = \frac{\alpha(\lambda_i)\rho_t(\lambda_i) + \rho_{as}(\lambda_i)}{\alpha(\lambda_l)\rho_t(\lambda_l) + \rho_{as}(\lambda_l)}. \quad (20)$$

For very small $\alpha(\lambda)$'s this provides an approximately correct $\varepsilon(\lambda_i, \lambda_l)$, i.e., $\rho_{as}(\lambda_i)/\rho_{as}(\lambda_l)$; however, if the $\alpha(\lambda_i)$'s are not small, very significant errors are possible. To illustrate this we consider two error scenarios: (1) the $\alpha(\lambda_i)$'s alternate in sign from band to band; and (2) the $\alpha(\lambda_i)$'s all have the same sign. In each case we assume for simplicity that they all have the same magnitude. The assumed viewing geometry is $\theta_0 \approx 32^\circ$, $\theta_v \approx 33^\circ$, and $\phi_v \approx 100^\circ$. The “aerosol radiance” L_a defined as $L_t - L_r - tL_w$ at 670 nm is taken to be 0.2, 0.4, and 0.6 mW/cm²μm sr. For reference, from CZCS imagery, the *mean* L_a for the Arabian Sea in winter is ~ 0.6 mW/cm²μm sr, with a standard deviation of about 0.2 mW/cm²μm sr (C.R. McClain, GSFC, personal communication). The results of computing $\varepsilon(\lambda_i, \lambda_l)$ with Eq. (20) as a function of the magnitude and the sign of the calibration error are provided in Figures 24a–24f. In preparing the figures it has been assumed that the correct value of $\varepsilon(\lambda_i, \lambda_l)$ is unity for all λ_i . This is what would be expected for a Maritime aerosol at high RH. The figures clearly show that the derived value of $\varepsilon(\lambda_i, \lambda_l)$ is strongly influenced by the calibration error, and the influence increases as $L_a(670)$ decreases. At this point the sensor calibration can be adjusted to yield a reasonable behavior for $\varepsilon(\lambda_i, \lambda_l)$.

If the true values of $\varepsilon(\lambda_i, \lambda_l)$ were known, the calibration could be adjusted to bring the apparent values into equality with the true values. In this case, Eq. (20) shows that the residual values of the $\alpha(\lambda_i)$'s are given by

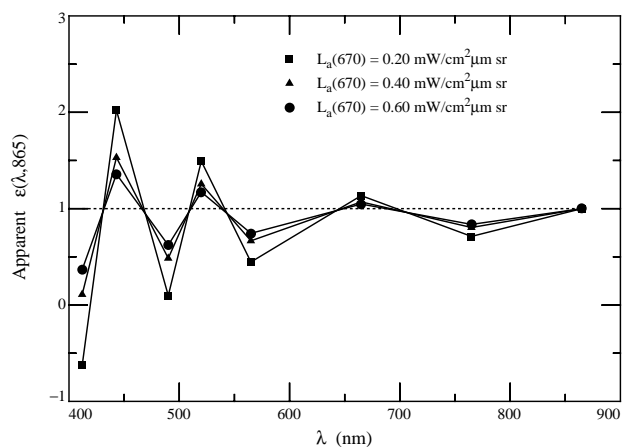


Figure 24a. Apparent value of $\varepsilon(\lambda, 865)$ for three values of $L_a(670)$. $\alpha(\lambda)$ alternates in sign from band to band and $|\alpha(\lambda)| = 0.05$.

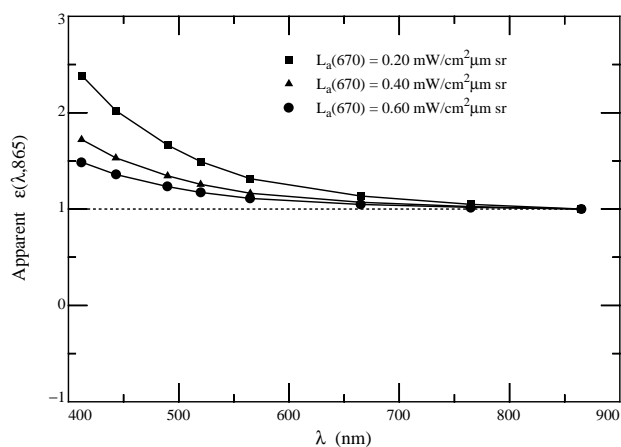


Figure 24b. Apparent value of $\varepsilon(\lambda, 865)$ for three values of $L_a(670)$. $\alpha(\lambda) = 0.05$ for all bands.

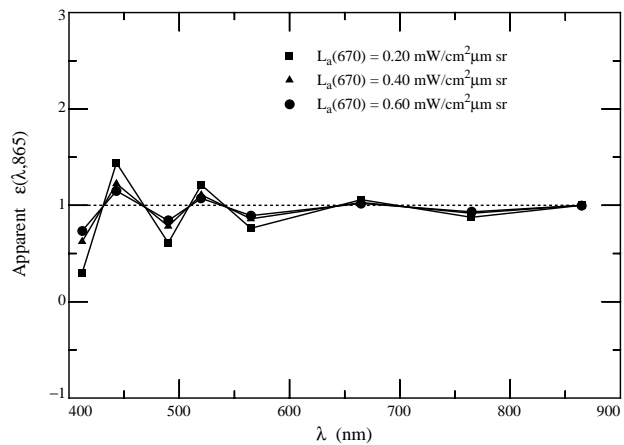


Figure 24c. Apparent value of $\varepsilon(\lambda, 865)$ for three values of $L_a(670)$. $\alpha(\lambda)$ alternates in sign from band to band and $|\alpha(\lambda)| = 0.03$.

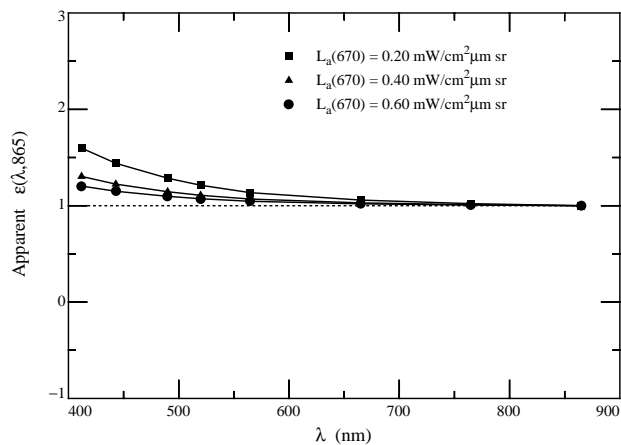


Figure 24d. Apparent value of $\varepsilon(\lambda, 865)$ for three values of $L_a(670)$. $\alpha(\lambda) = 0.03$ for all bands.

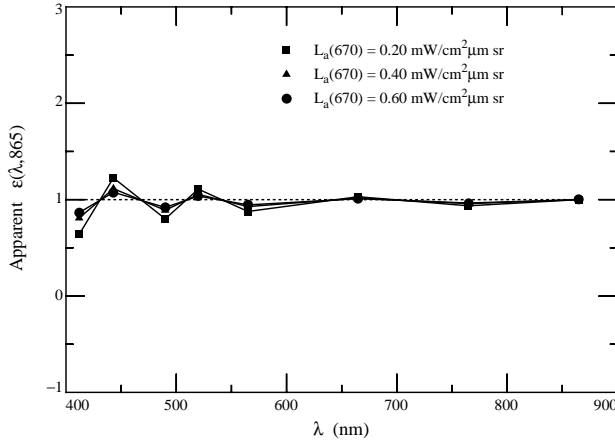


Figure 24e. Apparent value of $\varepsilon(\lambda, 865)$ for three values of $L_a(670)$. $\alpha(\lambda)$ alternates in sign from band to band and $|\alpha(\lambda)| = 0.01$.

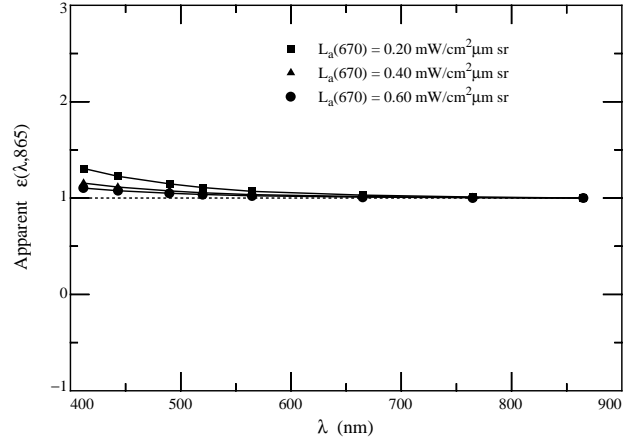


Figure 24f. Apparent value of $\varepsilon(\lambda, 865)$ for three values of $L_a(670)$. $\alpha(\lambda) = 0.01$ for all bands.

$$\alpha(\lambda_i) = \frac{\rho_t(\lambda_l)}{\rho_t(\lambda_i)} \varepsilon(\lambda_i, \lambda_l) \alpha(\lambda_l). \quad (21)$$

Thus, the residual errors ($\alpha(\lambda_i)$'s) will be $< \alpha(\lambda_l)$, since $\rho_t(\lambda_l) < \rho_t(\lambda_i)$ because of the strong spectral variation of ρ_r . We see that this form of calibration adjustment automatically reduces the error in the short-wave bands to a value below $\alpha(\lambda_l)$ and assures that all of the α 's have the same sign.

In practice Eq. (21) is useless because $\alpha(\lambda_l)$ is unknown. Thus, given $\varepsilon(\lambda_i, \lambda_l)$ one must actually adjust the calibration by trial and error to arrive at the correct values. This was done for the example in Figures 24a and 24b, where $\alpha(865) = +0.05$. The resulting residual α 's are presented in Table 10. The residual α 's follow the expected pattern, i.e., Eq. (21), and in the first three bands are reduced to less than 1%. [Note, however, that this method cannot even *detect* the error at λ_l .] In the presence of the residual errors in Table 10, the correction algorithm yields an error for $t\rho_w$ shown in Figure 25a. The error after this calibration adjustment is significantly reduced. In fact, it is similar to the error obtained when $\alpha(\lambda_i) \approx 0.02$. Figure 25b shows the further improvement that would be possible if $\alpha(\lambda_l)$ could be reduced to 0.025, half of its assumed initial value.

Table 10: Values of $\alpha(\lambda_i)$ required to produce a nearly correct $\varepsilon(\lambda_i, \lambda_l)$ for the examples in Figures 14a and 14b.

λ_i (nm)	$\alpha(\lambda_i)$
412	0.003
443	0.005
490	0.008
520	0.01
550	0.015
670	0.02
765	0.03

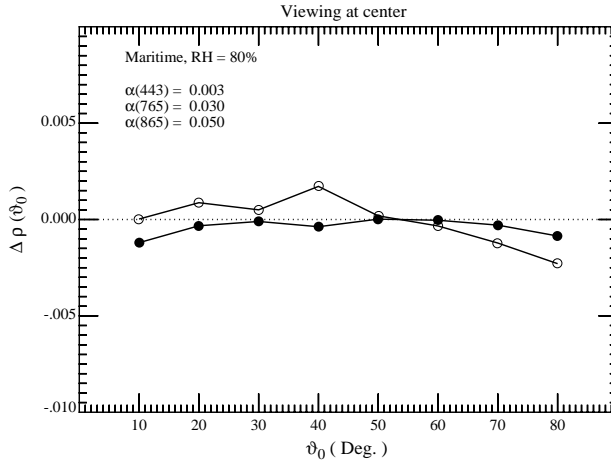


Figure 25a. Error in the retrieved $t(443)\rho_w(443)$ for viewing at the center of the scan with a Maritime aerosol at RH = 80% as a function of the solar zenith angle with $\tau_a(865) = 0.2$ and calibration errors $\alpha(443)$, $\alpha(765)$, and $\alpha(865)$ in Eq. (18) (open circles). Solid circles are for $\alpha(\lambda_i) = 0$ for all λ_i .

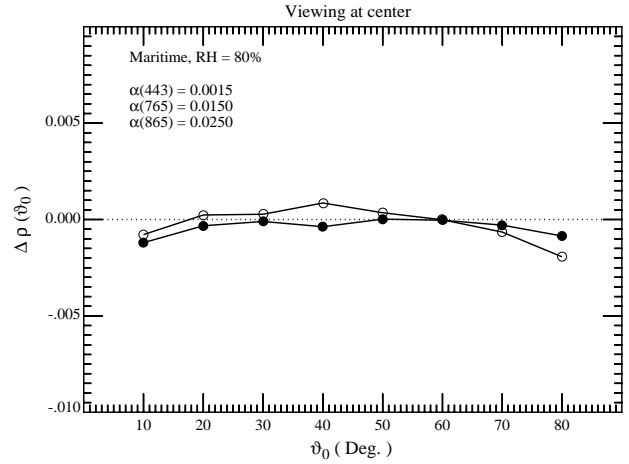


Figure 25b. Error in the retrieved $t(443)\rho_w(443)$ for viewing at the center of the scan with a Maritime aerosol at RH = 80% as a function of the solar zenith angle with $\tau_a(865) = 0.2$ and calibration errors $\alpha(443)$, $\alpha(765)$, and $\alpha(865)$ in Eq. (18) (open circles). Solid circles are for $\alpha(\lambda_i) = 0$ for all λ_i .

It is clear that the above method of calibration adjustment has the potential for reducing the calibration errors; however, to effect the adjustment we need a method of determining $\varepsilon(\lambda_i, \lambda_l)$ and a method for reducing the error at the long wave band — λ_l . We have investigated the accuracy to which measurement of $\tau_a(\lambda_i)$, for all λ_i , would allow a reasonable estimate of $\varepsilon(\lambda_i, \lambda_l)$. Figure 26 provides examples showing the existence of a rough relationship between $\tau_a(443)/\tau_a(865)$ and

$\varepsilon(443, 865)$ for all of the aerosol models used in this ATBD. Such models provide a prediction of $\varepsilon(443, 865)$.

To reduce $\alpha(\lambda_i)$ we propose measuring the optical properties of the aerosol. *Wang and Gordon* [1993] have shown how to combine measurements of τ_a and sky radiance over the oceans to obtain the aerosol phase function and single scatter albedo. Furthermore, the derived P_a and ω_a can be

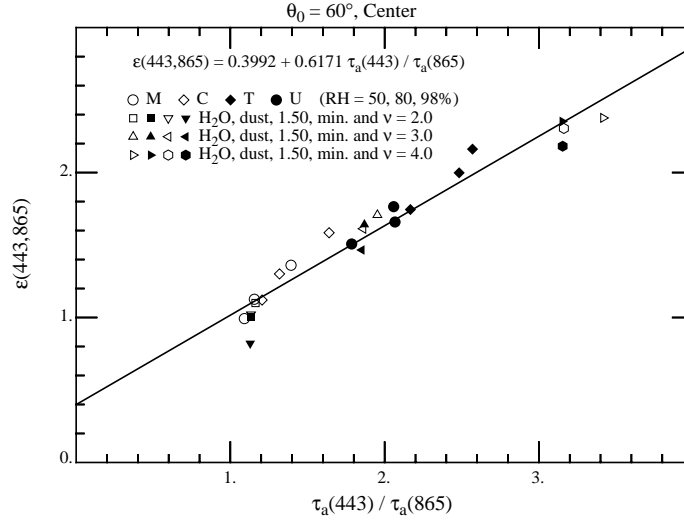


Figure 26. Relationship between $\tau_a(443)/\tau_a(865)$ and $\varepsilon(443, 865)$ at the scan center with $\theta_0 = 60^\circ$ for all of the test aerosol models used in Sections 3.1.1.1.2 and 3.1.1.4.

inserted into the RTE to predict ρ_t . *Gordon and Zhang* [1996] performed a complete error analysis of this procedure for predicting ρ_t and, as expected, under the most favorable conditions the error in the predicted ρ_t would be approximately the calibration uncertainty of the radiometer used in the measurement of the sky radiance, i.e., the accuracy of the procedure is the accuracy of the surface-based radiometer.

On the basis of the above discussion, we believe that it should be possible to reduce the $\alpha(\lambda_i)$'s to $\lesssim 0.02 - 0.03$ in the NIR, and to significantly smaller values in the visible. Also, the $\alpha(\lambda_i)$'s will all have the same sign. The resulting calibration will be maintained and fine-tuned by utilizing measurements of $[\rho_w]_N$ made with the marine optical buoy system (MOBY) being developed by D. Clark. In this scheme, a large amount of imagery acquired simultaneously with the surface data is examined, and again, assuming the algorithm is exact, the imagery is required to conform to the

surface measurements in a least-squares sense. This strategy will be used with SeaWiFS, and is proposed for MODIS.

It is important to stress again that the calibration described here is *not* radiometric, but rather a calibration of the entire system — sensor *plus* algorithms. Since we use F_0 to compute ρ_t in the procedure, the calibration is also relative to this quantity. An error in $F_0(\lambda_i)$ will influence the resulting value of $\alpha(\lambda_i)$; however, it will change in a very simple manner. The measured *radiance* L'_t is related to the true value L_t by $L'_t = L_t(1 + \alpha_L)$. This is converted to reflectance by multiplying by $\pi/F_0 \cos \theta_0$. If the extraterrestrial solar irradiance used in the conversion (F'_0) is in error by a fraction α_F , i.e., $F'_0 = F_0(1 + \alpha_F)$, where F_0 is the true value, then ρ'_t and ρ_t are related by

$$\rho'_t = \frac{(1 + \alpha_L)}{(1 + \alpha_F)} \rho_t \approx (1 + \alpha_L - \alpha_F) \rho_t.$$

Comparing with Eq. (18) we see that the value of $\alpha(\lambda_i)$ resulting from the procedure is really $\alpha_L(\lambda_i) - \alpha_F(\lambda_i)$, i.e., it includes the effect of *both* the calibration error and the solar irradiance error. Thus, our approach is pragmatic, no attempt is made to determine or understand the source of the error. The error in F_0 is independent of time, and as long as the radiometric sensitivity of the instrument is independent of time (or its variation is monitored by other means), the algorithms should perform as suggested by the analysis provided for Figures 23 and 25.

Summarizing, by combining the correction algorithm, measurements of $[\rho_w]_N$, and an estimate of $\varepsilon(\lambda_i, \lambda_l)$, it is possible to reduce the F_0 -sensor calibration error significantly, even with a rather large error ($\sim 5\%$) at λ_l . *This alone can provide a calibration that will yield atmospheric correction to nearly the desired accuracy.* Further reduction of the error requires reducing the error at λ_l . This can be accomplished by making atmospheric measurements sufficient to characterize the aerosol and then predicting $\rho_t(\lambda_l)$. The final calibration accuracy at λ_l will be approximately the same as the accuracy of the surface-based radiometer used to characterize the aerosols.

3.2.2.2 Validation

The validation of the $[\rho_w]_N$ product will be effected by comparing simultaneous surface-based measurements and MODIS-derived values at locations not used in the initialization measurements. Station locations will be chosen to provide a wide range of values of $[\rho_w]_N$. For ship-based validation experiments, aerosol properties (τ_a , ω_a , P_a) will be derived from measurements with sun

photometers and sky radiance cameras. This is described in detail in the validation plan provided as Appendix B.

3.2.3 Quality Assurance and Diagnostics

By “quality assurance” (QA) we mean providing the $[\rho_w]_N$ -user with information concerning when the product may not conform to expectations and should be used with caution. QA procedures are presently being developed in conjunction with R. Evans. Basically, if our assumptions are valid (Section 4.1), and the wind speed is $\lesssim 10$ m/s, the algorithm can be expected to perform properly except in situations where strongly absorbing aerosols are present (Sections 3.1.1.2 – 3.1.1.4). For these, no reliable algorithm exists at present. A climatology of geographical locations and times favorable for such aerosols will be developed (e.g., see *Husar, Stowe and Prospero [1996]*). We will also acquire TOMS data (if available) to reduce dependence on climatology. Generally absorbing aerosols will result in an overcorrection and $[\rho_w]_N$ will be too small; however, as $[\rho_w]_N$ may be small for other reasons, e.g., high pigment concentration, there is generally no simple rule that can be applied to determine whether the derived values are reasonable. To provide a QA measure we will compute the pigment concentration using Eq. (4) and keep a running tally of the concentration at low spatial resolution (TBD). We will then develop a metric for examination of imagery from climatologically suspect areas for anomalies, e.g., large and unexplained variations in the chlorophyll concentration or its spatial pattern. When such anomalies are detected, they will be compared to the absorbing-aerosol data (or climatology). If absorbing aerosols are believed to be the problem, the imagery will be either flagged as being unreliable, or reprocessed with a special algorithm (TBD). Otherwise, the imagery will be flagged as not conforming to expectations.

3.2.4 Exception Handling

Exceptions occasionally occur in a manner that prevents operation of the algorithm, e.g., missing data in bands 15 or 16, or in a manner that would cause exceptions in algorithms using $[\rho_w]_N$, e.g., negative values of $[\rho_w]_N$ caused by atmospheric correction errors (particularly in the blue at high pigment concentrations where $[\rho_w]_N$ is small). A series of flags will be developed to indicate when atmospheric correction should not be attempted, or to indicate that algorithm failed to operate or failed to provide realistic values for $[\rho_w(\lambda)]_N$.

3.2.5 Data Dependencies

The required ancillary data is described in detail in Section 3.1.1.7. All, with the exception of the total Ozone concentration, will come from numerical weather models via NMC. Ozone will be derived from MODIS data itself by the atmosphere group. An additional data set, the global concentration of absorbing aerosols from TOMS, is desirable, at least for QA. The avenue for acquiring such data is being investigated. If a particular data set is not available either a nominal value, e.g., the oceanic average, or a climatology will be substituted. A method of handling any discontinuity that is introduced by not using the “best” data set will be developed.

3.2.6 Output Products

The output products are the normalized water-leaving radiances in MODIS bands 8–14, the aerosol optical thickness $\tau_a(\lambda_l)$, $\varepsilon(\lambda_s, \lambda_l)$, and an index describing the two candidate models selected by the algorithm to perform the $[\rho_w]_N$ retrievals. Based on our observations that the combination of $\varepsilon(\lambda_s, \lambda_l) \sim 1$ and small $\tau_a(\lambda_l)$ yields a very good retrieval of $[\rho_w]_N$, while $\varepsilon(\lambda_s, \lambda_l) \sim 1.2$ and large $\tau_a(\lambda_l)$ may yield a poor retrieval, a quality index will be developed based on a combination of the values of $\varepsilon(\lambda_s, \lambda_l)$ and $\tau_a(\lambda_l)$. This index will also be an output product along with a flag indicating the possible presence of strongly absorbing aerosols (Section 3.1.1.4).

4.0 Assumptions and Constraints

In this section we describe the assumptions that have been made and how they may influence the resulting $[\rho_w]_N$. We also provide a list of situations in which the algorithm cannot be operated.

4.1 Assumptions

The principal assumption is the validity of the aerosol models used for the implementation of the algorithm, i.e., in developing the lookup tables described in Section 3.1.1.3. We have seen in Section 3.1.1.4 that the algorithm will work well if the models are a reasonable approximation to nature, but if they are unrealistic, i.e., mineral dust without absorption, the error in $[\rho_w]_N$ can be excessive (Figure 11). In fact, Figure 11 shows that it is of vital importance to have the correct absorptive properties of the aerosol. The adequacy of the aerosol models is difficult to judge. For the most part they were developed to model beam propagation, i.e., the total scattering and

extinction coefficients, not the scattering phase function and the single scatter albedo. They have not been validated for these quantities; however, *Schwindling* [1995] showed that the aerosol off the coast of Southern California appeared to fall within the boundaries of the *Shettle and Fenn* [1979] aerosol models used here. Other models are available, e.g., *d'Almeida, Koepke and Shettle* [1991] provide maritime models with 4 and 5 components, each of which is RH dependent; however, these have not been validated either. As part of our MODIS pre-launch effort (Section 3.1.1.9.2) and our SeaWiFS and MODIS initialization (Section 3.2.2.1), we are making sky radiance measurements over the ocean and plan to invert them to obtain $P_a(\alpha, \lambda)$ and $\omega_a(\lambda)$ for direct comparison with the predictions of the models. This will provide further information on the adequacy of the models.

A second, probably less important, assumption is that the radiative transfer in the atmosphere can be adequately described by a two-layer model (aerosols in the lower layer only). Based on tests with absorbing aerosols, we know that this model will have to be changed, e.g., Saharan dust will have to be mixed higher into the atmosphere. This will require generation of new lookup tables. We have planned our Team Member Computing Facility to have sufficient power to generate such tables in a reasonable length of time.

Finally, it is assumed that the water-leaving radiance in the NIR is essentially zero. This is usually an excellent assumption in the open ocean; however, in very concentrated coccolithophore blooms [*Balch et al.*, 1991; *Gordon et al.*, 1988] it is possible that the ocean will contribute NIR radiance. The magnitude of this NIR radiance as a function of the coccolith concentration will be established experimentally as part of a study to derive the concentration from MODIS imagery.

4.2 Constraints

Although algorithm will employ the cloud mask being developed by the MODIS Atmosphere Group to indicate the presence of thin cirrus clouds; an atmospheric correction will be attempted for all imagery that is not saturated in bands 15 and 16. Of these cloud-free pixels, the algorithm requires that they contain no land and that the estimated sun glitter contamination be below a pre-determined threshold (Appendix A). Also, the algorithm should not be applied closer than a distance x from land (the value of x is TBD) due to the adjacency effect from land pixels [*Otterman and Fraser*, 1979] and the possibility of sufficiently high sediment loads in the water that $[\rho_w]$ can not be considered negligible in the NIR.

References

- d'Almeida, G. A., P. Koepke and E. P. Shettle, *Atmospheric Aerosols — Global Climatology and Radiative Characteristics*, A. Deepak Publishing, Hampton, VA, 1991.
- André, J. -M. and A. Morel, Atmospheric Corrections and Interpretation of Marine Radiances in CZCS Imagery, Revisited, *Oceanologica Acta*, 14, 3–22, 1991.
- Balch, W. M., P. M. Holligan, S. G. Ackleson and K. J. Voss, Biological and optical properties of mesoscale coccolithophore blooms in the Gulf of Maine, *Limnology and Oceanography*, 34, 629–643, 1991.
- Barnes, R. A., A. W. Holmes, W. L. Barnes, W. E. Esaias, C. R. McClain and T. Svitek, *SeaWiFS Technical Report Series: Volume 23, SeaWiFS Prelaunch Radiometric Calibration and Spectral Characterization*, NASA, Greenbelt, MD, Technical Memorandum 104566, October 1994.
- Bricaud, A. and A. Morel, Atmospheric Corrections and Interpretation of Marine Radiances in CZCS Imagery: Use of a Reflectance Model, *Oceanologica Acta*, 7, 33–50, 1987.
- Charlson, R. J., J. E. Lovelock, M. O. Andreae and S. G. Warren, Oceanic phytoplankton, atmospheric sulphur, cloud albedo and climate, *Nature*, 326, 655–661, 1987.
- Charlson, R. J., S. E. Schwartz, J. M. Hales, R. D. Cess, J. A. Coakley, J. E. Hansen and D. J. Hofmann, Climate Forcing by Anthropogenic Aerosols, *Science*, 255, 423–430, 1992.
- Clarke, G. L., G. C. Ewing and C. J. Lorenzen, Spectra of Backscattered Light from the Sea Obtained From Aircraft as a Measurement of Chlorophyll Concentration, *Science*, 167, 1119–1121, 1970.
- Cox, C. and W. Munk, Measurements of the Roughness of the Sea Surface from Photographs of the Sun's Glitter, *Jour. Opt. Soc. of Am.*, 44, 838–850, 1954.

- Deirmendjian, D., *Electromagnetic Scattering on Spherical Polydispersions*, Elsevier, New York, NY, 1969, 290 pp.
- Deschamps, P. Y., M. Herman and D. Tanre, Modeling of the atmospheric effects and its application to the remote sensing of ocean color, *Applied Optics*, 22, 3751–3758, 1983.
- Ding, K. and H. R. Gordon, Atmospheric correction of ocean color sensors: Effects of earth curvature, *Applied Optics*, 33, 7096–7016, 1994.
- Ding, K. and H. R. Gordon, Analysis of the influence of O₂ A-band absorption on atmospheric correction of ocean color imagery, *Applied Optics*, 34, 2068–2080, 1995.
- Durkee, P. A., D. R. Jensen, E. E. Hindman and T. H. V. Haar, The Relationship Between Marine Aerosol Particles and Satellite-Detected Radiance, *Jour. Geophys. Res.*, 91D, 4063–4072, 1986.
- Eldridge, R. G., Water Vapor Absorption of Visible and Near Infrared Radiation, *Applied Optics*, 4, 709–713, 1967.
- Evans, R. H. and H. R. Gordon, CZCS ‘System Calibration:’ A retrospective examination, *Jour. Geophys. Res.*, 99C, 7293–7307, 1994.
- Falkowski, P. G., Y. Kim, Z. Kolber, C. Wilson, C. Wirick and R. Cess, Natural Versus Anthropogenic Factors Affecting Low-Level Cloud Albedo over the North Atlantic, *Science*, 256, 1311–1313, 1992.
- Feldman, G. C., N. Kuring, C. Ng, W. Esaias, C. R. McClain, J. Elrod, N. Maynard, D. Endres, R. Evans, J. Brown, S. Walsh, M. Carle and G. Podesta, Ocean Color: Availability of the Global Data Set, *EOS Trans. Amer. Geophys. Union*, 70, 634–641, 1989.
- Fraser, R. S., Degree of Interdependence among Atmospheric Optical Thickness in Spectral Bands between 0.36 and 2.4 μm , *Applied Optics*, 14, 1187–1196, 1975.

- Fraser, R. S., Satellite measurement of mass of Sahara dust in the atmosphere, *Applied Optics*, 15, 2471–2479, 1976.
- Fraser, R. S. and Y. J. Kaufman, Calibration of satellite sensors after launch, *Applied Optics*, 25, 1177–1185, 1986.
- Frouin, R., M. Schwindling and P. Y. Deschamps, Spectral reflectance of sea foam in the visible and near-infrared: In-situ measurements and implications for remote sensing of ocean color and aerosols, *Jour. Geophys. Res.*, 101C, 14,361–14,371, 1996.
- Gao, B. -C., A. F. H. Goetz and W. J. Wiscombe, Cirrus cloud detection from airborne imaging spectrometer data using the 1.38 micron water vapor band, *Geophysical Research Letters*, 20, 301–304, 1993.
- Gordon, H. R., Radiative Transfer: A Technique for Simulating the Ocean in Satellite Remote Sensing Calculations, *Applied Optics*, 15, 1974–1979, 1976.
- Gordon, H. R., Removal of Atmospheric Effects from Satellite Imagery of the Oceans, *Applied Optics*, 17, 1631–1636, 1978.
- Gordon, H. R., Calibration Requirements and Methodology for Remote Sensors Viewing the Oceans in the Visible, *Remote Sensing of Environment*, 22, 103–126, 1987.
- Gordon, H. R., Ocean Color Remote Sensing Systems: Radiometric Requirements, *Society of Photo-Optical Instrumentation Engineers, Recent Advances in Sensors, Radiometry, and Data Processing for Remote Sensing*, 924, 151–167, 1988.
- Gordon, H. R., Radiometric Considerations for Ocean Color Remote Sensors, *Applied Optics*, 29, 3228–3236, 1990.
- Gordon, H. R., Remote sensing of ocean color: a methodology for dealing with broad spectral bands and significant out-of-band response, *Applied Optics*, 34, 8363–8374, 1995.

- Gordon, H. R., J. W. Brown and R. H. Evans, Exact Rayleigh Scattering Calculations for use with the Nimbus-7 Coastal Zone Color Scanner, *Applied Optics*, 27, 862–871, 1988.
- Gordon, H. R., O. B. Brown, R. H. Evans, J. W. Brown, R. C. Smith, K. S. Baker and D. K. Clark, A Semi-Analytic Radiance Model of Ocean Color, *Jour. Geophys. Res.*, 93D, 10909–10924, 1988.
- Gordon, H. R. and D. J. Castaño, The Coastal Zone Color Scanner Atmospheric Correction Algorithm: Multiple Scattering Effects, *Applied Optics*, 26, 2111–2122, 1987.
- Gordon, H. R. and D. J. Castaño, The Coastal Zone Color Scanner Atmospheric Correction Algorithm: Influence of El Chichón, *Applied Optics*, 27, 3319–3321, 1988.
- Gordon, H. R. and D. K. Clark, Atmospheric effects in the remote sensing of phytoplankton pigments, *Boundary-Layer Meteorology*, 18, 299–313, 1980.
- Gordon, H. R. and D. K. Clark, Clear water radiances for atmospheric correction of coastal zone color scanner imagery, *Applied Optics*, 20, 4175–4180, 1981.
- Gordon, H. R., D. K. Clark, J. W. Brown, O. B. Brown, R. H. Evans and W. W. Broenkow, Phytoplankton pigment concentrations in the Middle Atlantic Bight: comparison between ship determinations and Coastal Zone Color Scanner estimates, *Applied Optics*, 22, 20–36, 1983.
- Gordon, H. R., D. K. Clark, J. L. Mueller and W. A. Hovis, Phytoplankton pigments derived from the Nimbus-7 CZCS: initial comparisons with surface measurements, *Science*, 210, 63–66, 1980.
- Gordon, H. R. and M. Wang, Surface Roughness Considerations for Atmospheric Correction of Ocean Color Sensors. 2: Error in the Retrieved Water-leaving Radiance, *Applied Optics*, 31, 4261–4267, 1992a.

- Gordon, H. R. and M. Wang, Surface Roughness Considerations for Atmospheric Correction of Ocean Color Sensors. 1: The Rayleigh Scattering Component, *Applied Optics*, 31, 4247–4260, 1992b.
- Gordon, H. R. and M. Wang, Influence of Oceanic Whitecaps on Atmospheric Correction of SeaWiFS, *Applied Optics*, 33, 7754–7763, 1994a.
- Gordon, H. R. and M. Wang, Retrieval of water-leaving radiance and aerosol optical thickness over the oceans with SeaWiFS: A preliminary algorithm, *Applied Optics*, 33, 443–452, 1994b.
- Gordon, H. R. and T. Zhang, 1996, How well can radiance reflected from the ocean-atmosphere system be predicted from measurements at the sea surface?, *Applied Optics* (In press).
- Gordon, H. R., T. Zhang, F. He and K. Ding, 1996, Effects of stratospheric aerosols and thin cirrus clouds on atmospheric correction of ocean color imagery: Simulations, *Applied Optics* (In press).
- Grant, W. B., E. V. Browell, C. F. Butler, M. A. Fenn and G. D. Nowicki, Comparisons of Electra-Lidar and LITE Atmospheric Measurements Near the East Coast of the U.S. and the Caribbean, *EOS, Transactions, American Geophysical Union*, 76, S70, 1995.
- Griggs, M., Measurements of the Aerosol Optical Thickness Over Water Using ERTS-1 Data, *Jour. Air Poll. Contr. Assoc.*, 25, 622–626, 1975.
- Griggs, M., Satellite Measurements of Tropospheric Aerosols, NASA, Contractor Report 3459, August 1981.
- Griggs, M., AVHRR Aerosol Ground Truth Experiment, NOAA National Environmental Satellite Service, Final Report Contract No. NA-83-SAC-00106, January 1984.
- Griggs, M., AVHRR Measurements of Atmospheric Aerosols Over Oceans, NOAA National Environmental Satellite Service, Final Report Contract No. M0-A01-78-00-4092, November 1981.

- Hale, G. M. and M. R. Querry, Optical Constants of Water in the 200-nm to 200- μ m Wavelength Region, *Applied Optics*, 12, 555–563, 1973.
- Hansen, J. E. and L. D. Travis, Light Scattering in Planetary Atmospheres, *Space Science Reviews*, 16, 527–610, 1974.
- Herman, J. R., P. K. Bhartia, O. Torres, C. Hsu, C. Seftor and E. Celarier, Global Distribution of Absorbing Aerosols from Nimbus-7/TOMS Data, 1996, *Jour. Geophys. Res.* (Submitted).
- Holben, B. N., T. F. Eck, I. Slutsker, D. Tanre, J. P. Buis, A. Setzer, E. Vermote, J. Reagan, Y. Kaufman, T. Nakajima, F. Lavenu and I. Jankowiak, 1996, Automatic Sun and Sky Scanning Radiometer System for Network Aerosol Monitoring, *Remote Sensing of Environment* (In press) .
- Hovis, W. A., D. K. Clark, F. Anderson, R. W. Austin, W. H. Wilson, E. T. Baker, D. Ball, H. R. Gordon, J. L. Mueller, S. Y. E. Sayed, B. Strum, R. C. Wrigley and C. S. Yentsch, Nimbus 7 coastal zone color scanner: system description and initial imagery, *Science*, 210, 60–63, 1980.
- van de Hulst, H. C., *Multiple Light Scattering*, Academic Press, New York, 1980, 739 pp.
- Husar, R. B., L. L. Stowe and J. M. Prospero, 1996, Satellite Sensing of Tropospheric Aerosols Over the Oceans with NOAA AVHRR, *Jour. Geophys. Res.* (Submitted).
- Ismail, S., E. V. Browell, S. A. Kooi and G. D. Nowicki, Simultaneous LASE and LITE Aerosol Profile Measurements over the Atlantic, *EOS, Transactions, American Geophysical Union*, 76, S71, 1995.
- Junge, C., Atmospheric Chemistry, *Advances in Geophysics*, 4, 1–108, 1958.
- Kattawar, G. W., G. N. Plass and S. J. Hitzfelder, Multiple scattered radiation emerging from Rayleigh and continental haze layers. 1: Radiance, polarization, and neutral points, *Applied Optics*, 15, 632–647, 1976.

- Kenizys, F. X., E. P. Shettle, W. O. Gallery, J.H.Chetwynd, L. W. Abreu, J. E. A. Selby, S. A. Clough and R. W. Fenn, Atmospheric Transmittance/Radiance: The LOWTRAN 6 Model, Air Force Geophysics Laboratory, Hanscomb AFB, MA 01731, AFGL-TR-83-0187, 1983, NTIS AD A137796.
- King, M. D., Harshvardhan and A. Arking, A Model of the Radiative Properties of the El Chichón Stratospheric Aerosol Layer, *Journal of Climate and Applied Meteorology*, 23, 1121-1137, 1984.
- Koepke, P., Vicarious Satellite Calibration in the Solar Spectral Range by Means of Calculated Radiances and its Application to Meteosat, *Applied Optics*, 21, 2845-2854, 1982.
- Koepke, P., Effective Reflectance of Oceanic Whitecaps, *Applied Optics*, 23, 1816-1824, 1984.
- Koepke, P. and H. Quenzel, Turbidity of the Atmosphere Determined From Satellite: Calculation of Optimum Viewing Geometry, *Jour. Geophys. Res.*, 84(C12), 7847-7856, 1979.
- Koepke, P. and H. Quenzel, Turbidity of the Atmosphere Determined From Satellite: Calculation of Optimum Wavelength, *Jour. Geophys. Res.*, 86(C10), 9801-9805, 1981.
- Korotaev, G. K., S. M. Sakerin, A. M. Ignatov, L. L. Stowe and E. P. McClain, Sun-Photometer Observations of Aerosol Optical Thickness over the North Atlantic from a Soviet Research Vessel for Validation of Satellite Measurements, *Jour. Atmos. Oceanic Technol.*, 10, 725-735, 1993.
- Lechner, I. S., G. W. Fisher, H. R. Larsen, M. J. Harvey and R. A. Knobbens, Aerosol Size Distributions in the Southwest Pacific, *Jour. Geophys. Res.*, 94D, 14893-14903, 1989.
- McCormick, M. P., LITE - An Overview, *EOS, Transactions, American Geophysical Union*, 76, S66, 1995.
- Mekler, Y., H. Quenzel, G. Ohring and I. Marcus, Relative Atmospheric Aerosol Content from Erts Observations, *Jour. Geophys. Res.*, 82, 967-970, 1977.

- Mishchenko, M. I. and L. D. Travis, Light scattering by polydispersions of randomly oriented spheroids with sizes comparable to wavelengths of observation, *Applied Optics*, 33, 7206–7225, 1994.
- Monahan, E. C., Oceanic Whitecaps, *J. Phys. Oceanogr.*, 1, 139–144, 1971.
- Monahan, E. C. and I. G. O’Muircheartaigh, Whitecaps and the passive remote sensing of the ocean surface, *Int. J. Remote Sensing*, 7, 627–642, 1986.
- Morel, A. and J. -M. André, Pigment Distribution and Primary Production in the Western Mediterranean as Derived and Modeled From Coastal Zone Color Scanner Observations, *Jour. Geophys. Res.*, 96C, 12,685–12,698, 1991.
- Morel, A. and B. Gentili, Diffuse reflectance of oceanic waters: its dependence on Sun angle as influenced by the molecular scattering contribution, *Applied Optics*, 30, 4427–4438, 1991.
- Morel, A. and B. Gentili, Diffuse reflectance of oceanic waters. II. Bidirectional aspects, *Applied Optics*, 32, 6864–6879, 1993.
- Morel, A. and B. Gentili, 1996, Diffuse reflectance of oceanic waters. III. Implication of bidirectionality for the remote sensing problem, *Applied Optics* (In press).
- Morel, A., K. J. Voss and B. Gentili, Bidirectional reflectance of oceanic waters: A comparison of modeled and measured upward radiance fields, *Jour. Geophys. Res.*, 100C, 13,143–13,150, 1995.
- Mugnai, A. and W. J. Wiscombe, Scattering from nonspherical Chebyshev particles. 3: Variability in angular scattering patterns, *Applied Optics*, 28, 3061–3073, 1989.
- Nakajima, T., M. Tanaka, M. Yamano, M. Shiobara, K. Arao and Y. Nakanishi, Aerosol Optical Characteristics in the Yellow Sand Events Observed in May 1982 at Nagasaki – Part II Models, *Jour. Meteorological Soc. Japan*, 67, 279–291, 1989.

- Neckel, H. and D. Labs, The Solar Radiation Between 3300 and 12500 Å, *Solar Physics*, 90, 205–258, 1984.
- Neville, R. A. and J. F. R. Gower, Passive Remote Sensing of Phytoplankton via Chlorophyll α Fluorescence, *Jour. Geophys. Res.*, 82C, 3487–3493, 1977.
- Otterman, J. and R. S. Fraser, Adjacency effects on imaging by surface reflection and atmospheric scattering: cross radiance to zenith, *Applied Optics*, 18, 2852–2860, 1979.
- Platt, T. and S. Sathyendranath, Oceanic Primary Production: Estimation by Remote Sensing at Local and Regional Scales, *Science*, 241, 1613–1620, 1988.
- Rao, C. R. N., L. L. Stowe, E. P. McClain and J. Sapper, Developemnt and Application of Aerosol Remote Sensing with AVHRR Data from the NOAA Satellites, in *Aerosols and Climate*, edited by P. Hobbs and M. P. McCormick, pp. 69–80, Deepak, Hampton, VA, 1988.
- Reddy, P. J., F. W. Kreiner, J. J. Deluisi and Y. Kim, Aerosol Optical Depths Over the Atlantic Derived From Shipboard Sunphotometer Observations During the 1988 Global Change Expedition, *Global Biogeochemical Cycles*, 4, 225–240, 1990.
- Sasano, Y. and E. V. Browell, Light scattering characteristics of various aerosol types derived from multiple wavelength lidar observations, *Applied Optics*, 28, 1670–1679, 1989.
- Schwindling, M., Modeles et mesures pour l'observation spatiale de la couleur de l'ocean: Diffusion atmospherique par les aerosols et reflexion de surface par l'ecume, 1995, Docteur de L'Universite these, Univ. des Sci. et Tech. de Lille. 245 pp.
- Shettle, E. P. and R. W. Fenn, Models for the Aerosols of the Lower Atmosphere and the Effects of Humidity Variations on Their Optical Properties, Air Force Geophysics Laboratory, Hanscomb AFB, MA 01731, AFGL-TR-79-0214, 1979.
- Slater, P. N., S. F. Biggar, R. G. Holm, R. D. Jackson, Y. Mao, M. S. Moran, J. M. Palmer and B. Yuan, Reflectance- and Radiance-Based Methods for the In-Flight Absolute Calibration of Multispectral Sensors, *Remote Sensing of Environment*, 22, 11–37, 1987.

- Smith, R. C., Structure of Solar Radiation in the Upper Layers of the Sea, in *Optical Aspects of Oceanography*, edited by N. G. Jerlov and E. S. Nielsen, pp. 95–119, Academic Press, New York, NY, 1974.
- Smith, R. C. and W. H. Wilson, Ship and satellite bio-optical research in the California Bight, in *Oceanography from Space*, edited by J. F. R. Gower, pp. 281–294, Plenum, New York, NY, 1981.
- Spinhirne, J. D., Micro Pulse Lidar, *IEEE Transactionson Geoscience and Remote Sensing*, 31, 48–55, 1993.
- Tomasi, C., Non-selective absorption by atmospheric water vapour at visible and near infrared wavelengths, *Quart. J. R. Met. Soc.*, 105, 1027–1040, 1979a.
- Tomasi, C., Weak Absorption by Atmospheric Water Vapour in the Visible and Near-Infrared Spectral Region, *Nuovo Cimento*, 2C, 511–526, 1979b.
- Villevalde, Y. V., A. V. Smirnov, N. T. O'Neill, S. P. Smyshlyaev and V. V. Yakovlev, Measurement of Aerosol Optical Depth in the Pacific Ocean and North Atlantic, *Jour. Geophys. Res.*, 99D, 20983–20988, 1994.
- Voss, K. J., Electro-optic Camera System for Measurement of the Underwater Radiance Distribution, *Optical Engineering*, 28, 241–247, 1989.
- Wang, M. and H. R. Gordon, Retrieval of the Columnar Aerosol Phase Function and Single Scattering Albedo from Sky Radiance over the Ocean: Simulations, *Applied Optics*, 32, 4598–4609, 1993.
- Wang, M. and H. R. Gordon, A Simple, Moderately Accurate, Atmospheric Correction Algorithm for SeaWiFS, *Remote Sensing of Environment*, 50, 231–239, 1994.
- Whitlock, C. H., D. S. Bartlett and E. A. Gurganus, Sea Foam Reflectance and Influence on Optimum Wavelength for Remote Sensing of Ocean Aerosols, *Geophys. Res. Lett.*, 7, 719–722, 1982.

Glossary

AERONET	Aerosol Robotic Network
ATBD	Algorithm Theoretical Basis Document
CZCS	Coastal Zone Color Scanner
IOP	Inherent Optical Property
MOBY	Marine Optical Buoy
MODIS	Moderate-Resolution Spectroradiometer
$NE\Delta\rho$	Noise Equivalent Reflectance
NIR	Near infrared (700–1000 nm)
RTE	Radiative Transfer Equation
SeaWiFS	Sea-viewing Wide-Field-of-view Sensor
SNR	Signal-to-noise Ratio
SRCA	Spectroradiometric Calibration Assembly
TBD	To be determined
TOMS	Total Ozone Mapping Spectrometer (Nimbus-7)

**MODIS Normalized Water-leaving Radiance
Algorithm Theoretical Basis Document**

Version 3

**Appendix A
MODIS Sun Glitter Mask**

Submitted by

**Howard R. Gordon
Department of Physics
University of Miami
Coral Gables, FL 33124**

Under Contract Number NAS5-31363

August 15, 1996

In this appendix we provide the equations required to prepare a mask to flag pixels that are seriously contaminated by sun glitter. The intention is that the sun glitter mask be applied to the imagery prior to the application of the normalized water-leaving radiance retrieval algorithm described in the text of this ATBD. This application could occur at an earlier processing level, or as the first step of the retrieval algorithm.

Sun Glitter Reflectance ρ_g

The contribution to the MODIS-measured radiance at the TOA from sun glitter — the specular reflection of sunlight from the sea surface and propagation to the sensor — is based on the

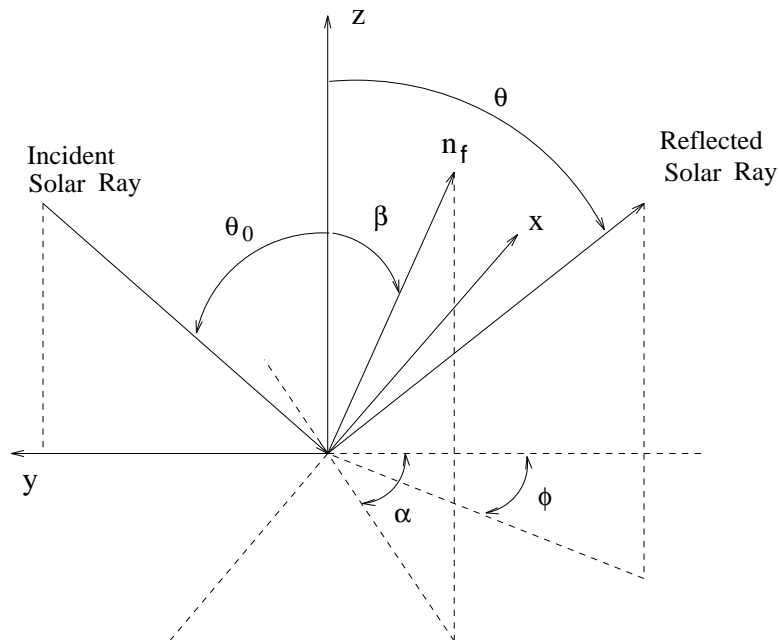


Figure 1. Geometry of reflection from a rough sea surface. n_f is the unit normal to the facet that is oriented properly to reflect the sunlight as shown.

formulation of *Cox and Munk* [1954]. In this development the sea surface is modeled as a collection of facets with individual slope components z_x and z_y . In a coordinate system with the $+y$ axis pointing toward the sun (projection of the sun's rays on the sea surface is along the $-y$ axis), given the solar zenith angle and the angles θ and ϕ specifying the reflected ray, the orientation (β, α) of

the facet normal n_f (Figure 1) required for a facet to reflect sunlight in the direction of (θ, ϕ) is found from the following equations

$$\begin{aligned}\cos(2\omega) &= \cos \theta \cos \theta_0 - \sin \theta \sin \theta_0 \cos \phi \\ \cos \beta &= (\cos \theta + \cos \theta_0)/2 \cos \omega \\ \cos \alpha &= (\cos \phi \cos \theta - \sin \theta)/2 \cos \omega \sin \beta \\ \sin \alpha &= (\sin \phi \cos \theta)/2 \cos \omega \sin \beta \\ z_x &= \sin \alpha \tan \beta \\ z_y &= \cos \alpha \tan \beta.\end{aligned}$$

Note that for a flat (smooth) surface, $\phi = 0$. Let χ be the angle between the projection of the sun's rays on the sea surface and the direction of the wind vector \vec{W} , i.e., if $\chi = 0$ the wind vector points in the direction of $-y$ in Figure 1. χ is measured positive in a clockwise direction (looking toward the surface), i.e., if $0 < \chi < 90^\circ$, the wind vector is in the quadrant formed by the $-x$ and $-y$ axes. Then, the defining the glitter reflectance ρ_g to be the radiance reflected from the sea surface, L_g , times $\pi/F_0 \cos \theta_0$, where F_0 is the extraterrestrial solar irradiance, ρ_g is given by

$$\rho_g(\theta, \phi; \theta_0, \phi_0) = \frac{\pi r(\omega)}{4 \cos \theta_0 \cos \theta \cos^4 \beta} p(z'_x, z'_y)$$

where $p(z'_x, z'_y)$ is the probability density of surface slopes given by

$$p(z'_x, z'_y) = (2\pi\sigma_u\sigma_c)^{-1} \exp[-(\xi^2 + \eta^2)/2] \left[1 + \sum_{i=1}^{\infty} \sum_{j=1}^{\infty} c_{ij} H_i(\xi) H_j(\eta) \right],$$

with

$$\xi = z'_x/\sigma_c = \sin \alpha' \tan \beta/\sigma_c$$

$$\eta = z'_y/\sigma_u = \cos \alpha' \tan \beta/\sigma_u$$

$$\alpha' = \alpha - \chi.$$

$r(\omega)$ is the Fresnel reflectance for unpolarized light incident at an angle ω , and H_i is the Hermite polynomial of order i . The constants σ_u , σ_c , and c_{ij} were determined by Cox and Munk by fitting

the radiance from glitter patterns photographed from aircraft to these equations. They are

$$\sigma_c^2 = 0.003 + 1.92 \times 10^{-3} W \pm 0.002$$

$$\sigma_u^2 = 0.000 + 3.16 \times 10^{-3} W \pm 0.004$$

$$c_{21} = 0.01 - 8.6 \times 10^{-3} W \pm 0.03$$

$$c_{03} = 0.04 - 33 \times 10^{-3} W \pm .012$$

$$c_{40} = 0.40 \pm 0.23$$

$$c_{22} = 0.12 \pm 0.06$$

$$c_{04} = 0.23 \pm 0.41$$

The contribution of ρ_g to the reflectance measured at the top of the atmosphere, $T\rho_g$, where T is the direct transmittance of the atmosphere, is just

$$\rho_g \exp \left[-\tau \left(\frac{1}{\cos \theta} + \frac{1}{\cos \theta_0} \right) \right],$$

where τ is the total optical thickness of the atmosphere.

The sun glitter mask is uses the wind vector \vec{W} to estimate ρ_g for each pixel, and if the estimate is larger than a threshold value (to be determined) the pixel is flagged and the normalized water-leaving radiance algorithm is not applied. As the aerosol optical thickness is unknown at the time of the application of this mask, the conservative approach is taken by choosing $\tau_a = 0$.

Reference

Cox, C. and W. Munk, Measurements of the Roughness of the Sea Surface from Photographs of the Sun's Glitter, *Jour. Opt. Soc. of Am.*, 44, 838–850, 1954.

**MODIS Normalized Water-leaving Radiance
Algorithm Theoretical Basis Document**

Version 3

Appendix B

Validation Plan

Submitted by

**Howard R. Gordon
Department of Physics
University of Miami
Coral Gables, FL 33124**

Under Contract Number NAS5-31363

August 15, 1996

Preface

The text of this validation plan is from a paper “Validation of Atmospheric Correction over the Oceans” by D. K. Clark¹, H.R. Gordon², K.J. Voss², Y. Ge³, W. Broenkow⁴, and C. Trees,⁵ presented at the Aerosol Remote Sensing Workshop, Sponsored by NASA/EOS, April 15–19, 1996, Washington, D.C.

¹ NOAA/NESDIS, Camp Springs, MD 20746

² Department of Physics, University of Miami, Coral Gables, FL 33124

³ Research and Data Corporation, Greenbelt MD, 20770

⁴ Moss Landing Marine Laboratories, San Jose State University, Moss Landing, CA 95039

⁵ CHORS, San Diego State University, San Diego, CA 92120

Abstract

By validation of atmospheric correction, we mean quantification of the uncertainty expected to be associated with the retrieval of the water-leaving radiance from the measurement of the total radiance exiting the ocean-atmosphere system. This uncertainty includes that associated with the measurement or estimation of auxiliary data required for the retrieval process, e.g., surface wind speed, surface atmospheric pressure, and total Ozone concentration. For a definitive validation, this quantification should be carried out over the full range of atmospheric types expected to be encountered. However, the immensity of the oceans, the scales of variability, and limited resources, require that the individual validation campaigns must be planned to address the individual components of the atmospheric correction algorithm believed to represent the greatest potential sources of error. In this appendix we develop a strategy for validation of atmospheric correction over the oceans. We also provide a description of the instrumentation and methods that have been developed for implementation of the plan.

1 Introduction

Atmospheric correction of ocean color imagery is discussed in the main body of this ATBD. Briefly, in atmospheric correction one attempts to remove the contribution to the radiance L_t measured by the sensor that results from scattering in the atmosphere and reflection from the sea surface. If carried out correctly, the result is the water-leaving spectral radiance, $L_w(\theta_v, \phi_v, \lambda)$, where θ_v and ϕ_v are, respectively, the polar and azimuth angles of a vector from the point on the ocean being examined (pixel) to the sensor, and λ is the wavelength. This is related to the upward radiance just beneath the sea surface $L_u(\theta'_v, \phi'_v, \lambda)$, where θ'_v and θ_v are related by Snell's law, and $\phi'_v = \phi_v$, i.e.,

$$L_w(\theta_v, \phi_v, \lambda) = \frac{T_F(\theta'_v, \theta_v)}{m^2} L_u(\theta'_v, \phi'_v, \lambda), \quad (1)$$

where m is the index of refraction of water, and T_F is the Fresnel transmittance of the air-sea interface. In an attempt to remove the effects of atmospheric transmission and the solar zenith angle, *Gordon and Clark* [1981] defined the normalized water-leaving radiance, $[L_w(\theta_v, \phi_v, \lambda)]_N$:

$$L_w(\theta_v, \phi_v, \lambda) = [L_w(\theta_v, \phi_v, \lambda)]_N \cos \theta_0 \exp \left[- \left(\frac{\tau_r(\lambda)}{2} + \tau_{Oz}(\lambda) \right) \left(\frac{1}{\cos \theta_0} \right) \right], \quad (2)$$

where $\tau_r(\lambda)$ and $\tau_{Oz}(\lambda)$ are the optical thicknesses of the atmosphere associated with molecular (Rayleigh) scattering and Ozone absorption, respectively, and θ_0 is the solar zenith angle at the specific pixel. The exponential factor partially accounts for the attenuation of solar irradiance by the atmosphere. Ignoring bidirectional effects [*Morel and Gentili*, 1991], the normalized water-leaving radiance is approximately the radiance that would exit the ocean in the absence of the atmosphere with the sun at the zenith. This quantity is used in other algorithms to derive ocean-related properties, e.g, the chlorophyll concentration. Often it is useful to replace radiance by reflectance. The reflectance ρ associated with a radiance L is defined to be $\pi L / F_0 \cos \theta_0$, where F_0 is the extraterrestrial solar irradiance. The normalized water-leaving radiance is converted to normalized water-leaving reflectance $[\rho_w]_N$ through

$$[\rho_w]_N = \frac{\pi}{F_0} [L_w]_N. \quad (3)$$

The goal of atmospheric correction of MODIS is to retrieve $[\rho_w(\theta_v, \phi_v, \lambda)]_N$ at 443 nm with an uncertainty less than ± 0.002 . This corresponds to an uncertainty of $\sim \pm 5\%$ at 443 nm in $[\rho_w(\theta_v, \phi_v, \lambda)]_N$ for very clear waters, e.g., the Sargasso Sea in summer [*Gordon and Clark*, 1981]. Here, we discuss the validation of the atmospheric correction procedure.

By the term validation of atmospheric correction, we mean quantification of the uncertainty expected to be associated with the retrieval of $[\rho_w(\theta_v, \phi_v, \lambda)]_N$ from the measurement of the total radiance (reflectance) exiting the ocean-atmosphere system. This uncertainty includes that associated with the measurement or estimation of auxiliary data required to operate the correction algorithm, e.g., surface wind speed, surface atmospheric pressure, total column Ozone concentration. For a proper validation, this quantification should be carried out over the full range of atmospheric and water types expected to be encountered in the retrievals.

2 Our approach to validation

In the main body it is shown that in the open ocean far from the influence of land (and in the absence of the long-range transport of dust) and/or anthropogenic aerosol sources, where the atmosphere is very clear and the aerosol is located in the marine boundary layer, a simple single-scattering correction algorithm should be sufficient to provide $[\rho_w(\theta_v, \phi_v, \lambda)]_N$ with the desired accuracy at 443 nm. For more turbid atmospheres, in which multiple scattering is important, *Gordon and Wang* [1994a] developed an algorithm that uses a set of candidate aerosol models developed by *Shettle and Fenn* [1979] to assess the effects of multiple scattering. This algorithm performs well as long as the absorption properties of the candidate aerosol models are similar to the actual aerosol present in the atmosphere. Furthermore, if the aerosol is nonabsorbing or weakly absorbing, the algorithm is insensitive to the vertical distribution of the aerosol. However, difficulties with this algorithm can occur under certain conditions, one of which is when the aerosol is strongly absorbing. In this case, the successful operation of the algorithm still requires that the candidate aerosol models be representative of the actual aerosol present, and in addition, that the thickness of the layer in which the dominant aerosol resides must be known or estimated with an accuracy of $\sim \pm 1$ km.

Based on these observations, it is reasonable to focus the atmospheric correction validation on regions dominated by (1) a locally generated maritime aerosol, and (2) strongly absorbing aerosols. In this manner it is possible to establish an uncertainty estimate characteristic of regions for which the atmospheric correction should be excellent, and to estimate how the uncertainty increases in regions with aerosols that present correction problems.

The open ocean, free of land and anthropogenic sources, represents the most favorable of conditions for atmospheric correction. In such a region, the aerosol is locally generated and resides in the marine boundary layer. In the absence of intense stratospheric aerosol, as might be present following a volcanic eruption, and in the absence of thin cirrus clouds, only whitecaps and residual sun glitter need to be removed in order that conditions satisfy those assumed in the development of the correction algorithm, i.e., a relatively clear two-layer atmosphere with aerosols in the lower layer. Under such conditions, the error in the water-leaving radiance due to the aerosol removal should be small, and specifying this component of the error field under these conditions relatively simple. When the error due to the aerosol is small, errors due to whitecaps and sun glitter may make a significant contribution to the overall error, therefore, a location with the conditions described above would be ideal for specifying the error fields due to these processes. The site chosen for such validation is in the waters off Hawaii.

There are two common situations with strongly absorbing aerosols in which the atmospheric correction algorithm may not retrieve the water-leaving radiances within acceptable error limits: situations in which the aerosol absorption is relatively independent of wavelength (urban aerosols transported over the oceans); and situations in which the aerosol absorption has significant dependence (desert dust transported over the oceans). Clearly, it is important to perform validation in regions and times where significant amounts of both types of absorbing aerosol are expected to be present over the water. In the case of urban pollution an ideal location is the Middle Atlantic Bight during summer (excellent logistics as well). For desert dust there are two important regions: the North Pacific (Gobi desert influence) and the Tropical North Atlantic (Saharan desert influence). We plan a validation cruise in the Tropical North Atlantic.

In order to utilize imagery in the more turbid Case 2 waters near coasts, it is critical to understand the limitations that significantly higher (than typical oceanic) concentrations of suspended particulate matter in the water place on atmospheric correction. Thus, validation of atmospheric correction should also be carried out in a coastal region of spatially varying turbidity. Such a validation can be effected in the Middle Atlantic Bight by making measurements at a set of stations successively closer to the coast. In this manner, it will be possible to combine the validation cruises for studying the limitations imposed by urban aerosols and by waters of moderate turbidity.

It is important to examine in detail the influence of stray light from bright targets (ghosting, internally reflected and scattered light, etc.) in the MODIS focal plane fields-of-view, on atmospheric correction. For example, how close can one perform adequate atmospheric correction to a cloud bank or coastline? This can be effected by examining the atmospheric correction in broken cloud fields and near islands in clear water. The Hawaii optical mooring site (Subsection 4.2) appears to be ideal for such studies. These would provide error bounds on normalized water-leaving radiances under such conditions. This single site should be adequate for assessing this component of the error field.

Validation of any algorithm developed for removal of stratospheric aerosols and/or thin cirrus clouds is also required; however, it will not be necessary to conduct a focussed validation experiment for this purpose. One need only track the quality of the atmospheric correction in the experiments recommended above with regard to the scene reflectance at 1380 nm (used to indicate the presence and amount of stratospheric aerosol and/or thin cirrus) to assess the efficacy of this component of the algorithm.

Finally, an important component of validation is an estimate of the day-to-day consistency and the long-term stability of the retrieved radiances. The Hawaii optical mooring site (Subsection 4.2) will provide the water-leaving radiances required to monitor the quality of the retrievals on a continual basis.

3 Required measurements

Obviously to validate the atmospheric correction it is necessary to compare near-simultaneous satellite-derived and surface-measured values of the retrieved quantity: $[L_w]_N$ or $[\rho_w]_N$. Typically, *in situ* measurements of $L_u(\theta'_v, \phi'_v, \lambda)$ are obtained only for $\theta'_v = 0$, and $[L_w]_N$ is derived for this direction, and used to develop algorithms for relating water-leaving radiance to ocean properties. It has usually been assumed that $L_u(\theta'_v, \phi'_v, \lambda)$ is nearly independent of θ'_v and ϕ'_v . However, recently Morel and coworkers [Morel and Gentili, 1991; Morel and Gentili, 1993; Morel, Voss and Gentili, 1995] have shown that L_u varies considerably, depending on θ'_v , ϕ'_v , θ_0 , and ϕ_0 , where ϕ_0 is the solar azimuth. Thus, for purposes of validation, one must measure $L_u(\theta'_v, \phi'_v, \lambda)$, i.e., the upwelling spectral radiance just beneath the sea surface in the direction the sensor is viewing. L_w is then determined with Eq. (1). As MODIS views the ocean with a spatial resolution of ~ 1 km at nadir,

an assessment of the variability of $L_u(\theta'_v, \phi'_v, \lambda)$ within the pixel under examination must be carried out to obtain a pixel-averaged $L_u(\theta'_v, \phi'_v, \lambda)$.

It is to be expected that in some cases the satellite-derived normalized water-leaving radiances will not agree with the surface measurements within the required error limits. In such cases it will be important to understand what part of the atmospheric correction algorithm is at fault in order to facilitate algorithm “fine tuning.” This requires what we term “auxiliary” measurements, i.e., measurements of quantities other than that which is being validated. Several such measurements are discussed next.

Since the major (highly variable) component to be removed during atmospheric correction is the aerosol, it is important to make detailed measurements of the columnar aerosol optical properties as part of the validation effort. Quantities to be measured include the spectral aerosol optical thickness and the spectral sky radiance, both close to (the aureole) and far from the sun. From such measurements, it is possible to obtain the columnar aerosol size distribution, aerosol phase function and aerosol single scattering albedo, an index of the aerosol absorption [*Kaufman et al.*, 1994; *King et al.*, 1978; *King and Herman*, 1979; *Nakajima, Tanaka and Yamauchi*, 1983; *Wang and Gordon*, 1993]. This data will be used to determine the applicability of the aerosol model selected by the algorithm for use in the atmospheric correction, and to provide a determination of the presence or absence of strongly absorbing aerosols.

As mentioned in Section 2, the correction algorithm is insensitive to the vertical distribution of the aerosol only if it is weakly absorbing or nonabsorbing. Thus, an additional possibility for a degradation in the accuracy of the retrieved water-leaving radiances is the presence of significant quantities of absorbing aerosol in the free troposphere. Because of this it is important to be able to assess the vertical structure of the aerosol. The most direct technique of effecting this is LIDAR [*Sasano and Browell*, 1989] and ship-borne micro pulse lidar [*Spinhirne*, 1993] will be included in validation exercises.

Whitecaps on the sea surface can also result in larger-than-required uncertainty in $[\rho_w(\theta_v, \phi_v, \lambda)]_N$ [*Gordon and Wang*, 1994b; *Koepke*, 1984], unless the increase in the spectral reflectance of the ocean-atmosphere system can be estimated within about ± 0.002 . The severity of the whitecap perturbation depends on the spectral form of the reflectance [*Frouin, Schwindling and Deschamps*,

1996; Gordon, 1996; Schwindling, 1995]. Thus, an estimate of the whitecap contribution to the perturbation of the $[\rho_w(\theta_v, \phi_v, \lambda)]_N$ is required.

Finally, the ancillary data required to operate the atmospheric correction algorithm, and, in the processing of MODIS data estimated from numerical weather models, must also be measured. These include surface atmospheric pressure, wind speed, and wind direction.

4 Instrumentation and measurements

The validation as envisaged will be carried out via ship-based and buoy-based measurements. The ship-based validation will involve the more complete set of measurements, as much of the instrumentation cannot be operated from buoys. We shall discuss each in detail.

4.1 Ship-based instrumentation

A complete set of measurements for validation of atmospheric correction must be ship-based, as the most fundamental measurement, $L_u(\theta'_v, \phi'_v, \lambda)$, can only be made from such platforms. The basic measurements to be carried out at sea are high spectral resolution ($\sim 3\text{--}4$ nm) measurements of L_u at nadir ($\theta'_v = 0$, actually $\theta'_v < 5^\circ$), measurement of $L_u(\theta'_v, \phi'_v, \lambda)$ in a few spectral bands (full width at half maximum (FWHM) ~ 10 nm), measurement of the augmentation of the water-leaving reflectance by whitecaps, measurement of the aerosol optical thickness (FWHM ~ 4 nm) and sky radiance (FWHM ~ 10 nm) in a few spectral bands, and measurement of ancillary parameters such as surface wind speed and direction and atmospheric pressure at the surface. Instrumentation developed to meet these measurement requirements is described next. Protocols for most of the measurements are provided in *Mueller and Austin* [1992].

4.1.1 Upwelling spectral radiance at nadir

Typically, for remote sensing applications, the optical measurements are performed in the near surface waters at three or four depths, z . The selection of these depths depends on the clarity of the water. The optical instrument which measures upwelled spectral radiances $L_u(z, \lambda)$ and downwelled spectral irradiance $E_d(z, \lambda)$ is suspended from a buoy and drifted away from the ship in order to avoid shadowing by the ship. On board the ship, a second spectrometer measures

the downwelling sky and sun spectral irradiance just above the sea surface, $E_s(z, \lambda)$, when the submersed spectrometer is at depth z in order to normalize for the variations in the incident irradiance. The shallowest observations of upwelled spectral radiances (nominally one meter) are then propagated upward to just beneath the sea surface by first calculating the upwelled spectral radiance attenuation coefficient $K_L(\lambda)$ using

$$K_L(\lambda) = \frac{1}{z_2 - z_1} \ln \left[\frac{L_u(z_1, \lambda) E_s(z_2, \lambda)}{E_s(z_1, \lambda) L_u(z_2, \lambda)} \right], \quad (4)$$

where z_1 and z_2 are the two shallowest depths at which measurements are carried out ($z_1 < z_2$). Then the radiance loss between the surface and z is accounted for through

$$L_u(0, \lambda) = L_u(z_1, \lambda) \exp[K_L(\lambda) z_1]. \quad (5)$$

The subsurface upwelled radiances are then transmitted through the sea surface using Eq. (1) and normalized with Eq. (2). These high resolution spectra may then be convolved with the satellite sensor's spectral response, $S_i(\lambda)$ for band i , to form the band-averaged water-leaving radiance:

$$\langle [L_w(\lambda)]_N \rangle_i = \int S_i(\lambda) [L_w(\lambda)]_N d\lambda. \quad (6)$$

Since effective application of ocean color satellite observations, to derive bio-optical products, rely totally on retrieving accurate and precise water-leaving radiances, a new marine optical instrumentation and a buoy system to enhance its in-situ measurement capability has been developed. A prototype Marine Optical System (MOS) has been constructed and tested. The operational version of this system is now in its final construction phase and is scheduled for at-sea test and evaluation during the summer of 1996. The system uses a modular design concept which has provided a high degree of flexibility and has facilitated the ease in which instrument upgrades can be implemented. The concept was constrained by the buoy requirement that necessitated the instrument be capable of maintaining measurement integrity while being unattended for long periods of time. This constraint has led to a design which minimizes the number of moving parts (one) and has resulted in the spectrographic application of concave holographic diffraction gratings. These spectrograph gratings approximate a flat focal field to the degree that planar silicone photodiode arrays may be used as detectors. Inherent within this technology are the features of simplicity, compactness, durability, and stable high performance system characteristics. The new operational version uses a convex holographic grating spectrograph with a cooled CCD detector system. These modifications

are being implemented in order to improve image quality, dynamic range, and signal to noise ratios. Additionally, the shipboard system is being modified to utilize fiber-optics to avoid the instrument self shadowing errors as described by *Gordon and Ding* [1992].

Laboratory radiometric calibrations are performed prior to and after each deployment. Spectral standards for irradiance are either NIST traceable or NIST standard lamps (1000 W FEL'S). NIST protocols for irradiance calibrations are used in conjunction with commercial systems (EG&G GAMMA Scientific (Model 5000) and Optronics Model 420) which have integrating spheres for radiance calibrations. During the laboratory calibrations, portable reference lamps are measured and then utilized during the at-sea deployments to provide a time history of the system response stability. For the buoy system a submersible reference lamp has been developed for divers to perform monthly checks of the system's stability. Wavelength calibrations are performed with five low pressure lamps, which provide numerous emission lines over the instruments spectral range.

4.1.2 Upwelling spectral radiance distribution

The spectral upwelling radiance distribution $L_u(z, \theta'_v, \phi'_v, \lambda)$ will be measured using a radiance distribution camera system (RADS) [Voss, 1989; Voss and Chapin, 1992]. This system employs a fisheye camera lens to image the upwelling radiance distribution onto a thermoelectrically cooled CCD camera (First Magnitude, Starscape IIb). Included in the optical path are interference filters which are used to select the spectral region of interest. There are four possible filter positions on each of two filter wheels which can be used to obtain the upwelling radiance distribution in 6 different spectral bands. Since only the near surface radiance distribution is needed in this application, the instrument will be deployed by suspending it beneath a float at the depth z_L of 1.5 to 2 meters. This will allow the instrument to drift away from the ship and avoid ship shadow contamination of the data [Gordon, 1985]. Data reduction and instrument calibration are performed using standard procedures which have been described elsewhere [Voss and Zibordi, 1989]. $L_u(z_L, \theta'_v, \phi'_v, \lambda)$ will be propagated to the surface using K_L derived from the nadir-viewing MOS (Subsection 4.1.1). This is acceptable as $L_u(z, \theta'_v, \phi'_v, \lambda)$ decays with depth in a manner that is a weak function of θ'_v and ϕ'_v . If necessary, the radiance distribution will be interpolated between spectral bands using the L_u at nadir spectrum discussed in the last paragraph.

4.1.3 Whitecap reflectance contribution

To determine the whitecap contribution to the top-of-the-atmosphere reflectance, a new radiometer system has been constructed [Moore, Voss and Gordon, 1996]. This instrument system consists of a narrow field-of-view radiometer, video camera system, downwelling irradiance sensor, wind speed and direction instruments, and a GPS receiver. The radiometer and irradiance sensor have 6 spectral bands each, with matching filters to enable the upwelling reflectance of the sea surface to be calculated. The radiometer and video camera system are aligned to view the same scene and deployed 5–10 m in front of the bow of the ship to obtain a downward view of the surface uncontaminated by ship wake effects even while the ship is underway. The full angle field-of-view of the radiometer is approximately 1° , so the diameter of the surface sampling area is typically 20 cm (depending on the height of the bow above the sea surface). The video camera signal is recorded and the images are time stamped to allow synchronization of the video images and radiometer data. The video images are useful for identifying whitecaps and other surface features in the data stream, e.g., sun glitter. The data from the radiometer, irradiance sensor, and wind speed and direction instrument are digitized at 1000 Hz, and the average of 100 samples are recorded at 0.5 Hz along with the GPS position. By continuously measuring the total reflectance of the ocean surface, the whitecap contribution to the signal may be determined. Samples in the data stream, with and without whitecaps, can be found, and therefore the overall reflectance with, and without, whitecaps can be determined. Since the relative wind speed, direction, and ship heading and speed are also recorded, a relationship between the true wind speed and whitecap augmentation of the reflectance can be found.

4.1.4 Aerosol optical thickness

The aerosol optical thickness is measured using a standard sun photometer [d'Almeida *et al.*, 1983]. The total optical thickness, τ , is given by the relationship,

$$\tau = -\frac{1}{m} \ln \left(\frac{E_m}{E_0} \right),$$

where E_m is the direct solar irradiance measured in instrument units (such as counts) with the sun photometer, E_0 is the calibrated extraterrestrial solar irradiance in instrument units, and m is the air mass. For solar zenith angles, θ_0 , less than 60° , m is very close to $1/\cos \theta_0$ [Kasten and Young, 1989]), it can be determined precisely from the solar ephemeris with the measurement of time and position. The E_0 is determined for the sun photometer through a Langley calibration

[Shaw, 1983]. The total optical depth is determined in spectral bands which do not have sharp molecular absorption bands. In this manner the only other components, besides aerosols, which have significant contributions are the molecular (Rayleigh) scattering and the broad Chappiux absorption band of Ozone. Thus once the total optical thickness is determined, the aerosol optical thickness can be found by subtraction of the Rayleigh optical thickness, determined by calculation [Young, 1980], and the ozone optical thickness, determined by ozone climatologies [Klenk *et al.*, 1983], or by direct measurement, and knowledge of the wavelength dependence of ozone absorption [Nicolet, 1981; Vigroux, 1953].

4.1.5 Sky radiance

On land, an automatic pointing instrument, e.g., the Automatic Sun and Sky Radiometer (ASSR) [Holben *et al.*, 1996] may be used to make sky radiance distribution measurements, but on a ship obtaining a stable reference is difficult and expensive. Thus, for our ship-borne program, we will use a camera system similar to the RADS system described above. This fisheye camera system is mounted in a “stable table” which is an active servo-controlled table to maintain its vertical reference. Otherwise the overall system is very similar to the in-water system. The sky camera can also be equipped with polarizers to enable measurement of the first three elements of the Stokes vector in the sky radiance distribution (the linear polarization components).

Because of the rapid change in sky radiance near the sun, the RADS system requires that a 10° portion of the sky around the sun be blocked to prevent flare in the camera lens system. To acquire the sky radiance near the sun, an important component when the atmospheric single scattering albedo is needed to assess the aerosol absorption, another instrument has been constructed. This instrument, a solar aureole camera system, is designed to measure the sky radiance for the region from 2° to 10° from the solar disk. This instrument is based on a cooled CCD camera system (Spectra source, MCD1000). In this system a 35 mm camera lens (50 mm focal length) is used to image the sky around the sun. An interference filter is attached to the front of the lens to select the spectral region of interest, and a small aperture (1 cm) is placed in front of the interference filter. A small occulting disk is placed approximately a meter in front of the camera and is oriented such that the shadow of this disk falls over the aperture on the interference filter. Thus the direct solar image is blocked from the camera system, yet the area around the sun can be imaged. The system is controlled, via software, to be operated with a push-button on the camera itself. When

the shadow of the occulter is in the correct position, the operator triggers the push-button which tells the camera system to operate the shutter then to download the image. Immediately afterward, a dark image is obtained to be used in the data reduction process. Calibration of this system is similar to the RADS system. The calibration procedures required include, camera system roll off and flat fielding, system linearity, absolute radiance calibration, and spectral calibration. These procedures have been performed as described in *Voss and Zibordi* [1989].

4.1.6 Phytoplankton pigments

Normally the measurement of the phytoplankton pigment concentration, C , (defined to be the sum of the concentrations of chlorophyll a and phaeophytin a in the water) is not used in this type of validation process. However, for the very clear water cases ($C \lesssim 0.25 \text{ mg/m}^3$), the water-leaving radiance spectral variance can be estimated as a function of pigment concentration for $\lambda \gtrsim 520 \text{ nm}$ [*Gordon and Clark*, 1981]. In-order to estimate the spatial variability of the surface waters around the primary bio-optical station, a grid of ship tracks is traversed while continuously measuring chlorophyll a fluorescence. A fluorometer, depth sensor, and water pumping system are towed while the ship is underway at near-surface depth (five meters typically). Calibration of the fluorometric signal is conducted from high frequency sampling (every 15 minutes) of the water pumped from the towed depth for laboratory extraction of pigments. Contour maps of the pigment distribution and the estimated normalized water-leaving radiances are then generated for satellite inter-pixel variability analyses.

4.1.7 Ancillary measurements

Apparent wind speed and direction are determined using a standard instrument manufactured by Young Co. (Model 05103). The apparent wind observations are corrected for the ship's heading and speed from the ship's navigation instrumentation (gyro and speed log). Relative humidity and air temperature are measured with Vaisalla sensor systems (Models HMD 30/UB/YB and HMD/W 30YB respectively). Atmospheric pressure is obtained from a digital pressure transducer manufactured by Setra (Model 470). These measurements are all continuously logged at 1hz along with GPS time and position. The data are then processed into mean values at specified time intervals, i.e., mean atmospheric pressure every four hours. Ozone concentrations may be obtained from various sources. For the MOBY site, column ozone can be obtained from the

NOAA/CMDL site at Mauna Loa (personal communication, Gloria Koenig, NOAA/CMDL). For other sites in the northern hemisphere data can be obtained from the WMO Ozone Mapping Centre. (<http://www.athena.auth.gr:80/ozonemaps/>) which derives the data from SBUV-2 satellite data and ozone sonex around the world.

4.2 Buoy-based instrumentation

The Marine Optical Buoy System (MOBY), is tethered to a slack-line moored main buoy. MOBY is a 15 meter, 2500 lb, wave-rider buoy which emulates an “optical bench” with a 12 meter column extending into the sea. The surface buoy floatation (manufactured by Moorings System Inc.) is 1.7 meters in diameter, with four 40-watt solar panels mounted to the antenna support column. The surface buoy houses the controlling computers, mass storage, electronics, cellular modem, and computer battery. The Marine Optical System discussed in Subsection 4.1.1, has been reconfigured for the buoy application. The instrument along with four 200 amp/hr gelcell marine batteries is located in the subsurface housing at the bottom of the buoy. The apparent optical properties (upwelled radiances and downwelled irradiances) are measured by a series of remote collectors positioned on arms extending away from the central column. The arms may be positioned at varying depths, typically 1.5, 6, and 10 meters, along the column. The E_s sensor is located at the top of the surface buoy. The remote collectors are coupled to 1 mm, multimode fiberoptic cables which are terminated at a fiberoptic rotary selector (multiplexer). This optical multiplexer is mounted to one of the MOS entrance windows. Multiplexer ports are selected and the energy incident on the remote collector relays the light into the MOS optical train and detectors. The optical and ancillary data are relayed to the surface computer and stored on disk for future access via a cellular telephone link. The transmitted data will be converted into calibrated radiances and a water-leaving radiance data base for sensor quality control monitoring and algorithm development.

The selection of the calibration/validation site for MOBY was primarily based upon the clear-water water-leaving radiance criterion [*Gordon and Clark*, 1981], logistics, and survivability. The site selected is located at 20°49.0'N and 157°11.5' W in 1200 m of water, and is approximately 10 nautical miles from the west coast of the Hawaiian Island of Lanai. The mountains on the Islands of Molokai, Lanai, and Maui provide a lee from the dominant trade winds. This lee reduces the amount of sea, swell, and cloud cover at the mooring site which increases the probability of mooring survivability and cloud free satellite coverage. Logistics are conducted from a dockside operational

support facility which has been constructed at the University of Hawaii's Marine Operations Facility in Honolulu. GTE-MobleNet has excellent cellular coverage in the region, facilitating the transfer of relatively large MOBY observational data sets back to the MOBY support facility computer or to the mainland. University of Hawaii ships are utilized for MOBY deployments and maintenance. The transit time to the MOBY site from Honolulu is approximately six hours, allowing for a relatively quick response time in case emergency service is required.

In support of the MOBY calibration/validation effort, a land-based automatic sun and sky radiometer [*Holben et al.*, 1996] (ASSR, CIMEL Electronique) has been installed at a remote site on the west coast of Lanai at 20°49.57' N, 156°59.1' W. The ASSR measures the direct solar irradiance in several wavelength bands (440, 670, 870, 937, 940, and 1020 nm) in the visible every 15 minutes during the morning and afternoon. In addition the instrument measures the sky radiance in the principal plane (the sun-zenith plane) and along the almucantar (the collection of azimuthal angles with the same zenith angle as the sun) in several wavebands (440, 670, 860, and 1020 nm) three times each morning and afternoon. This data is collected automatically, and is sent via the GOES satellite to NASA/Goddard where it can be accessed over the Internet. In its location on Lanai it has an unobstructed view to the south and west for measurement of the sky radiance and the aerosol optical thickness. Volcanic activity on the Island of Hawaii, which lies approximately 165 miles to the southeast of the site, will produce unique aerosol occurrences when the surface winds are from the southeast. The frequency of these wind conditions is approximately ten days per year (J. Porter, University of Hawaii, personal communication). The observations are acquired approximately 11.3 nautical miles from the MOBY site and should be representative of the atmospheric conditions in that region. Shipboard atmospheric measurements will be made for comparison purposes on the MOBY quarterly maintenance cycles.

5 Validation Schedule

The planned schedule for carrying out the MODIS validation activities described in this appendix is presented in Figure 1.

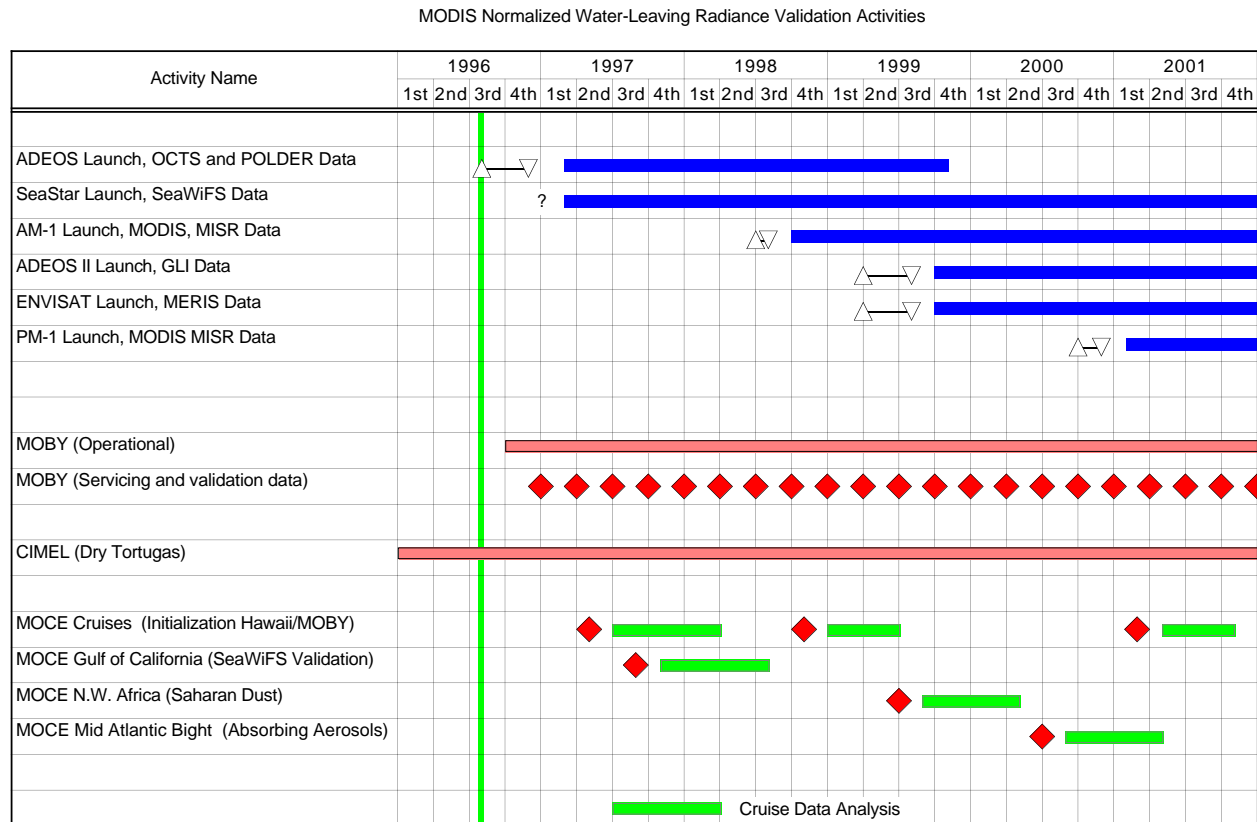


Figure 1. Schedule of activities for validation of normalized water-leaving radiance.

6 Data system

The validation data generated through these efforts will be matched with the appropriate satellite imagery (on a pixel-by-pixel basis) and archived within a “matchup data base” being developed by R. Evans. A description of this data system effort is described in the ATBD “Processing Framework and Matchup Data Base: MODIS Algorithm” by R. Evans. The validation data will then be transferred to EOSDIS for archive.

7 Concluding remarks

We have described the requirements for validating the MODIS atmospheric correction algorithm over the oceans, and presented a plan for effecting the validation. To implement the validation plan, new instrumentation and techniques have been developed, and were briefly described in the text. With few exceptions, the instrumentation required to carry out the plan exists or is in the final

phase of testing. We believe that the plan as described will provide a measure of the uncertainty expected to be associated with the atmospheric correction of MODIS. It will also provide data to allow “fine tuning” of the correction algorithm using MODIS data. If carried out, it should allow establishment of the correction uncertainty characteristic of oceanic regions for which atmospheric correction is normally expected to be excellent, and provide an estimate of the increase in uncertainty in settings in which the correction is expected to be degraded. The quality of the validation will be dependent on the extent to which the plan can be carried out.

References

- d'Almeida, G. A., R. Jaenicke, P. Roggendorf and D. Richter, New sunphotometer for network operation, *Applied Optics*, 22, 3796–3801, 1983.
- Frouin, R., M. Schwindling and P. Y. Deschamps, Spectral reflectance of sea foam in the visible and near-infrared: In-situ measurements and implications for remote sensing of ocean color and aerosols, *Jour. Geophys. Res.*, 101C, 14,361–14,371, 1996.
- Gordon, H. R., Ship Perturbation of Irradiance Measurements at Sea 1: Monte Carlo Simulations, *Applied Optics*, 23, 4172–4182, 1985.
- Gordon, H. R., 1996, Atmospheric Correction of Ocean Color Imagery in the Earth Observing System Era, submitted to *Jour. Geophys. Res.*.
- Gordon, H. R. and D. K. Clark, Clear water radiances for atmospheric correction of coastal zone color scanner imagery, *Applied Optics*, 20, 4175–4180, 1981.
- Gordon, H. R. and K. Ding, Self-Shading of In-Water Optical Instruments, *Limnology and Oceanography*, 37, 491–500, 1992.
- Gordon, H. R. and M. Wang, Retrieval of water-leaving radiance and aerosol optical thickness over the oceans with SeaWiFS: A preliminary algorithm, *Applied Optics*, 33, 443–452, 1994a.
- Gordon, H. R. and M. Wang, Influence of Oceanic Whitecaps on Atmospheric Correction of SeaWiFS, *Applied Optics*, 33, 7754–7763, 1994b.
- Holben, B. N., T. F. Eck, I. Slutsker, D. Tanre, J. P. Buis, A. Setzer, E. Vermote, J. Reagan, Y. Kaufman, T. Nakajima, F. Lavenue and I. Jankowiak, 1996, Automatic Sun and Sky Scanning Radiometer System for Network Aerosol Monitoring, *Remote Sensing of Environment* (In press) .
- Kasten, F. and A. T. Young, Revised optical air mass tables and approximation formula, *Applied Optics*, 28, 4735–4738, 1989.

- Kaufman, Y. J., A. Gitelson, A. Karnieli, E. Ganor, R. S. Fraser, T. Nakajima, S. Mattoo and B. N. Holben, Size distribution and scattering phase functions of aerosol particles retrieved from sky brightness measurements, *Jour. Geophys. Res.*, *99D*, 10341–10356, 1994.
- King, M. D., D. M. Byrne, B. M. Herman and J. A. Reagan, Aerosol size distributions obtained by inversion of optical depth measurements, *Jour. Atmos. Sci.*, *35*, 2153–2167, 1978.
- King, M. D. and B. M. Herman, Determination of the Ground Albedo and the Index of Absorption of Atmospheric Particulates by Remote Sensing. Part I: Theory, *Jour. Atmos. Sci.*, *36*, 163–173, 1979.
- Klenk, K. F., P. K. Bhartia, E. Hilsenrath and A. J. Fleig, Standard ozone profiles from balloon and satellite data sets, *J. Climate and Appl. Meteorology*, *22*, 2012–2022, 1983.
- Koepke, P., Effective Reflectance of Oceanic Whitecaps, *Applied Optics*, *23*, 1816–1824, 1984.
- Moore, K. D., K. J. Voss and H. R. Gordon, Measurements of the Spectral Reflectance of Whitecaps in the Open Ocean, *EOS, Transactions, American Geophysical Union*, *76*, OS105, 1996.
- Morel, A. and B. Gentili, Diffuse reflectance of oceanic waters: its dependence on Sun angle as influenced by the molecular scattering contribution, *Applied Optics*, *30*, 4427–4438, 1991.
- Morel, A. and B. Gentili, Diffuse reflectance of oceanic waters. II. Bidirectional aspects, *Applied Optics*, *32*, 6864–6879, 1993.
- Morel, A., K. J. Voss and B. Gentili, Bidirectional reflectance of oceanic waters: A comparison of modeled and measured upward radiance fields, *Jour. Geophys. Res.*, *100C*, 13,143–13,150, 1995.
- Mueller, J. L. and R. W. Austin, *SeaWiFS Technical Report Series: Volume 5, Ocean Optics Protocols for SeaWiFS Validation*, NASA, Greenbelt, MD, Technical Memorandum 104566, July 1992.

- Nakajima, T., M. Tanaka and T. Yamauchi, Retrieval of the Optical Properties of Aerosols from Aureole and Extinction Data, *Applied Optics*, 22, 2951–2959, 1983.
- Nicolet, M., The solar spectral irradiance and its action in the atmospheric photodissociation processes, *Planet. Space Sci.*, 29, 951–974, 1981.
- Sasano, Y. and E. V. Browell, Light scattering characteristics of various aerosol types derived from multiple wavelength lidar observations, *Applied Optics*, 28, 1670–1679, 1989.
- Schwindling, M., Modeles et mesures pour l’observation spatiale de la couleur de l’ocean: Diffusion atmospherique par les aerosols et reflexion de surface par l’ecume, 1995, Docteur de L’Universite these, Univ. des Sci. et Tech. de Lille. 245 pp.
- Shaw, G. E., Sun Photometry, *Bull. Am. Meterol. Soc.*, 64, 4–9, 1983.
- Shettle, E. P. and R. W. Fenn, Models for the Aerosols of the Lower Atmosphere and the Effects of Humidity Variations on Their Optical Properties, Air Force Geophysics Laboratory, Hanscomb AFB, MA 01731, AFGL-TR-79-0214, 1979.
- Spinhirne, J. D., Micro Pulse Lidar, *IEEE Transactionson Geoscience and Remote Sensing*, 31, 48–55, 1993.
- Vigroux, E., Contribution a l’etude experimentale de l’absorption de l’Ozone, *Ann. Phys. Paris*, 8, 709–762, 1953.
- Voss, K. J., Electro-optic Camera System for Measurement of the Underwater Radiance Distribution, *Optical Engineering*, 28, 241–247, 1989.
- Voss, K. J. and A. C. Chapin, Next generation in-water radiance distribution camera system, *Society of Photo-Optical Instrumentation Engineers, Ocean Optics XI*, 1750, 384–387, 1992.
- Voss, K. J. and G. Zibordi, Radiometric and Geometric Calibration of a Visible Spectral Electro-Optic “Fisheye” Camera Radiance Distribution System, *Jour. Atmos. and Oceanic Technology*, 6, 652–662, 1989.

Wang, M. and H. R. Gordon, Retrieval of the Columnar Aerosol Phase Function and Single Scattering Albedo from Sky Radiance over the Ocean: Simulations, *Applied Optics*, 32, 4598–4609, 1993.

Young, A. T., Revised depolarization corrections for atmospheric extinction, *Applied Optics*, 19, 3427–3428, 1980.